PONTIFICIA UNIVERSIDAD CATOLICA DE CHILE
ESCUELA DE INGENIERIA

INTEGRATION AND CHARACTERIZATION OF A POLARIZED RADIO FREQUENCY SOURCE FOR UAV-BASED TELESCOPE CALIBRATION

FELIPE ERNESTO CARRERO MUÑOZ

Thesis submitted to the Office of Research and Graduate Studies in partial fulfillment of the requirements for the Degree of Master of Science in Engineering

Advisor:
ROLANDO DÜNNER PLANELLA

Santiago de Chile, December, 2021

PONTIFICIA UNIVERSIDAD CATOLICA DE CHILE
ESCUELA DE INGENIERIA

INTEGRATION AND CHARACTERIZATION OF A POLARIZED RADIO FREQUENCY SOURCE FOR UAV-BASED TELESCOPE CALIBRATION

FELIPE ERNESTO CARRERO MUÑOZ

Members of the Committee:

ROLANDO DÜNNER PLANELLA Rolando Dünner

ANDRÉS GUESALAGA MEISSNER

NICOLÁS REYES GUZMÁN

JORGE VERA ANDREO

Thesis submitted to the Office of Research and Graduate Studies in partial fulfillment of the requirements for the Degree of Master of Science in Engineering

Santiago de Chile, December, 2021

CONTENTS

LIST OF TABLES

LIST OF FIGURES

ABSTRACT

In experimental cosmology, the study of the Cosmic Microwave Background (CMB) radiation requires accurate measurements of temperature fluctuations of fraction of Kelvin and extended polarization signals up to 4 orders of magnitude below the main 2.725 K signal. Thus, the systematic effects introduced by radio telescopes must be precisely characterized to ensure that the measured signals accurately represent the underlying physical phenomena. The calibration of polarization sensitive telescopes through the novel approach of using an artificial, polarized radio frequency (RF) source carried by an Unmanned Aerial Vehicle (UAV) rises as an alternative with several benefits as opposed to traditional characterization methods. To explore this possibility, the Astro-Engineering Center (AIUC) of Pontificia Universidad Católica de Chile has taken on the design and implementation of a UAV-based CMB telescope calibrator.

This thesis aims to integrate, characterize, and test a polarized RF source than can be mounted on a UAV to calibrate polarization sensitive radio telescopes of CMB experiments. The objectives of this work are the development of a mechanical structure to house the system components; the integration and testing of the RF electronics; the design and implementation of characterization experiments for the system; the execution of electromagnetic simulations of the Cosmology Large Angular Scale Surveyor (CLASS) radio telescope at 150 GHz; and a test flight of the integrated system. To this end, the 3D modelling software SolidWorks (Dassault Systèmes) will be used to design and validate the mechanical structure; an anechoic chamber and a spectral analyzer will be used to test the RF system and perform the characterization experiments; and the electromagnetic simulations will be carried out in the electromagnetic modelling software GRASP (Ticra).

The result of this thesis is a fully functional and characterized polarized RF source that can be carried by a UAV with the aim of being used in the calibration of polarization sensitive radio telescopes to allow for more accurate calibration procedures.

Keywords: radio, astronomy, telescopes, CMB, calibration, drone, UAV, polarization

RESUMEN

En cosmología experimental, el estudio de la Radiación de Fondo de Microondas (CMB) requiere mediciones precisas de fluctuaciones de temperature de fracción de Kelvin y de señales extendidas de polarización que pueden estar hasta 4 órdenes de magnitud por debajo de la señal principal de 2.725 K. Así, los efectos sistemáticos introducidos por los radiotelescopios deben ser precisamente caracterizados para asegurar que las señales medidas representan apropiadamente los fenómenos físicos subyacentes. La calibración en polarización de estos telescopios mediante el novedoso uso de radiofuentes artificiales llevadas por vehículos aéreos no tripulados (VANT) se perfila como una alternativa con varios beneficios frente a métodos tradicionales. Para explorar esta alternativa, el Centro de Astro-Ingeniería (AIUC) de la Pontificia Universidad Católica de Chile se ha embarcado en el diseño y desarrollo de un calibrador polarizado para la calibración de radio telescopios mediante vehículos aéreos no tripulados.

Esta tesis apunta a integrar, caracterizar y probar una fuente de RF que pueda ser montada en un VANT para calibrar telescopios de CMB sensibles a la polarización. Los objetivos de este trabajo son el desarrollo de una estructura mecánica para albergar los componentes; la integración y prueba de la electrónica de RF; el diseño e implementación de experimentos de caracterización; simulaciones electromagnéticas en 150 GHz del telescopio Cosmology Large Angular Scale Surveyor (CLASS); y una prueba de vuelo del sistema integrado. Para estos fines, se emplearán: el software de modelado CAD SolidWorks (Dassault Systèmes), para diseñar y validar la estructura de montaje; una cámara anecoica equipada con un robot CNC, un analizador espectral y bolómetros, para realizar la caracterización del sistema de RF; y el software de modelado electromagnético GRASP (Ticra), para las simulaciones electromagnéticas.

El resultado de este trabajo es una fuente de RF autocontenida y caracterizada, que puede ser llevada por VANTs para utilizarse en calibraciones más precisas de radiotelescopios de CMB sensibles a la polarización.

Palabras clave: radioastronomía, telescopios, CMB, calibración, drone, VANT, polarización

1. INTRODUCTION

1.1. Motivation

The usage of radio telescopes in experimental cosmology poses a variety of scientific and technical challenges that must be overcome to bring answers to fundamental questions about the universe. These experiments aim to measure and map the anisotropies of the Cosmic Microwave Background (CMB) radiation in intensity and polarization. The average temperature of the CMB is 2.725 K ± 0.00057 K (Fixsen, 2009) but the anisotropies themselves are in the order of millikelvin, while the expected polarization signals are up to 6 orders of magnitude below the main signal (Kamionkowski & Kovetz, 2016).

The sensitivity necessary to measure the CMB signals also raises the issue of dealing with systematic effects introduced by the instrument, e.g., those related to the optics or electronics (Stevens, et al., 2018). An accurate calibration involving precise characterization of systematic effects of the telescope is required to generate reliable scientific data. Leaving these effects unaccounted for may entirely remove the capability to measure a given phenomenon or result in an inaccurate depiction of the underlying physical process. For instance, it is estimated that in order to detect physical phenomena such as cosmological gravitational waves and birefringence, polarization accuracy in the calibration must be of the order of tenths of a degree (Abitbol, et al., 2020); calibration accuracies lower than this value may impair the ability to detect the aforementioned phenomena.

Radio telescope calibration is frequently carried out using natural radio frequency (RF) sources, such as planets or satellites (Wilson, Rohlfs, & Huettemeister, 2012). Other polarization sensitive experiments such as CMB experiments require highly polarized radio sources to perform appropriate calibrations, e.g., Taurus-A. However, such polarized sources are not abundant, provide insufficient accuracy or have not been widely studied at millimeter wavelengths (Keating, Shimon, & Yadav, 2012; Huffenberger, et al., 2015). Alternatively, artificial, controllable, ground-based radio sources can also be used in the calibration procedures of most radio telescopes; however, given the high sensitivity and low dynamic range of detectors required for experimental cosmology, ground-based RF sources become a less viable option due to ground pick at low telescope elevations (Stevens, et al., 2018). Moreover, stationary ground-based RF sources may not be able to serve as a calibrator for other critical sections of the radiation pattern of a telescope, such as far side lobes or back lobes.

A novel alternative proposed to overcome limitations in radio telescope calibration is the use of an aerial artificial RF source (Nati, et al., 2018) or through use of Unmanned Aerial Vehicles (UAV). The latter alternative combines the mobility of UAVs with the versatility of a controllable artificial RF source and has been devised and carried out successfully for radio telescopes at frequencies of up to a few gigahertz (Martínez Picar, Marqué, Anciaux, Lamy, & Ranvier, 2015; García-Fernández, et al., 2017; Paonessa, Virone, Bolli, & Addamo, 2018).

In this context, the Astro-Engineering Center (AIUC) of the Pontificia Universidad Católica de Chile (PUC) has taken on the design and implementation of a UAV-carried RF source for use in CMB radio telescope calibration. The system components include a professional heavy-lift drone and gimbal, RF filters, amplifiers and multipliers, control electronics, a wire grid polarizer, and a compact high-definition video camera. The end goal of the project is to implement a CMB telescope calibrator that emits a pure, highly linearly polarized RF tone to serve as a reference with at least 0.1° accuracy for the polarization angle. The determination of the polarization angle will be carried out through a combination of high-accuracy GPS positioning embedded in the drone plus photogrammetry to determine the attitude of the RF source.

This work aims at obtaining a fully functional, controllable, linearly polarized RF source that can be carried by a UAV and serve as an accurate aerial CMB radio telescope polarization calibrator.

1.2. Hypothesis

The integration and characterization of a polarized RF source and its incorporation into a

UAV will allow us to determine the viability of UAV-based, more accurate millimeter wave radio telescope calibrations that allow for the determination of the absolute polarization angle with 0.1° accuracy and the measurement of the influence of far side lobes, which cannot be easily achieved through current, conventional methods.

This general hypothesis is subject to each of the components of the calibrator achieving the appropriate levels of performance as detailed in the specific hypotheses below:

- The RF source, including the mechanical support structure, will be below the maximum payload of the UAV (evaluated at the altitude of CMB observatory high sites).
- The photogrammetry-based metrology system will be able to achieve angular accuracy better or equal to 0.1° for the absolute polarization angle.
- The emitted power of the RF source and drone emission will be within the typical power constraints for linear operation of CMB detectors.
- The power variations of the RF system will be below 10% of emitted power for the duration of the typical calibration mission.
- The frequency variations of the RF system will account for no more than 1% of the typical bandwidth of CMB telescopes and frequency shift power variations will remain negligible.

1.3. Objectives

The general objective of this thesis is the integration, characterization, and testing of a linearly polarized, millimeter wavelength RF source that can be mounted on a UAV to serve as a calibrator for CMB radio telescopes.

To attain the main objective, several specific objectives have been proposed and are detailed below:

a. <u>Implementation of electromagnetic simulations of the Cosmology Large Angular Scale Surveyor (CLASS) telescope at 150 GHz</u>: the goal is to study the properties of a representative CMB telescope, such as the CLASS telescope, at a frequency of interest and gain insight into possible effects during a potential test flight. The electromagnetic (EM) modelling software GRASP (by Ticra) will be used to perform these simulations.

b. Design and implementation of a mechanical frame: the goal is to design structure that can be integrated into the drone's gimbal, while complying with volume, weight, rigidity, ease of assembly and other constrains. The 3D modelling software SolidWorks (by Dassault Systèmes) will be used to design and validate the structure.

c. Integration of the RF source and design and implementation of characterization experiments: the goal is to integrate the system components into a self-contained, controllable, polarized RF source and design experiments that allow for an appropriately characterized device. These include: power stability tests; band power measurements; angular measurements of the RF source, such as radiation pattern characterization, polarization angle measurements and measurement of polarization angle maps; and frequency stability tests. These experiments will be carried out using a spectral analyzer, RF detectors, an anechoic chamber, high-speed rotary actuators, and a Computer Numerical Control (CNC) robot.

d. Validation of the polarizer alignment system: the goal is to design an algorithm capable of obtaining the relative angle between the camera and polarizer grid — the UAV-based calibrator's absolute polarization angle reference— in an accurate and reliable manner, then test this method with the integrated RF source.

e. Integrated RF source test flight: the goal is to perform a test flight of the drone with the integrated RF source and assess the overall system performance with the current design.

1.4. Document organization

This thesis is divided into 6 chapters, whose contents are detailed as follows:

1. Introduction: this section briefly outlines the motivation of this work, presents the hypothesis, the objectives, and describes the organization of the document.

2. Theoretical Framework: this section describes the engineering and scientific considerations that give rise to the challenges related to accurate radio telescope calibration and the need for more sophisticated calibration methods. Its subsections consist of a general introduction to radio astronomy, including an outline of the radio telescope and its most important parameters; an overview of cosmology and the study of the CMB; and radio telescope calibration methods, including a revision of alternative calibration methods for CMB experiments.

3. The Cosmology Large Angular Scale Surveyor (CLASS) project: this section describes the CLASS experiment, its scientific goals and technical specifications. Given that the source is expected to be ultimately tested with this telescope, electromagnetic simulations were designed, performed, and analyzed to gain insight into a prospective flight at the CLASS observatory.

4. Technical considerations of the RF source: this section describes the UAV-based calibrator project of the Astro-Engineering Center and the technical requirements that give rise to the need of characterization of the UAV-carried RF source.

5. Integration and characterization of the RF source: this section concerns the design and implementation of the mechanical frame for the RF source, as well as the design and implementation of characterization experiments, and analysis of their results.

6. Conclusions: in this section we analyze the viability of the UAV-based calibrator in its current design, summarizing the most relevant findings of this work's characterization experiments, and assessing whether the goals set at the beginning of this work were attained.

2. THEORETICAL FRAMEWORK

2.1. Radio Astronomy

In 1931, the American engineer Karl Jansky discovered radio waves emanating from the Milky Way and forever changed the way Astronomy looks at the universe. Before this discovery, information obtained from the universe came only from visible light, which limited our ability to understand more complex physical phenomena such as star and planet formation, high energy processes in galaxies or even the early moments of the Big Bang (Burke, Graham-Smith, & Wilkinson, 2019).

Radio astronomy can be defined as the study of natural emission from celestial sources, with a range of observable frequencies spanning roughly 5 decades between the far-infrared at $\nu \sim 1$ THz and the high-frequency (HF) radio band at $\nu \sim 10$ MHz (ITU, 2013). Due to the broad range of frequencies, radio astronomy has access to the observation of physical processes such as nuclear transitions, electronic motions, molecular vibration and rotation, and electronic precession, which allows for a comprehensive understanding of a large variety of astrophysical phenomena (Wilson, Rohlfs, & Huettemeister, 2012).

Another fundamental advantage of radio astronomy lies in the observation methods used at radio wavelengths. In principle, radio signals can be understood as sums of radio quanta, whose low energies (from 4×10^{-7} eV at 10 MHz, to 4×10^{-3} eV at 1 THz) allow us to disregard their quantum statistical properties and treat them as classical waves. Such regime enables the amplification, frequency down-conversion and digitalization of the signal, as well as the use of complex coherent receivers, in which the phase of the signal is accurately preserved. These characteristics have led to the implementation of radio spectrometers with high spectral resolution and frequency accuracy, as well as the construction of sensitive aperture-synthesis interferometers, which can image astronomical sources with extremely high angular resolution up to 10^{-4} arcseconds (Condon & Ransom, 2016; Burke, Graham-Smith, & Wilkinson, 2019).

Earth's atmosphere blocks most infrared, ultraviolet, X-ray and gamma-ray radiation, which require specialized, spaceborne equipment to be observed. However, radio waves at lower frequencies traverse the atmosphere mostly unaltered and can be observed from earth's surface, which constitutes the so-called radio window, shown in Figure 2-1. The lower cutoff frequency of the radio window is determined by the ionospheric plasma, which fully reflects signals with wavelengths longer than ~10 meters (3 MHz). The high-frequency end of the radio window is mainly limited by the absorption of radio waves from molecules of water vapor (H_2O) and oxygen (O_2). For water vapor, the resonant absorption frequency bands are centered at ν = 22.2 GHz ($\lambda \approx$ 13 mm) and ν = 183 GHz ($\lambda \approx$ 1.6 mm), while oxygen has a band at ν = 60 GHz ($\lambda \approx$ 5 mm) and a line at ν = 119 GHz ($\lambda \approx$ 2.5 mm). Most of these bands span several gigahertz, which forbids observations at those frequencies unless carried out at extremely dry locations. The cut-off at higher frequencies is given by abundant molecules in the atmosphere, such as nitrogen (N_2) and carbon-dioxide (CO_2), which occur at frequencies above 300 GHz (Condon & Ransom, 2016; Wilson, Rohlfs, & Huettemeister, 2012; Burke, Graham-Smith, & Wilkinson, 2019).

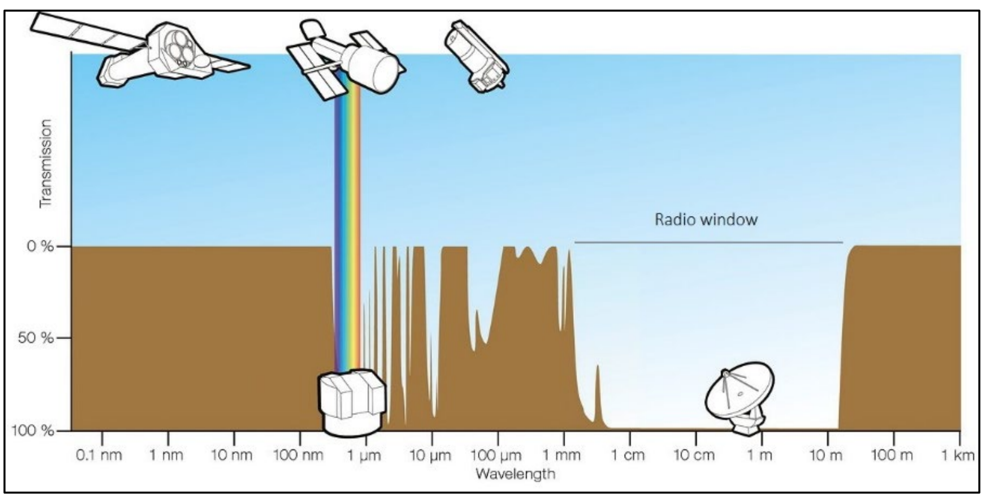

Figure 2-1. Atmospheric windows at different wavelengths.
Adapted from 'Atmospheric windows', by F. Granato (ESO), 2010, retrieved from https://www.eso.org/public/spain/images/atm_opacity

In addition to the opacity, the partially absorbing atmosphere also emits radio noise that can degrade the sensitivity of ground-based radio observations (Condon & Ransom, 2016). Given that the higher frequency portion of the radio window is so greatly affected by the effects of water vapor, it is possible to extend the accessible frequency range by carrying out measurements from locations with low total water vapor content (Wilson, Rohlfs, & Huettemeister, 2012). For example, CMB experiments and observatories such as the Atacama Large Millimeter/Submillimeter Array (ALMA) —whose wavelengths of interest are in the order of millimeters— are located at altitudes of 5000 meters or above to maximize sensitivity and take advantage of a more radio-transparent atmosphere.

Radio astronomy benefits from access to almost all types of astronomical sources, radiation mechanisms of thermal and nonthermal origin, as well as different types of propagation phenomena. In this context, some of the current lines of work include radio galaxies and quasi-stellar radio sources (quasars), powered by supermassive black holes; the study coherent continuum emission from stars and pulsars; kinetics in galaxies related to the search for evidence of dark matter; star and planet formation; study of the evolution of large-scale structures of the universe; and the study of Cosmic Microwave Background Radiation from the Big Bang, leading to the hunt for gravitational waves or model defying phenomena such as Cosmic Birefringence or primordial magnetic fields (Condon & Ransom, 2016; Wilson, Rohlfs, & Huettemeister, 2012; Burke, Graham-Smith, & Wilkinson, 2019; Abitbol, et al., 2020; Pogosian & Zucca, 2018).

Such a myriad of physical processes and sources call for a wide variety of observation techniques and instruments, and while detailing each of them is not within the scope of this work, it is convenient to describe the basic element of radio astronomical observations and outline its more relevant parameters: the radio telescope.

2.1.1. The Radio Telescope

A radio telescope can be defined as a device that intercepts radio radiation coming from celestial sources and acts as a transducer that converts electromagnetic radiation into electrical current or voltage (Condon & Ransom, 2016; Burke, Graham-Smith, & Wilkinson, 2019). In its typical configuration, a radio telescope consists of two basic elements: an antenna feed and a reflecting surface —or aperture—. The reflecting surface, usually parabolic in shape, concentrates radiation and brings it into focus on the antenna. The antenna then receives the incoming electromagnetic fields and transforms them into a signal that can be measured directly with relative ease. This simple configuration of a single reflector and feed is usually referred to as a prime focus dish.

Figure 2-2. Lovell Telescope at Jodrell Bank Observatory, an example of a prime focus dish. From “SKA Telescope – Images”, by University of Manchester, 2021, retrieved from https://www.skatelescope.org/multimedia/image/ska-pathfinder-lovell-telescope-used-for-e-merlin/

Determining antenna properties in a receiving configuration is not a straightforward task, as it often involves more complicated calculations. However, the properties of the antenna can be analyzed interchangeably from the perspective of transmission or reception, which is the principle of the *reciprocity theorem* (Burke, Graham-Smith, & Wilkinson, 2019).

The reciprocity theorem considers a set of two antennas, with a generator attached to antenna 1 and a measuring device connected to antenna 2; it also considers an ideal system in which no losses occur and that the antennas are oriented in such a way that the power received by the measuring device is maximum.

It can be shown that by analyzing the two antennas through Maxwell’s equations, we can obtain a result in the form of

$$U_2 \, I_1 \; = \; U_1 \, I_2 \quad , \qquad \text{(Eq. 2.1)}$$

where U_1 is the voltage induced in antenna 1 by antenna 2, with total antenna current I_1, while U_2 is the voltage induced in antenna 2 by antenna 1, with total antenna current I_2. From this result we can clearly see the strong implication of the theorem, which states that even if we exchange the generator and meter defined in Figure 2-3 we should still see the same reading in the meter. In other words, in a medium that has no preferred direction, it should not matter which antenna is receiving or transmitting and we can analyze its properties independently of the configuration (Wilson, Rohlfs, & Huettemeister, 2012).

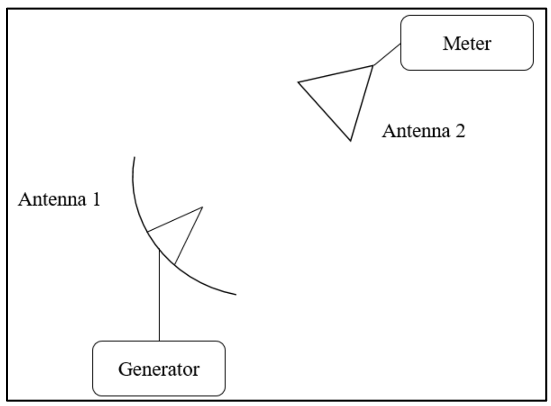

Figure 2-3. Illustration of the antenna setup in the reciprocity theorem.

The radiated electric field of a transmitting antenna can be described in terms of a power gain *G,* and by an effective area A_e for a receiving antenna (Burke, Graham-Smith, & Wilkinson, 2019). These parameters are both directional functions and are related by a fundamental relation:

$$A_e = \frac{G}{4\pi}\lambda^2 \quad \text{(Eq. 2.2)}$$

From this relation we can infer that the gain of an antenna, i.e., the measure of its capability to amplify electromagnetic radiation, is in direct proportion to its area and in inverse proportion to the wavelength squared. For most radio telescopes, this explains the need for larger collecting surfaces which allow for higher sensitivities.

Formally, the *directive power gain* G of a transmitting antenna can be defined as the power transmitted per unit solid angle in a direction given by angles (θ, φ) in spherical coordinates relative to an isotropic antenna, i.e., an ideal antenna that radiates equally in all directions (Wilson, Rohlfs, & Huettemeister, 2012). Gain values are often expressed in units of decibels (dB), so:

$$G(\theta, \varphi)_{[dB]} = 10 \log_{10} G(\theta, \varphi) \quad \text{(Eq. 2.3)}$$

The directive gain can be used to define the *antenna power pattern* or *radiation pattern* $P(\theta, \varphi)$, which consists of the angular distribution of its radiated power P and is often normalized with respect to the peak (Condon & Ransom, 2016):

$$P(\theta, \varphi) = G(\theta, \varphi)P \quad \text{(Eq. 2.4)}$$

For most radio telescopes, the power pattern of the antenna has larger power values at a certain range of angles. This range is called the *main beam*, or main lobe, while side lobes or back lobes are considered secondary lobes (Wilson, Rohlfs, & Huettemeister, 2012). The main beam is usually defined as the angular range in which the power drops by half (or -3dB) with respect to the peak, or the Full Width at Half Maximum (FWHM). An illustrative sketch of an arbitrary antenna power pattern at $\varphi = 0°$ is shown in Figure 2-4.

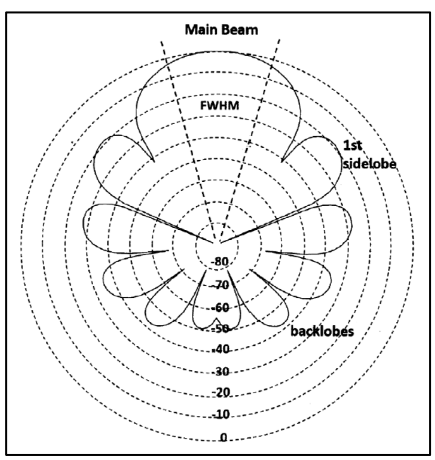

Figure 2-4. Normalized polar diagram of a power pattern in decibels.
From 'An Introduction to Radio Astronomy', by Burke, B. F.; Graham-Smith, F.; and Wilkinson, P. N., 2019.

The width of main beam can also be related to its *angular resolution*, which determines the smallest angular scale that can be resolved from a given source (Wilson, Rohlfs, & Huettemeister, 2012). Considering the case of a circular aperture of diameter *D*, the angular resolution can be typically calculated as:

$$\vartheta \approx 1.02 \frac{\lambda}{D} \quad \text{(Eq. 2.5)}$$

From the power pattern we can obtain the *antenna solid angle* Ω_A defined as the sphere surface angle where most of the power of the antenna is contained (Burke, Graham-Smith, & Wilkinson, 2019). The antenna solid angle can be calculated as the integral over the full sphere of the normalized power pattern $P_n(\theta, \varphi)$ with respect to the peak amplitude and is expressed as follows:

$$\Omega_A = \int_0^{2\pi} \int_0^{\pi} P_n(\theta, \varphi) \, sin\theta \, \delta\theta \, \delta\varphi \quad \text{(Eq. 2.6)}$$

Alternatively, if we consider integration only in the range of angles θ and φ that define the main beam, we instead obtain the *main beam solid angle* Ω_{MB}:

$$\Omega_{MB} = \iint_{MB} P_n(\theta, \varphi) \, \delta\Omega \quad \text{(Eq. 2.7)}$$

The antenna solid angle is associated to the *directivity D*, that relates the total power radiated over the whole sphere from an isotropic antenna —i.e., 4π— to the antenna solid angle (Wilson, Rohlfs, & Huettemeister, 2012). The directivity, frequently expressed in units of *dB*, is defined also as the maximum gain, and is expressed as follows:

$$D = \frac{4\pi}{\Omega_A} = G_{max} \quad \text{(Eq. 2.8)}$$

By replacing the value of *G* in Equation 2.2 with the equivalence formulated in Equation 2.8, we can obtain the *effective aperture*, calculated as the product between the antenna solid angle and the wavelength squared, defined in Equation 2.9.

$$A_e = \Omega_A \lambda^2 \qquad \text{(Eq. 2.9)}$$

This parameter indicates the amount of power than can be extracted by the telescope from a plane wave (Wilson, Rohlfs, & Huettemeister, 2012), or the equivalent collecting surface as 'seen' by the electromagnetic waves. From this concept, we can derive the existence of an *antenna efficiency*, which can be described as the ratio between the effective aperture and the geometric aperture A_g —i.e., the physical area of the collecting surface— (Condon & Ransom, 2016), and is expressed by:

$$n_A = \frac{A_e}{A_g} \qquad \text{(Eq. 2.10)}$$

For an ideal, uniformly illuminated aperture, the peak aperture efficiency is 1, which translates to the effective aperture being equal to the physical area of the collecting surface. In practice, the aperture efficiencies of most radio telescopes are below 70%, with few exceptions that can reach efficiencies up to 80% (Condon & Ransom, 2016).

Another measure of radio telescope efficiency can be obtained relating the solid angles of the antenna and the main beam, the *main beam efficiency*. This parameter indicates the fraction of power radiated by the antenna that is concentrated in the main beam; equivalently, a higher main beam efficiency means that more power is received from the telescope's main beam instead of secondary lobes. Main beam efficiency is expressed by the following relation:

$$n_B = \frac{\Omega_{MB}}{\Omega_A} \qquad \text{(Eq. 2.11)}$$

Attempting to maximize the power received by the antenna feed —and, thus, maximize the overall efficiency of the telescope— requires collecting radiation from the center of the reflector with the equal efficiency as from the edges. However, such an abrupt transition from full illumination of the reflector at the center, to zero just outside the edges is usually the main cause of larger secondary lobes. While sidelobe amplitudes can be orders of magnitude below that of the main beam, it is an undesired contribution that can still pick up radiation from other sources (Burke, Graham-Smith, & Wilkinson, 2019). The most common form of attenuating sidelobes consists of limiting the power received by the antenna near the edges, which is referred as a taper. This implies a reduction in the effective aperture of the telescope and in resolution. Thus, radio telescope design frequently becomes a trade-off between high efficiency and controlled sidelobes.

A side effect of applying a taper to the reflector illumination can be analyzed considering the antenna feed as a transmitting device. If the antenna feed radiates onto the reflector with power greater than zero at its edge —because of the taper going from full illumination at the center to a non-zero value at the rim—, we can conclude that some radiation from the feed will 'spill' over the edge of the reflector. If we switch back to the perspective of reception, we can see that this effect traduces into radiation coming from the back of the reflector and being received by the antenna. This effect is appropriately referred to as *spillover* and is typically defined as the portion of power that a telescope receives from the ground (Burke, Graham-Smith, & Wilkinson, 2019).

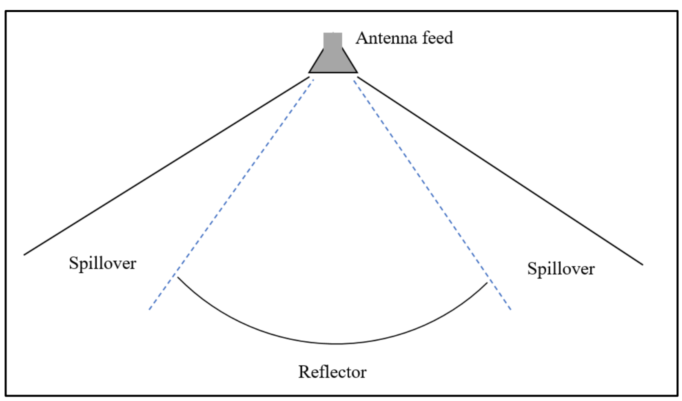

Figure 2-5. Sketch of spillover in a radio telescope.

As the sensitivity of experiments increases, proper characterization of the effects of sidelobes and spillover becomes more important. For instance, sidelobe contamination can occur even at tens of degrees from bright sources, while the contribution from the spillover varies with different elevations as the observed section of the ground changes (Stevens, et al., 2018).

2.1.1.1. Polarization in radio telescopes

Cosmic astronomical sources can be studied in polarization as well as intensity, which constitutes a fundamental advantage of radio astronomy. Polarization of electromagnetic waves can be defined simply as the preferred direction of oscillation of the electric field component of the wave. Any measure of polarization from celestial objects implies a preferred direction of the medium or source emission and can allow us to study sources such as the thermal emission from the CMB, synchrotron radiation from radio galaxies, among others (Burke, Graham-Smith, & Wilkinson, 2019).

Let us consider the instantaneous transverse electric field E of a monochromatic electromagnetic wave traveling in the $\hat{z}$ direction, perpendicular to the x-y plane (Condon & Ransom, 2018):

$$\vec{E} = \left[\hat{x}E_x \exp(i\phi_x) + \hat{y}E_y \exp\left(i\phi_y\right)\right]\exp\left[i(\vec{k}\cdot\hat{z} - \omega t)\right] \quad \text{(Eq. 2.12)}$$

Where the wave number $k = 2\pi/\lambda$ is defined as the magnitude of the wave vector $\vec{k}$ pointing in the direction of propagation; $\omega = 2\pi\nu$ is the angular frequency; and $\delta = \phi_x - \phi_y$ is the phase difference between the orthogonal fields E_x and E_y.

The energy of the electric field component is given by:

$$E^2 = \left|\vec{E}\right|^2 = E_x^2 + E_y^2 \quad \text{(Eq. 2.13)}$$

From Equation 2.12 we can see that a time-independent combination of phases and amplitudes results in an *elliptically polarized* wave, in which the electric field traces an ellipse in the x-y plane. For a phase difference of $\delta = 0$, the electric field vector does not rotate, and the wave is *linearly polarized*. If $E_x = E_y$ and the phase difference magnitude equals $|d| = \pi/2$, the electric field traces a circle with angular frequency ω, which constitutes a *circularly polarized* wave. Radio astronomers follow the International Astronomical Union (AIU) convention for circularly polarized waves, which designs *right-handed polarization* for clockwise rotation ($\delta > 0$) and *left-handed polarization* for counterclockwise polarization ($\delta < 0$).

A more straightforward way to analyze polarization is using the Stokes parameters, which characterizes polarization in terms of linear combinations of average power measured in different directions (Burke, Graham-Smith, & Wilkinson, 2019). The analysis of polarization with Stokes parameters is appropriate for radiation obtained from astronomical sources, whose electric field vector varies rapidly in amplitude and direction and frequently needs averaging (Condon & Ransom, 2016).

The Stokes parameters are defined as follows:

$$I = \langle E_x^2 + E_y^2 \rangle \quad \text{(Eq. 2.14)}$$

$$Q = \langle E_x^2 - E_y^2 \rangle \quad \text{(Eq. 2.15)}$$

$$U = \langle 2E_x E_y \cos\delta \rangle \quad \text{(Eq. 2.16)}$$

$$V = \langle 2E_x E_y \sin\delta \rangle \quad \text{(Eq. 2.17)}$$

The *I* parameter is the total intensity of the wave, usually associated to the co-polarization, the intended polarization of the signal, and is a measure of the tendency of the radio wave to prefer the horizontal direction (Robishaw & Heiles, 2019). It can be calculated by summing the amplitudes of the orthogonal components of the wave, i.e., adding the intensities measured at an angle of 0° and 90° with respect to the horizontal axis. The Q parameter results from the difference of power from the 0° and 90° components and can be associated to the cross-polarization, or the perpendicular component of the intended polarization of the signal. The *U* parameter can be calculated as the difference of power measured at an angle of 45° and -45°. The *V* parameter requires a measurement of circularly polarized flux and can be calculated from the difference of power measured from right-handed polarization minus power from left-handed polarization (Condon & Ransom, 2016).

From these definitions, the *polarization angle* of an electromagnetic wave, i.e., position angle of the electric field component of the wave (Burke, Graham-Smith, & Wilkinson, 2019), can then be calculated as

$$\chi_{[rad]} = \left(\frac{1}{2}\right) \arctan \frac{U}{Q} \qquad \text{(Eq. 2.18)}$$

Radio telescopes can study polarization by placing polarization sensitive devices, such as half-wave plate polarizers, in front of the detectors (or at a given point in the optical path), which results in a phase difference between the two orthogonal polarization components (Wilson, Rohlfs, & Huettemeister, 2012). Alternatively, linearly polarized detectors or feeds can be placed at a given angle to make them sensitive to polarization with that orientation.

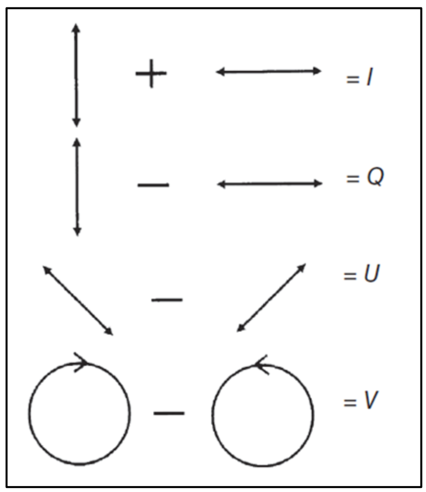

Figure 2-6. Graphical representation of the Stokes parameters.
Adapted from 'An Introduction to Radio Astronomy', by Burke, B. F.; Graham-Smith, F.; and Wilkinson, P. N., 2019.

Polarization signals typically have a low signal-to-noise ratio, which requires large bandwidths in the receiver system and adds the complexity of maintaining purity in the polarization. Other systematic contributions, such as the effects associated with the radiation pattern, polarization leakage from co-polarization to cross-polarization, or differential gain errors in the detectors, can negatively impact the measurement of polarization and require precise calibration to ensure the measure signal corresponds to the actual physical processes (Burke, Graham-Smith, & Wilkinson, 2019).

2.2. Cosmology

Cosmology is a field of study that combines natural sciences such as astronomy and physics to understand the origin and evolution of the universe (Encyclopaedia Britannica, 2021). The drive to comprehend and explain the mechanics of the universe can be dated back to Copernicus and his solar system model, or even further if we consider the complex worldviews of pre-Columbian civilizations, such the Incas or Mayas, as the earliest precursors of cosmology as we know it (Gullberg, 2020). However, modern cosmology rose from Albert Einstein's General Theory of Relativity, the first theory that allowed for an explanation of the universe that was compelling and verifiable.

The Big Bang model of the universe was developed from a series of interwoven theoretical studies and observations, including the General Theory of Relativity, the Friedman-Lemaitre-Robertson-Walker exact solutions of Einstein's equations and Hubble's observations of cepheids and receding galaxies, among others. This expanding, hotter and denser universe than previously realized poses new technical and scientific challenges, in which physics, astronomy and radio astronomy play a key role (Dodelson & Schmidt, 2020).

The main consequence of an expanding universe, as currently proposed in the Big Bang model, is that distances do not remain constant, e.g., the distance between us and a far galaxy is larger now than it was at an earlier time in history. This can be visualized through a scale factor a that describes the base metric of distance, as the universe expands, the value of a grows and thus the distance between two comoving points separated by a also increases.

Another crucial implication of the expansion of universe is the *cosmological redshift* of light, in which the wavelength is lengthened as a result of the expansion of the universe. Defining the redshift z is convenient as in cosmology it is frequent to label the time t using the redshift of light emitted at that moment, as we see it now (Carmeli, Harnett, & Oliveira, 2005). It can be defined as

$$1 + z = \frac{\lambda_{observed}}{\lambda_{emitted}} = \frac{a_0}{a(t)}, \quad \text{(Eq. 2.19)}$$

with a_o the scale factor as observed at t_0 (current time) and $a(t)$ the scale factor at given *t* time.

The takeaway from Equation 2.19 is that the farther the object, the larger its redshift will be, or, alternatively, a larger measured z implies a further object. However, the relationship between distance and redshift is not fixed as depends on the scale factor and how it changes over time (Dodelson & Schmidt, 2020).

The Hubble rate allows us to quantify the change in the scale factor and its relation to the energy content of the universe as:

$$H(t) = \frac{1}{a}\frac{\delta a}{dt}, \qquad \text{(Eq. 2.20)}$$

with its value at current time t_0 is given by $H(t0) = H_0$ in units of $km\ s^{-1}\ Mpc^{-1}$.

General relativity predicts that the scale factor is determined by the Friedmann equation in terms of energy density —i.e., energy per unit volume of the universe— as follows:

$$H^2(t) = \frac{8\pi G}{3}\left[\rho(t) + \frac{\rho_{cr} - \rho(t_0)}{a^2(t)}\right] \qquad \text{(Eq. 2.21)}$$

where G is Newton's constant; $\rho(t)$ is the total energy density of the universe as a function of time, with $\rho(t_0)$ its value today; ρ_{cr} is the critical energy density given by $3H_0^2/8\pi G \approx 10^{-29}\ g\ cm^{-3}$. The total energy of the universe can be expressed as the sum of non-relativistic matter, radiation, and a cosmological constant —such as the vacuum energy—, whose relative proportions evolve over time and from which the energy density can be obtained (Dodelson & Schmidt, 2020).

In the Friedmann models of an expanding universe, the ratio between the current energy density of the universe and the critical energy density defines the geometry of the universe at the very large scales and is expressed by

$$\Omega = \frac{\rho(t_0)}{\rho_{cr}} \qquad \text{(Eq. 2.22)}$$

A value of Ω smaller than 1 results in an open universe or positively curved space, in which two parallel lines never cross paths and diverge; a value of Ω greater than 1 results in negatively curved space in which parallel lines eventually cross paths and converge; finally, a value of Ω equal to 1 results in a universe that is said to be 'flat', in which parallel light rays will never cross paths unless affected by external influences. By most accounts, the energy density of the universe has been measured to be consistent with the critical energy density within margin of error and thus the universe if presumed flat, or Euclidean (Dodelson & Schmidt, 2020).

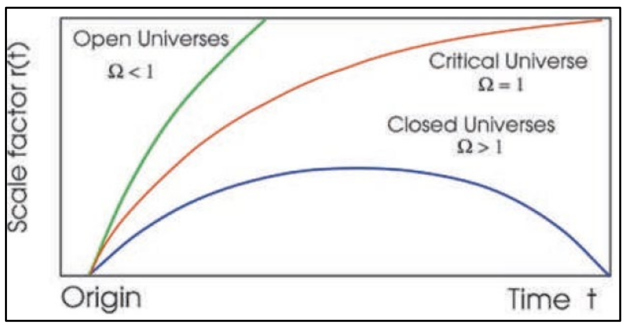

Figure 2-7. Friedmann models of the expanding universe.
From 'Introduction to Astronomy and Cosmology', by Morison. I., 2008

To solve Equation 2.21 for $a(t)$ we need to be aware of the energy content of the universe. To that end, several experiments such as the Cosmic Background Explorer (COBE), Wilkinson Microwave Anisotropy Probe (WMAP), and Planck space probes, along with other experiments from the ground, have carried out increasingly precise measurements of the energy density and distribution of matter in the universe (Smoot, 1999; Hinshaw, et al., 2013; Aghanim, et al., 2020). In parallel, more precise constraints on the Hubble Constant H_0 are being obtained through observations of standard astronomical objects (see, e.g., Dhawan, Jha, & Leibundgut, 2018 and Zhang, Jiao, & Zhang, 2019). The latest estimates have narrowed the Hubble constant to $H_0 \approx 73\ km\ s^{-1} Mpc^{-1}$ which leads to a universe roughly 13.8 billion years old.

The standard Big Bang model of an expanding universe predicted sufficiently well several of the conditions seen today. However, the most notable inclusion to the standard model is the *inflationary epoch*, in which the universe underwent exponential expansion due to the potential energy of a slow-rolling —i.e., slowly varying— scalar field. This consolidated Big Bang model is usually referred to as the Lambda Cold Dark Matter Model (ΛCDM). The addition of inflation solved several troubling issues with the non-inflationary model, mainly the *flatness problem*, the *horizon problem,* and the *monopole problem*.

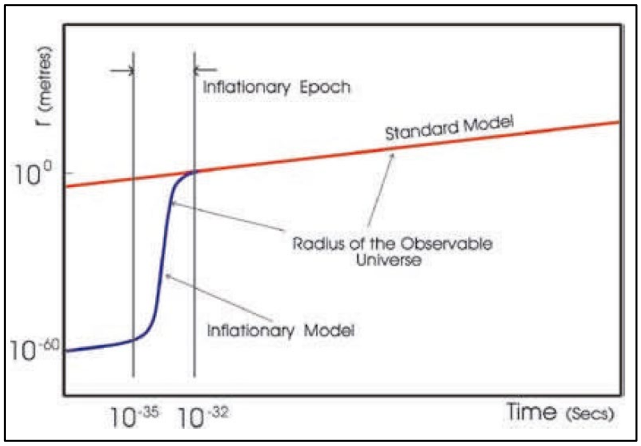

Figure 2-8. The Big Bang timeline with and without an inflationary period.
From 'Introduction to Astronomy and Cosmology', by Morison, I., 2008.

The flatness problem concerns the lack of curvature as seen on the universe today, solved through the exponential expansion that occurred during Inflation which would force the geometry of space to become flat. The horizon problem poses that, given the current size of the universe, there has not been enough time for temperature to become as homogeneous and isotropic in all directions as it is observed today. An inflationary period solves this problem as it proposes that, given that the conditions immediately before this epoch were homogeneous on a sufficiently large scale, this would result in the isotropic and homogeneous universe seen today (Morison, 2008; Dodelson & Schmidt, 2020). Finally, the monopole problem concerns unwanted exotic relics from the earlier moments of the Big Bang, as they are produced in most particle physics models at very high temperatures and apparently are not present today. These so-called magnetic monopoles should have their observed density 'diluted' by many orders of magnitude because of inflation (Durrer, 2008).

A key factor of the inflationary epoch is that some fluctuations are introduced into the homogeneous universe, the minimum of which is guaranteed by the Heisenberg uncertainty principle. During inflation, the universe is comprised of a scalar field (responsible for inflation) and a uniform background metric; it is against the latter whom the fields fluctuate due to the vacuum quantum mechanics. This scalar perturbations to the metric cause density and radiation fluctuations that are responsible for the large-scale structure of the universe that we can observe today and in the form of the Cosmic Microwave Background Radiation temperature fluctuations. Moreover, inflation should also generate tensor fluctuations in the metric of the universe, i.e., *gravitational waves*. These waves are perturbations produced by the vacuum fluctuations of gravity during inflation, which modify the amplitude of the angular power spectrum for very small scales —or a large multipole moment l in spherical harmonic decomposition— and, contrary to scalar fluctuations, are not manifested in the density. The anisotropies introduced by gravitational waves constitute a unique signature of inflation and thus are of utmost interest for validating and constraining the physics behind inflation (Dodelson & Schmidt, 2020).

2.2.1. The Cosmic Microwave Background Radiation

In 1948, physicist George Gamow stated that a 'sea of thermal radiation' must had mediated the formation of elements in the early universe, whose results should be dependent on the temperature of the radiation as detected at present time. This is the initial reference of what would later be known as the Cosmic Microwave Background Radiation, the leftover radiation that is the earliest light in the universe (Morison, 2008).

At sufficiently early times in the Big Bang, reaction rates for particle interactions were much faster than the expansion rate, so it can be assumed that the medium was in thermal equilibrium and the expansion can be assumed adiabatic. At this time, the temperature and density were too high for neutral atoms or bound nuclei to exist, with temperatures in the order of $10^{10}\ K$, vast amounts of thermal radiation permeated the environment and high-energy photons destroyed any atom or nucleus produced. Thus, free electron density was so high that the mean free path of photons was very short due to Thomson scattering, and the early universe plasma was opaque to electromagnetic radiation. As the universe cooled down below typical nuclear binding energies, light elements, such as Helium and Deuterium, began to form in the process known as Big Bang Nucleosynthesis (BBN). When temperature of the early universe decreased to approximately $4000\,K$, free electrons and protons combined into neutral hydrogen in what is referred to as the *recombination epoch* of the universe (Durrer, 2008).

During recombination, the free electron density drops greatly, and the mean free path of photons grows larger than the Hubble scale —the volume around an observer beyond which objects recede from the observer faster than the speed of light—. The electrons captured by protons in the recombination process are mostly in a higher energy state due to higher recombination efficiencies, which tips the ratio of ground-state to high-state energies of captured electrons in neutral hydrogen nuclei in favor of the latter. These electrons soon decay into their ground-state, emitting photons than can travel freely, which is referred to as *decoupling*. Thus, at T ~ 3000 K and t ~ 380,000 years (z ~ 1100), the photons finally have decoupled from the electrons and the universe is transparent, so the background radiation of the early universe is established (Dodelson & Schmidt, 2020; Durrer, 2008).

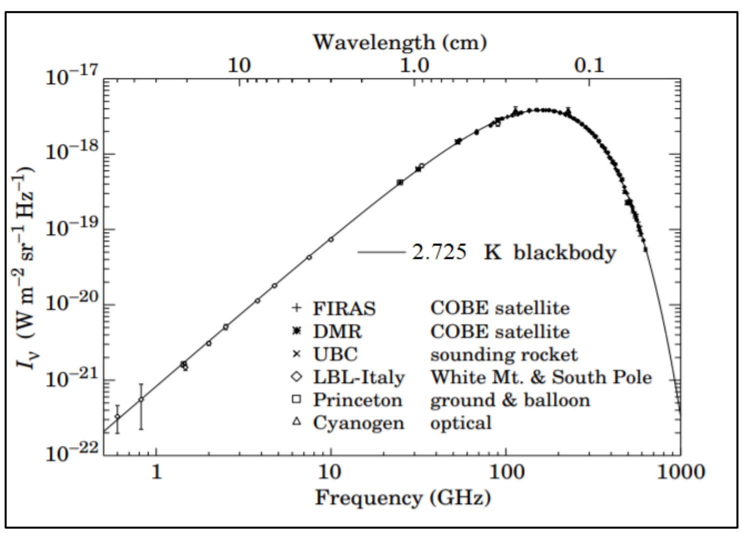

Figure 2-9. The spectrum of the Cosmic Background Radiation as measured by several sources. Modified from "The Cosmic Microwave Background Spectrum" by Smoot, G., 1997.

By the conditions set at the early Big Bang, such as thermal equilibrium, the background radiation spectrum corresponds to a blackbody at T ~ 3000 K. From that moment, the universe has expanded roughly 1000-fold and, due to cosmological redshift, the background radiation's wavelength has been lengthened, shifting the radiation to an equivalent blackbody temperature of 2.725 K (Fixsen, 2009), with its peak sitting at the far infrared and millimeter wave range; thus, it is referred to as the Cosmic Microwave Background (CMB) Radiation.

Despite this accurate fit to a blackbody spectrum (see Figure 2-9), the CMB is not completely uniform when mapped with sufficient precision and resolution, as can be seen in the CMB map in Figure 2-10. At an age of 380,000 years, the universe was uniform to roughly 1 part in 10^5, which constitutes the typical amplitude of temperature fluctuations seen in the CMB (Dodelson & Schmidt, 2020).

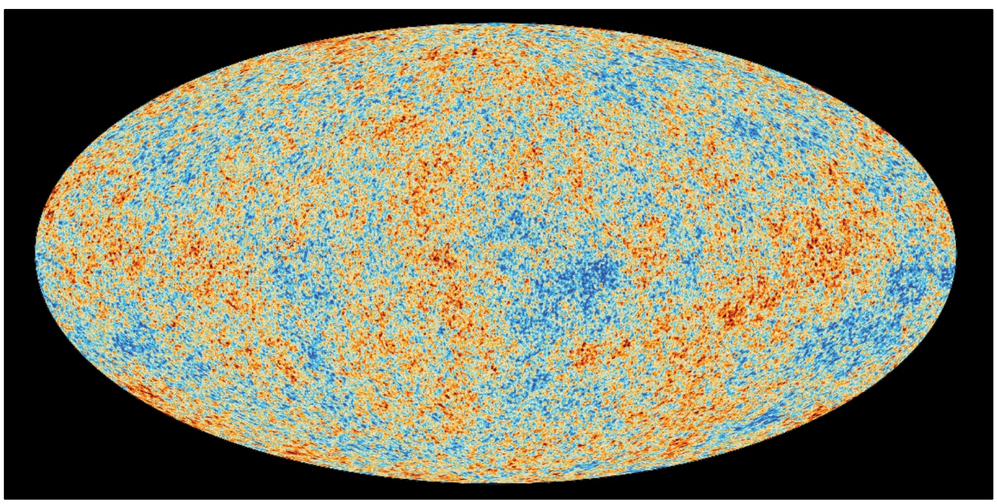

Figure 2-10. The CMB anisotropies as mapped by the Planck satellite.
The temperature scale is in the range of ±300uK.
From 'The Cosmic Microwave Background: temperature and polarization', by the European Space Agency (ESA), 2018.

Current Cosmology experiments attempt to measure this background radiation with increasing precision and varied angular resolution, aiming at determining whether the observed anisotropies are consistent with the matter-density perturbations required to form the observed structure today. Moreover, parameters for cosmological models can be constraint from measurements, which include: the fractional density of matter in the universe $\Omega_m = \Omega_b + \Omega_c$ —the sum of contributions from baryonic (ordinary matter) and cold dark matter—; the fractional density of vacuum energy Ω_Λ; the total energy density $\Omega = \Omega_m + \Omega_\Lambda$; the Hubble constant; and the amplitude and spectral index of the primordial power spectrum density fluctuations (Balbi, 2000). An example of the determination of such constraints can be seen in Figure 2-11.

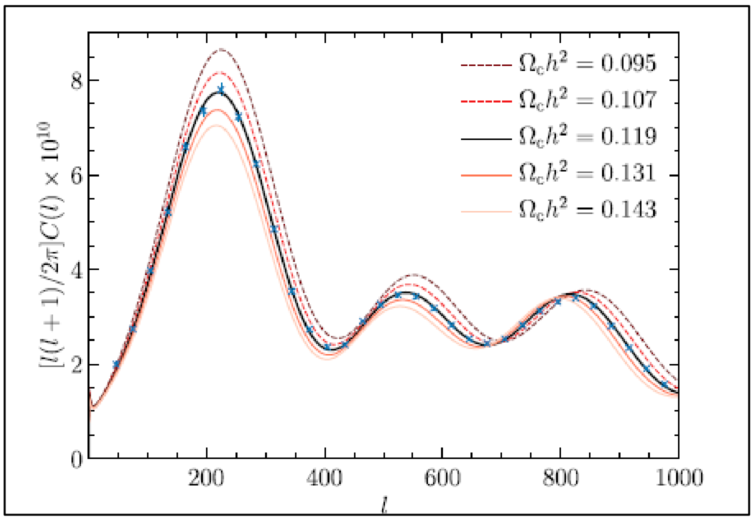

Figure 2-11. Planck measurements of the angular power spectrum and predictions for varying values of Ω_c. From 'Modern Cosmology', by Dodelson, S. & Schmidt, F., 2020.

The CMB is also characterized by polarization anisotropies that arise from scattering just before decoupling, which effectively doubles the available information regarding the scalar perturbations of inflation. Moreover, gravitational waves produce a particular pattern of polarization in the CMB that scalar perturbations cannot, which makes polarization a unique way of searching for gravitational waves produced during inflation. Polarization of the CMB signal can be divided into E-modes and B-modes, which have different properties: E-modes vary in strength in the same direction as, or perpendicular to its orientation; B-modes vary in strength in 45° angles from its orientation (Dodelson & Schmidt, 2020), illustrated in Figure 2-12.

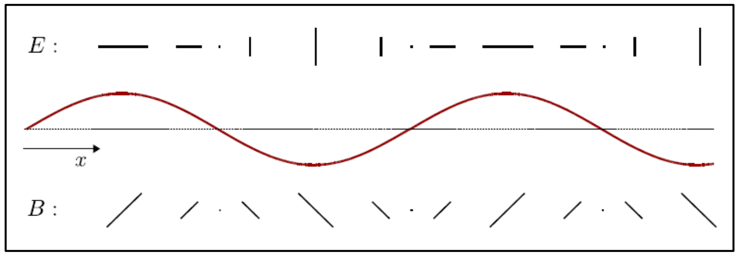

Figure 2-12. Polarization generated by a single plane-wave perturbation along the x-axis, and E (top) and B (bottom) mode behavior.
From 'Modern Cosmology', Dodelson, S. & Schmidt, F., 2020.

For a superposition of plane waves in the x-y plane, with equal amplitude, wavelength and phase, the resulting polarization patterns should look like those shown in Figure 2-13. This shows that E and B modes have even and odd parity, respectively —i.e., E-modes preserve their symmetry under spatial inversion, while B-modes do not. The behavior of these components of the polarization should make them particularly easy to spot in a polarization map.

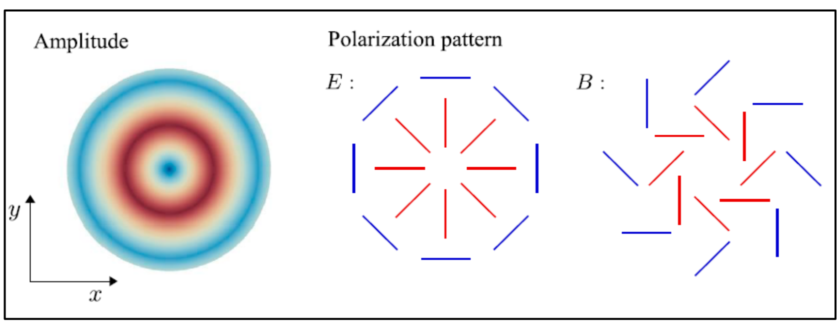

Figure 2-13. Polarization patterns generated by a radial wave in the x-y plane.
From 'Modern Cosmology', Dodelson, S. & Schmidt, F., 2020.

The relation between E-modes with scalar perturbations and B-modes with tensor perturbations is evident, as the photon distribution associated with tensor perturbations is not rotationally symmetric about the direction of the wavevector of the perturbation — i.e., gravitational waves are expected to produce B-mode polarization in addition to E-modes—.

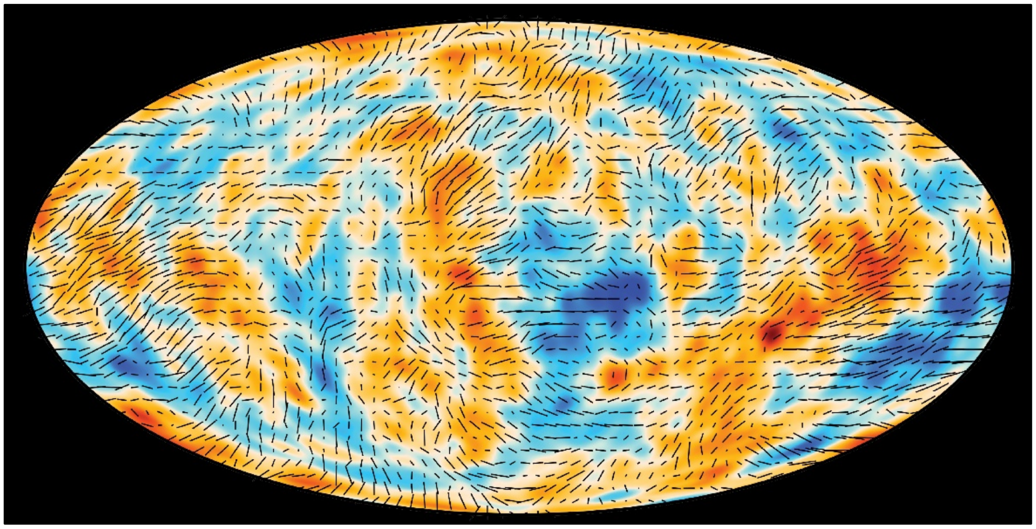

Figure 2-14. Planck satellite's measurements of large scale CMB anisotropies overlayed with the polarization map. From 'The Cosmic Microwave Background: temperature and polarization', by the European Space Agency, 2018.

The main limitations in the detection of E and B-modes are their relative amplitudes compared to the main temperature signal. The primordial B-mode polarization component is expected up to at least 6 orders of magnitude below the main temperature signal at angular scales of $l \approx 80$, as seen in Figure 2-15; thus, a high-sensitivity and high-resolution polarization map is required to optimize the spectrum reconstruction (Kamionkowski & Kovetz, 2016). In practice, detector noise and foreground contributions to the CMB polarization make this task a complicated one. Moreover, an absolute calibration of the polarization angle is critical, as associated errors can leak from the much larger E-modes to the B-modes (Aumont, Ritacco, Macías-Pérez, Ponthieu, & Mangilli, 2020). At tensor-to-scalar ratios of $r = 0.002$ (with r defined as the ratio of the B-mode to E-mode power spectra), at which the gravitational lensing B-modes are much larger than primordial B-modes, the absolute angle polarization must be calibrated to better than 0.2° accuracy (Abitbol, et al., 2020).

The stringent requirements outlined earlier are not exclusive to gravitational waves, as the so-called *cosmic birefringence* requires strict polarization angle calibration to ensure the detection of a very slight rotation in the linear polarization of the CMB, denoted as β. Cosmic birefringence should arise from the coupling of CMB photons to particles and fields that deviate from the standard model of cosmology, which should produce nonzero correlations in the power spectrum between E and B polarization (EB) components and between Temperature and B-modes (TB). Again, observing such paradigm changing phenomenon can be limited by current calibration procedures in the absolute polarization angle of the instruments, whose inaccuracies could mask such effects (Grain, Tristram, & Stompor, 2012; Minami & Komatsu, 2020).

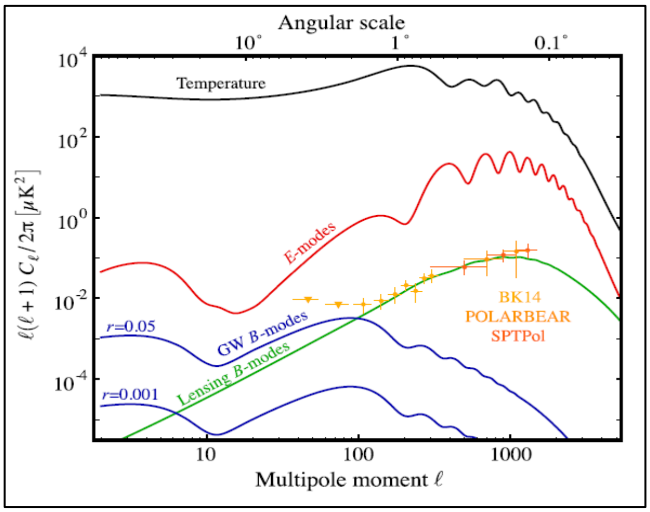

Figure 2-15. Expected amplitudes of the CMB signals.
Lensing B-modes are produced by gravitational lensing when signals pass near massive bodies.
From 'Modern Cosmology', Dodelson, S. & Schmidt, F., 2020.

As stated earlier in this chapter, water vapor is responsible for most of the limitations of ground based CMB observations. This explains the need for ad-hoc space faring observatories such as the Planck satellite. However, at privileged geographical locations with low precipitable water vapor levels, such as the Atacama Desert in northern Chile, at altitudes above 5000 meters, observations at millimeter and sub-millimeter wavelength can be carried out and CMB experiments with access to varied angular scales have been established. Among these, we find projects such as the Atacama Cosmology Telescope (ACT)[1], the POLARBEAR[2] experiment and the Cosmic Large Angular Scale Surveyor (CLASS)[3] observatory.

[1] https://act.princeton.edu
[2] https://bolo.berkeley.edu/polarbear/
[3] https://sites.krieger.jhu.edu/class/

It is the CLASS experiment to which this thesis work expected to have access to perform proof-of-concept testing of the drone-based calibrator; however, due to conditions associated with the COVID pandemic, these on-site tests had to be postponed. Nevertheless, electromagnetic simulations of its 150 GHz camera were performed to gain insight into the possible effects of a prospective flight at the CLASS site —where the source is expected to be ultimately tested— and are detailed in Chapter 3.

2.3. Radio Telescope Calibration Methods

Radio telescopes, as any other measurement device, must be calibrated to ensure the physical quantities are accurately represented by the instrument's measurements. For a telescope, calibration also refers to the process of determining the set of parameters that describe its behavior, such as the ones outlined in the first section of this chapter.
For smaller antennas, such as the ones used for telecommunications, calibrations are carried out in anechoic chambers with test stands that rotate the antennas in azimuth and elevation against a very well characterized transmitter (Wilson, Rohlfs, & Huettemeister, 2012). This is usually performed at a distance *d* in the far field region of the antenna to obtain easily interpretable results, such that

$$d > \frac{2D^2}{\lambda} \qquad \text{(Eq. 2.23)}$$

For modern radio telescopes, performing this kind of measurements is complex due to their current sizes. For example, a 6-meter diameter telescope operating at a frequency of 145 GHz —such as the Atacama Cosmology Telescope— results in a far-field distance of roughly 36 kilometers. It becomes extremely complicated to accommodate for such a setup for calibrations that must be executed in a routinary manner, thus, radio telescopes are usually calibrated with very well studied astronomical sources.

Using astronomical sources as calibrators sets the requirement of having calibrators available in different locations of the sky to appropriately characterize the telescope pointing —i.e., the effects related to the mechanical motion of the telescope—. Moreover, for amplitude calibrations, the flux density of the object must be very well characterized across the frequency band of interest and its time stability must be high. For polarization angle calibrations, the source must be highly polarized and equally well characterized and stable. This task becomes even more complex for polarization sensitive experiments telescopes, such as CMB experiments, due to the need of highly polarized sources in the millimeter-wave range: these sources are not abundant and they have not been sufficiently studied at the wavelengths of interest (Keating, Shimon, & Yadav, 2012; Huffenberger, et al., 2015).

For a single-dish antenna, the power as a function of frequency P_ν at the receiver input terminals is expressed as

$$P_\nu \delta\nu = \frac{1}{2} A_e S_\nu \delta\nu = kT_A \delta\nu \ , \qquad \text{(Eq. 2.24)}$$

where S_ν is frequency dependent flux in Jansky ($1\,Jy = 10^{-26}\,W\,m^{-2}\,Hz^{-1}$), k is the Boltzmann constant and T_A is the antenna temperature (expressed in Kelvin), which expresses a power level equivalent to that of a perfectly matched resistor at the given temperature (O'Neil, 2001).

The antenna temperature is a convolution of the beam pattern of the telescope with the source brightness temperature T_B. At these wavelengths, the source brightness temperature is defined as the Rayleigh-Jeans temperature of an equivalent black body which will give equivalent power per unit area per unit frequency interval per unit solid angle as the celestial source, expressed as

$$I_\nu = B_\nu(T_B) \rightarrow I_\nu^{R-J} = \frac{2\nu^2}{c^2} kT_B \ \left[\frac{\mathrm{W}}{m^2 Hz\, sr}\right] \ , \qquad \text{(Eq. 2.25)}$$

then the antenna temperature can be expressed as

$$T_A = \frac{A_e}{\lambda} \iint T_B(\theta, \phi)\, P_n(\theta, \phi) \delta\Omega \qquad \text{(Eq. 2.26)}$$

Aside from precise characterization of the antenna radiation pattern, calibration of radio telescopes usually involves determining the *sensitivity of the antenna* Γ in $K\,Jy^{-1}$ under assumptions or available information of the observed source, such as actual flux density, atmospheric effects, among others. Antenna sensitivity can be expressed in terms of the aperture efficiency and reflector diameter as

$$\Gamma = n_A \frac{\pi D^2}{8k} \quad \text{(Eq. 2.27)}$$

The measured antenna temperature $T_A{}'$ can then be expressed in terms of the sensitivity and the flux density of the source as

$$T_A' = \Gamma\, S_\nu \quad \text{(Eq. 2.28)}$$

The minimum detectable antenna temperature is related to fluctuations in the receiver output caused by the system noise. This noise is directly proportional to the system temperature T_{sys}, which represents the equivalent temperature of added noise, including the receiver electronics noise (due to physical temperature of the antenna components), effects of the reception chain, telescope spillover, atmospheric emission, among others (O'Neil, 2001; Wilson, Rohlfs, & Huettemeister, 2012). System temperature can then be defined as

$$T_{sys} = T_{bg} + T_{atm} + T_{spill} + T_{loss} + T_{rx} \quad \text{(Eq. 2.29)}$$

where T_{bg} corresponds to the CMB background and galactic emission, T_{atm} corresponds to atmospheric emission, T_{spill} corresponds to spillover and scattering, T_{loss} can be attributed due to losses in the reception chain and T_{rx} is the receiver noise temperature. The background, spillover and atmospheric components are usually consolidated as $T_A{}'$, while the reception chain losses are usually incorporated into T_{rx}. From these components, the background temperature, atmospheric emission, and spillover vary with the position in the sky, i.e., its value changes depending on the coordinates at which the telescope points during observations (Gary, 2019). Frequently, the sky emission component can be expressed as a function of the opacity at the zenith and the elevation angle as

$$T_{atm} = T_{atm}(1 - e^{-\tau_o \csc(el)}) \qquad \text{(Eq. 2.30)}$$

If the system temperature is known, the sensitivity or aperture efficiency can then be determined from measurements of a calibrator source (O'Neil, 2001). The sensitivity of a radio telescope can then be expressed in terms of the RMS noise fluctuations of the system T_{RMS}, which can be expressed as

$$\Delta T_{RMS} = \frac{K_s T_{sys}}{\sqrt{\Delta \nu \, t \, n}} \qquad \text{(Eq. 2.31)}$$

where K_s is a sensitivity constant of the telescope —dimensionless and of order unity—, $\Delta\nu$ is the detection bandwidth, t is the integration time for one sample and n is the number of averaged samples. The minimum detectable temperature is typically considered to be 3-5 times the RMS noise temperature, i.e., $\Delta T_{min} = 3\,T_{RMS}$ (O'Neil, 2001). The minimum detectable temperature can also be expressed as a minimum brightness or flux density.

In practice, source temperature can be separated from the system temperature from two observations: one with the source and one without it. These measurements are typically referred to as on-source and off-source, respectively. Thus, the source temperature can be expressed as

$$T_{source} = T_{on} - T_{off}\ , \qquad \text{(Eq. 2.32)}$$

from which the system temperature can then be determined.

At centimeter wavelengths, the typical calibration procedures involve obtaining the system temperature mainly from two techniques: *switched noise diode* and *hot and cold loads*. The switched noise diode requires coupling a noise diode with a known effective temperature T_{CAL} at the frequency of interest. Then, while pointing at the cold sky, measurements with the diode on CAL_{on} and with the diode off CAL_{off} are carried out. The off-source system temperature can then be determined from these measurements, considering the ratio of the off-source to diode temperature measurements as

$$\frac{T_{off}}{T_{CAL}} = \frac{CAL_{off}}{CAL_{on} - CAL_{off}} \qquad \text{(Eq. 2.33)}$$

and finally

$$T_{off}[K] = \frac{CAL_{off}}{CAL_{on} - CAL_{off}} T_{CAL}[K] \qquad \text{(Eq. 2.34)}$$

The hot and cold loads method for obtaining system temperature considers a cold load in the form of an absorbing system placed inside a liquid or gas at a known temperature, e.g., liquid nitrogen. This load is then coupled to the receiver and the power level is measured. The hot load is usually at ambient temperature and a similar measurement is performed. Alternatively, the hot load can be an absorbing system placed in a liquid at a given temperature and the cold load can be an empty patch of sky. These measurements can be then used to obtain the system temperature. The advantage of the hot and cold loads method is that there are no conversions required, as both the measurements and the loads are in units of temperature (O'Neil, 2001).

An approach analogous to the previous methods is referred to as the *Y-method* or cold calibration, which allows us to determine the receiver temperature directly (Issaoun, et al., 2017). This method involves using two sources or loads, such as well characterized celestial objects or noise diodes, with known effective temperatures T_{hot} and T_{cold}. The ratio of the measured power of the two sources is given by

$$Y = \frac{C_{hot}}{C_{cold}} \,, \qquad \text{(Eq. 2.35)}$$

where the Y-factor is calculated as a ratio between the analog to digital converter (ADC) counts C for the hot and cold loads. The receiver noise temperature is then determined by the expression shown in Equation 2.36.

$$T_{rx} = \frac{T_{hot} - Y\, T_{cold}}{Y-1} \qquad \text{(Eq. 2.36)}$$

At the millimeter and sub-millimeter wave range, the chopper calibration is commonly used for obtaining the system noise temperature, as detailed in Issaoun's work (Issaoun, et al., 2017). An ambient temperature load T_{hot} with properties similar to a blackbody is placed in front of the receiver, blocking everything but the receiver noise. By making $T_{hot} \sim T_{atm}$, this method can compensate for the rapid changes in the mean atmospheric absorption, which is a concern at these wavelengths. This method attempts to obtain the effective sensitivity of the system and not a comparison of the contributions to system noise of the receiver and the sky. The effective noise temperature T^*_{sys} can be then calculated as

$$T^*_{sys} = T_{hot} \frac{C_{sky}}{C_{hot} - C_{sky}} \qquad \text{(Eq. 2.37)}$$

where C stands for the ADC counts for the ambient temperature load and the sky (considered for this instance as emission from the atmosphere).

When the blocker is in place, the measured temperature T_{block} is defined by

$$T_{block} = T_{rx} + T_{hot}\ , \qquad \text{(Eq. 2.38)}$$

and the off-source temperature is rewritten as the system noise temperature while considering $T_{sky} \approx T_{atm}(1 - n_1 e^{-\tau})$, from which we obtain

$$T_{off} = T_{rx} + T_{sky} = T_{rx} + T_{atm}(1 - n_1 e^{-\tau})\ , \qquad \text{(Eq. 2.39)}$$

where τ is the opacity in the line of sight and n_1 is the forward efficiency, which represents the fraction of power received from the forward portion of the antenna beam $n_1 = P_{2\pi}/P_{4\pi}$ (Marcelino, 2016).

We can rewrite Equation 2.37 in terms of temperature as

$$T^*_{sys} = T_{hot} \frac{T_{off}}{T_{block} - T_{off}} \rightarrow T_{hot} \frac{T_{rx} + T_{sky}}{(T_{rx} + T_{hot}) - (T_{rx} + T_{sky})} \qquad \text{(Eq. 2.40)}$$

By assuming $T_{hot} \approx T_{atm}$ the previous equation is simplified to

$$T^*_{sys} = \frac{T_{rx}+T_{atm}(1-n_1 e^{-\tau})}{n_1 e^{-\tau}}\,, \qquad \text{(Eq. 2.41)}$$

and by replacing T_{sky} into Equation 2.41 and reordering, we finally obtain

$$T^*_{sys} = \frac{e^{\tau}}{n_1}\left(T_{rx} + T_{sky}\right)\,, \qquad \text{(Eq. 2.42)}$$

If we consider that the system temperature can be defined in terms of the effects of the receiver and the noise added from the sky, i.e., $T_{sys} = T_{rx} + T_{sky}$, we then obtain an expression that relates system temperature to atmospheric effects that can be expressed as follows

$$T^*_{sys} = \frac{T_{sys}}{n_1 e^{-\tau}} \qquad \text{(Eq. 2.43)}$$

With the flux density, system temperature and sensitivity calibrations, the focus of calibrations becomes the characterization of the main beam and sidelobes. To map the main beam, several measurements of such objects must be carried out, taking in consideration the relative sizes of the source and the expected beamwidth of the telescope, the latter of which can be calculated through Equation 2.5. As stated earlier, well characterized sources, such as planets or satellites, can be used to perform calibration procedures. This is especially true for CMB telescopes, in which the methods described earlier do not perform well due to the high sensitivity and limited dynamic range of the detectors.

For compact sources, where the source angular size is smaller than the beamwidth, the process of calibration involves deconvolving the source shape from the beam pattern (Wilson, Rohlfs, & Huettemeister, 2012). This can be simplified by the assumption of a gaussian beam and a gaussian shaped source (equivalent to a sum of gaussians), which relate according to the following expression

$$\theta_o^2 = \theta_s^2 + \theta_b^2 \qquad \text{(Eq. 2.44)}$$

where θ_o corresponds to the resulting angular size, θ_s corresponds to the source angular size and θ_b corresponds to the telescope beamwidth. By relating the measured antenna temperature to the main beam temperature via the main beam efficiency, i.e., $n_B = T_A'/T_{MB}$, the actual source brightness temperature can be obtained as follows:

$$T_S = T_{MB} \frac{\theta_s^2 + \theta_b^2}{\theta_s^2} \qquad \text{(Eq. 2.45)}$$

For extended sources, the process is more complex due to the side lobes receiving power from the source as well (Wilson, Rohlfs, & Huettemeister, 2012). This usually results in the need of a source with uniform brightness temperature T_B over a solid angle Ω_s, from which the measured antenna temperature can be calculated as

$$T_A' = n_B \frac{\int_{source} P_n(\theta,\varphi)\delta\Omega}{\int_{main\ lobe} P_n(\theta,\varphi)\delta\Omega} T_B = n_B f_{beam} T_B \ , \qquad \text{(Eq. 2.46)}$$

where $f_{beam} = \frac{\Omega_{source}}{\Omega_{source} + \Omega_B}$ is the beam filling factor for gaussian shaped beam and sources.

While main beam estimation is a relatively straightforward process, estimating the sidelobe contribution to the measured temperature is a more complicated matter. This usually requires either experimental measurements to characterize the sidelobes or resource heavy computer simulations to estimate these effects. Conventional scans of point sources become less effective as the sidelobe amplitudes can be up to -30dB below the main beam, which restricts sidelobe calibration source to ones with high brightness. Moreover, depending on the telescope, pickup from other sidelobes pointed at unwanted hot sources could be in the same order of the measurement of interest. For example, the beamwidth of the CLASS telescope at 40 GHz is estimated at 1.5°, while the sidelobe peaks of -25dB are located at ~2.5° from boresight, no more than 1.75° away from the main beam.

For more complex telescopes and more sensitive surveys such as CMB experiments, the challenge lies in attaining the required level of accuracy in a theoretical model that can account for several effects such as multiple reflections, spillover, diffraction, and scattering. Computer simulations, on the other hand, can achieve such requirements but, in practice, due to non-idealities —e.g., mechanical defects, misalignments or thermal effects—, these simulations by themselves may fail to replicate the actual complex interactions of the instrument's structures. Using combined methods such as photogrammetry measurements of the mechanical setup of a telescope on top of computational simulations has had good results that can serve as a first-order approximation to predict sidelobe patterns, despite not capturing all diffraction effects, as seen in Gallardo's work (Gallardo, et al., 2018).

For polarization angle calibrations, highly polarized sources are required, with Taurus A (Tau A), a supernova remnant, being extensively used as a main polarization calibrator. However, the polarization angle of Tau A has been calibrated at best to $\pm 0.27°$ at the millimeter wavelengths (Aumont, Ritacco, Macías-Pérez, Ponthieu, & Mangilli, 2020), which allows for the study of CMB B-modes at $r \geq 10^{-2}$ and would allow the detection of cosmic birefringence for $\beta \gtrsim 0.3$. Moreover, Tau A is not a point-like source, and its frequency spectrum has not been studied within the band of most polarization sensitive projects (Nati, et al., 2018). Other polarized sources, such as Centaurus A, have been characterized to similar levels (Zemcov, et al., 2009).

2.3.1. Alternative calibration methods for CMB telescopes

As seen earlier, polarized CMB experiments require more strict calibrations to avoid systematic effects, but conventional radio telescope calibration methods do not perform appropriately on this kind of telescopes. As alternatives for CMB telescopes, recent proposed methods of polarization angle calibration (Nati, et al., 2018; Aumont, Ritacco, Macías-Pérez, Ponthieu, & Mangilli, 2020) include the following:

- ground calibration, the mechanical calibration of the polarization angle prior to observations, which is subject to potential thermal and environmental effects of up to 1° (Nati, et al., 2018);
- self-calibration, that assumes the EB, and TB correlations are zero (as per the

standard ΛCDM model) and adjusts polarization angle calibration accordingly, but loses the ability to effectively probe for cosmic birefringence;

- sky-source calibration, which uses celestial sources, such as Tau A, as a polarization angle reference, which is heavily dependent on the knowledge of the reference source (accuracy, frequency dependence, time variability, extent of the source, etc.) and, as seen, is ultimately limited in accuracy; and
- external, artificial calibration sources, which can be ground-based (Navaroli, et al., 2018), or airborne such as stratospheric balloons (Nati, et al., 2018) or satellites (Johnson, et al., 2015). Cost and the lack of previous work on these methods are listed as their drawbacks.

While some ground-based external calibration sources have achieved a high degree of polarization accuracy (Navaroli, et al., 2018), these still have to deal with the possibility of detector saturation at lower altitudes from erratic ground pickup, mostly due to a lack of featureless horizon at CMB sites (Stevens, et al., 2018). On the other hand, self-calibration, despite being able to achieve high accuracies, nullifies the possibility of exploring other cosmological phenomena, which may defeat the purpose of several CMB experiments.

Airborne sources then constitute a good alternative to overcome issues related to ground-based calibrators or other methods. For satellite calibrators, while launch prices have dropped drastically in the last few years, the cost of hardware for a CubeSat satellite calibrator can be in the order of several tens of thousands of US dollars (Liddle, Holt, Jason, O'Donnell, & Stevens, 2020); moreover, no physical access to the instrument makes it impossible to correct problems that may arise overtime —or adapt for new technical requirements— and the observation of the calibrator is subject to its orbit. The use of stratospheric balloons is another option that promises very high accuracies, but it incurs in a longer preparation time in the order of hours to reach proposed altitudes and the calibrator can be available for up to 2 hours before the need for another launch (Nati, et al., 2018). For larger telescopes, however, whose far-field is in the order of kilometers, this is still a suitable alternative.

Another option of airborne calibrators are drone-carried RF sources, a trend that has emerged lately due to the drop in price of increasingly advanced UAVs with access to high-accuracy GPS positioning, a wide variety of precise onboard sensors and robust stabilization systems. This alternative combines the versatility of drone flight with low costs and preparation times, while maintaining a high availability —i.e., flight missions may be extended or repeated frequently if access to several sets of batteries is available—. In the last few years, drone-based calibrators have been used for characterizing the bean pattern of smaller radio telescopes and antennas at frequencies in the order of the hundreds of megahertz up to a few gigahertz (Martínez Picar, Marqué, Anciaux, Lamy, & Ranvier, 2015; Wijinhols, Pupillo, Bolli, & Virone, 2016; García-Fernández, et al., 2017; Paonessa, Virone, Bolli, & Addamo, 2018); thus, the next step would be to extend the concept of a drone-based calibrator to CMB polarization sensitive experiments.

3. THE COSMOLOGY LARGE ANGULAR SCALE SURVEYOR (CLASS) PROJECT

The Cosmology Large Angular Scale Surveyor (CLASS) from Johns Hopkins University (USA) is a telescope array that observes the Cosmic Microwave Background over 75% of the sky from the Atacama Desert, in northern Chile, at frequency bands centered near 40, 90, 150, 220 GHz. As its name implies, CLASS measures the large angular scales between $1° \lesssim \theta \leq 90°$ ($l < \sim 200$) of the CMB polarization to constrain the tensor-to-scalar ratio at the $r \sim 0.01$ level (Xu, et al., 2020). Additionally, CLASS attempts to improve constraints on the sum of neutrino masses, measure the reionization (which is expected to have occurred at $6 < z < 15$) optical depth and provide the deepest wide-sky-area galactic microwave polarization maps of the interstellar medium. Its multifrequency capabilities enable CLASS to distinguish the CMB from Galactic foreground (Xu, et al., 2020).

The CLASS telescope design is unique in that it uses a rapid front-end polarization modulation to limit the intensity-to-polarization leakage and avoid far sidelobes and other systematic effects, while using well-formed beams with low distortion and high spill efficiency that propagate through the telescope. As stated earlier in the chapter, these aspects are crucial to appropriately measure the faint amplitudes of the B-modes and to achieve the rest of CLASS' scientific goals.

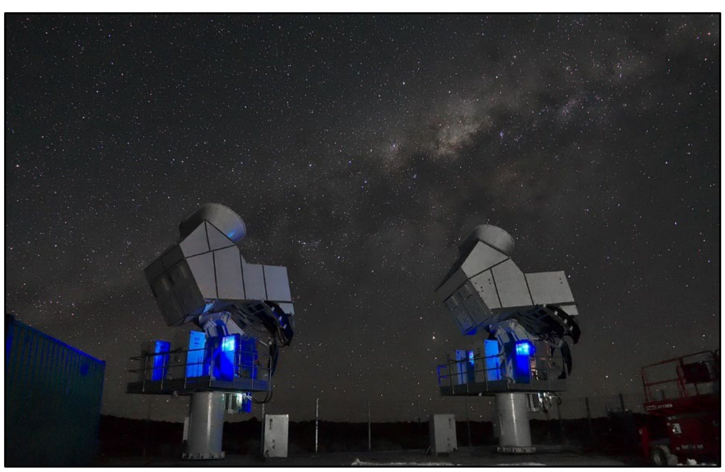

Figure 3-1. CLASS telescope array at mount Toco, San Pedro de Atacama, Chile. Image by Petroff, M. (Johns Hopkins University), 2019

The CLASS array consists of two telescopes of similar characteristics: the first equipped to observe the 40/90 GHz bands and the other for the 150/200 GHz bands. The base optical design of both telescopes is similar, which allows us to make a general description of the telescopes based on the available technical documents for the 40 GHz optical design (Eimer J. , et al., 2012).

The first optical element of the telescopes is the 60-cm diameter Variable-delay Polarization Modulator (VPM) which allows CLASS to discern the CMB signal from telescope and atmospheric drift in the form of $1/f$ noise. After hitting the VPM, light rays meet the primary and secondary mirrors and are redirected through a Zotefoam window (laminated sheets of HD30, a closed cell polyethylene foam with several advantageous optical properties) to a cold stop, at which the waves arrive as aberration-free near-spherical waves and suffer apodization. The reimaging optics, constituted by two subsequent High-Density Polyethylene (HDPE) lenses, are tasked with re-imaging these spherical waves to a flat surface at the focal plane. Finally, the waves are collected by antenna horns coupled to Transition-Edge sensors at the detector plane. The detectors themselves are paired in 45° and -45° angles and are cooled to ~40 mK by a dilution refrigerator. This enables the telescope to obtain the extreme sensitivities required to accurately measure the polarization signals of the CMB. Moreover, this pairing of detectors allows the telescope to perform differential measurements that cancel out common mode power.

As part of the strategy to measure the polarization signal projected onto different orientations, boresight rotation within a 90° range is included (in addition to conventional azimuth (*az*) and elevation (*el*) motions) and cycles through 7 angles between -45° and 45° while maintaining an elevation of 45°.

The CLASS telescope polarization angle determination is carried out using removable wire-grid polarization calibrators. During calibration operations, a polarization calibrator, whose polarization angle is known with high precision, is installed in front of the VPM and partially polarizes the incoming light. This grid can be rotated, providing polarization signals with customizable linear polarization direction.

However, the polarization angles measured through this method are in the near-field region of the telescope —where non-radiative behaviors dominate— whereas the polarization angles in the sky are in the far-field region. Even though far-field polarization angles can be estimated from the near-field measurements, the ideal scenario would require measurements of far-field polarization calibration sources (Xu, et al., 2020). This calls for the use of celestial objects as angle calibrators or other highly polarized sources in the far field. Thus, CLASS is established as an excellent candidate for testing and using the proposed drone-based calibrator as a highly polarized source in the far-field.

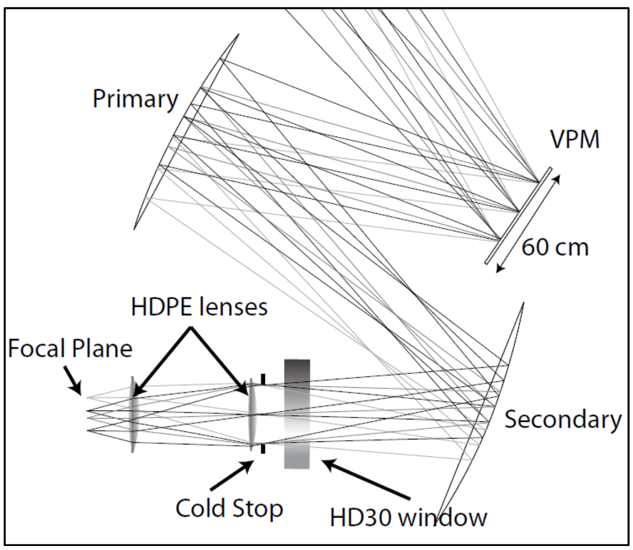

Figure 3-2. Diagram and ray tracing of the 40 GHz CLASS telescope optics.
From 'The Cosmology Large Angular Scale Surveyor (CLASS): 40 GHz optical design', Eimer, J., Bennet, C. L., Chuss, D. T., Marriage, T., Wollack, E. J. and Zeng, L., 2012.

3.1. Design of the 150 GHz optics electromagnetic simulations

The electromagnetic simulations of the CLASS telescope were carried out with the General Reflector Antenna Software (GRASP) package from TICRA. This tool allows for complex simulations of near field and far field electromagnetic waves, ray tracing of optical paths, physical optics simulations, among others.

To simulate the CLASS 150 GHz camera in GRASP, the specifications of the optics were obtained from a OpticStudio (Zemax) file provided by Joseph Eimer, Research Scientist at Johns Hopkins University who oversaw the optical design. As part of this thesis, the Zemax file was then translated into a GRASP optical model taking as a reference an existing 40-GHz CLASS camera optical model.

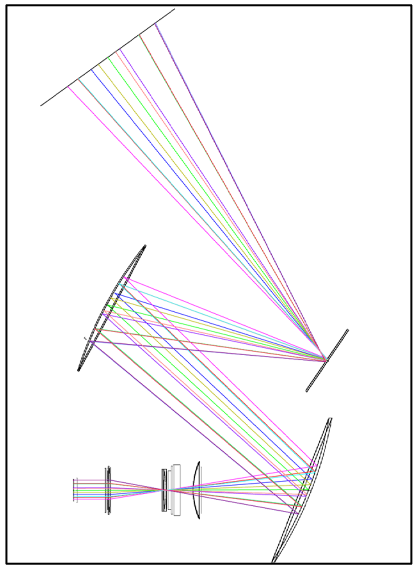

Figure 3-3. Zemax ray-traced model of the 150 GHz optics from the files provided by Dr. Eimer.

The analysis carried out in GRASP estimates currents induced in optical surfaces by electromagnetic waves and then propagates waves using the newly generated currents as a source. Thus, the entire optical path can then be simulated. The ray-traced model of the CLASS 150 GHz optics used for the simulations is shown in Figure 3-4.

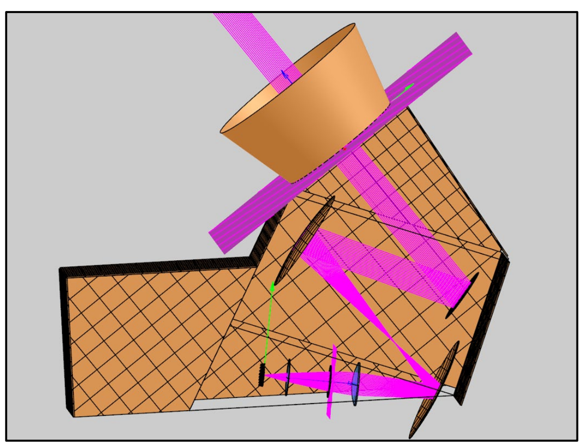

Figure 3-4. The developed GRASP model of the 150 GHz telescope optics, ray-traced for a central detector.

The simulations allow us to study the optics of the telescope and model the behavior of the resulting beam and sidelobes in the near or far field. The simulations analyze the telescope from the perspective of transmission, thus, the receiving horns act as emitters which propagate the rays through the rest of the optical chain. From these results, it will be possible to make conclusions about a prospective flight at the site and quantify certain effects, e.g., the optimal distance for testing the RF source, or the expected polarization efficiency of the telescope for calibration at different distances.

We can also attempt to simulate the optics for the near field regime, in which the non-radiative effects of the telescope dominate, to determine the distance at which the telescope starts resembling the far-field. Considering the VPM of the telescope as the aperture of the telescope, the theoretical distance for the far field can be calculated from Equation 2.23, with $D = 0.60\ m$ and $\lambda \approx 2\ mm$, which results in a far field distance of $d \approx 360\ m$. The VPM, however, is significantly underilluminated and its effective diameter is then smaller in order to achieve a balance between reduced sidelobes and angular resolution. From the literature (Xu, et al., 2020), the 40 GHz beamwidth is listed as ~1.5° and by estimating $\vartheta \approx 1.02\frac{\lambda}{D}$ this results in an aperture diameter of ~0.31 m. The cold stop, mostly responsible for the sub illumination of the VPM, remains unchanged for both the 40 GHz and 150 GHz optics, then, we can safely conclude that the far field distance of the 150 GHz optics will be ~193 m.

In addition to evaluating the near and far-field regimes, we can also measure the polarization efficiency of the telescope as the fraction of integrated power from the co-polarization with respect to the total power, i.e., integrated co-polarization power plus integrated cross-polarization power, given by

$$n_{pol} = \frac{I-Q}{I+Q} \qquad \text{(Eq. 3.1)}$$

This allows us to analyze how the power from a polarized source is received by the telescope. Moreover, by applying the previous relation to each data point in the co-polarization and cross-polarization patterns, we can obtain a per-pixel map of the polarization efficiency of the beam and allows us to determine how this polarized power is distributed within the beam.

3.2. Results of the 150 GHz optics electromagnetic simulations

The simulations show that the CLASS 150 GHz optics generate a gain of 51.65 dB and a beamwidth of 0.362° or 21.7 arcmin. The cross-polarization peak sits at 1.69 dB, roughly 50 dB below the co-polarization peak. The co-polarization solid angle is measured from the data at 48.3 µsr at a 7.5° radius, while the cross-polarization solid angle is 0.001 µsr. The simulations in Figure 3-5 were carried out in the far field regime, in which the software evaluates the rays of the telescope at distance equivalent to infinity.

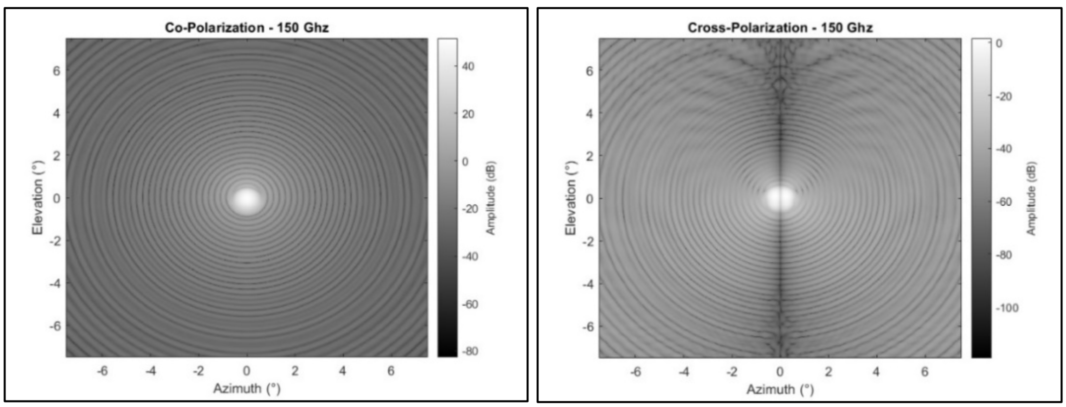

Figure 3-5. Results of the simulation of the CLASS 150 GHz optics.
The resulting cross-polarization shows a vertically oriented pattern in the center due to the chosen orientation of the detectors during this simulation. The actual orientation should reflect a 45°/-45° inclined pattern that matches the paired detectors' physical orientations in the focal plane. This discrepancy should not generate any significant variations in the studied properties of the optics.

The beam and solid angles of the CLASS telescope have been measured experimentally at 22.68 arcmin and 51 µsr (Dahal, et al., 2021). The discrepancies of the simulation from the measured values are expected and acceptable, given that the simulations are carried out in an environment where non-ideal effects are ignored.

The simulations of the near and far-field regimes are shown in Table 1, in which we can see that the telescope starts behaving as in the far field for distances of 200 meters and greater. This shows good agreement with the theoretical calculations of ~193 meters, shown earlier. At 200 meters, the simulated near field beamwidth matches the far field beamwidth with 2% error and the solid angle is only 3% larger than its far field counterpart. At 500 meters, both parameters differ by 1% or less from the far field case. The GRASP software uses different methods for calculating the near and far field patterns, which can explain the observed difference of less than 1%. Nevertheless, the results show that a distance of 500 meters is more than appropriate to perform the calibration procedures with the drone-based calibrator for the CLASS project, as it is well within the theoretical far field and the simulated one.

Table 1. Summary of simulation results for the near and far field regime of the CLASS 150 GHz optics

Distance (m)	Co-Pol. Solid Angle [4] (μsr)	Cross-Pol. Solid angle (μsr)	Beamwidth[4] (°)	Polarization efficiency (%)
25	88.475 (25%)	0.001	0.473 (31%)	99.997
50	59.344 (23%)	0.001	0.404 (12%)	99.997
100	52.049 (8%)	0.001	0.374 (4%)	99.997
200	49.784 (3%)	0.001	0.368 (2%)	99.997
300	49.204 (2%)	0.001	0.365 (1%)	99.997
500	48.807 (1%)	0.001	0.362 (<1%)	99.997
Far Field	48.325	0.001	0.362	99.997

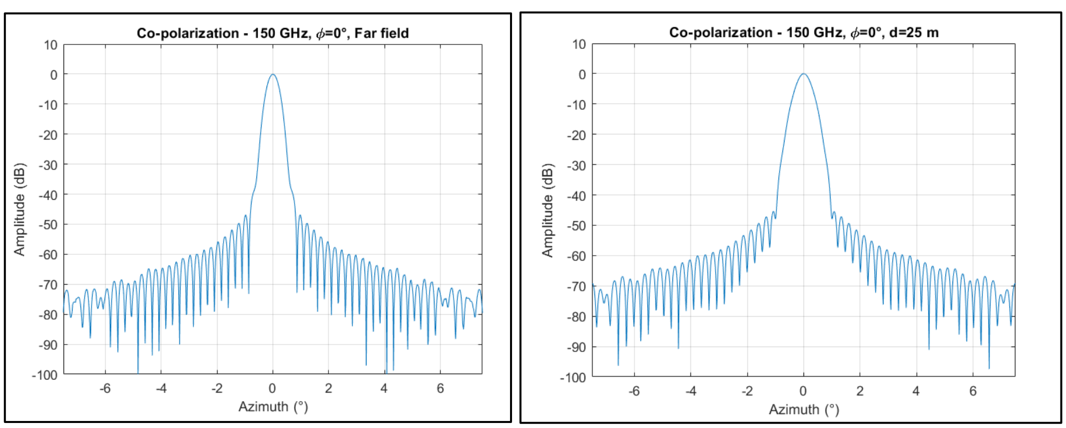

Figure 3-6. Cut of the co-polarization radiation pattern for the far field (left) and near field at 25 meters (right). The radiation patterns vary slightly, especially the main lobe, which thickens and, consequently, increases the width of main beam. Nevertheless, other features, such as sidelobe shapes and amplitudes remain relatively constant.

[4] The relative difference between the near field compared to the far field are shown in parenthesis

From the radiation pattern of the CLASS telescope, considering the nominal accuracy of the RTK GNSS positioning system of the drone (horizontal/vertical: 1 cm + 1 ppm / 2 cm + 1 ppm) at a distance of 500 meters, the motion of the drone would generate an angular uncertainty of ~0.002°. This value would result in a power uncertainty at the telescope's detectors no higher than ±0.065 dB (1.5%) with the drone hovering in place at the center of the beam.

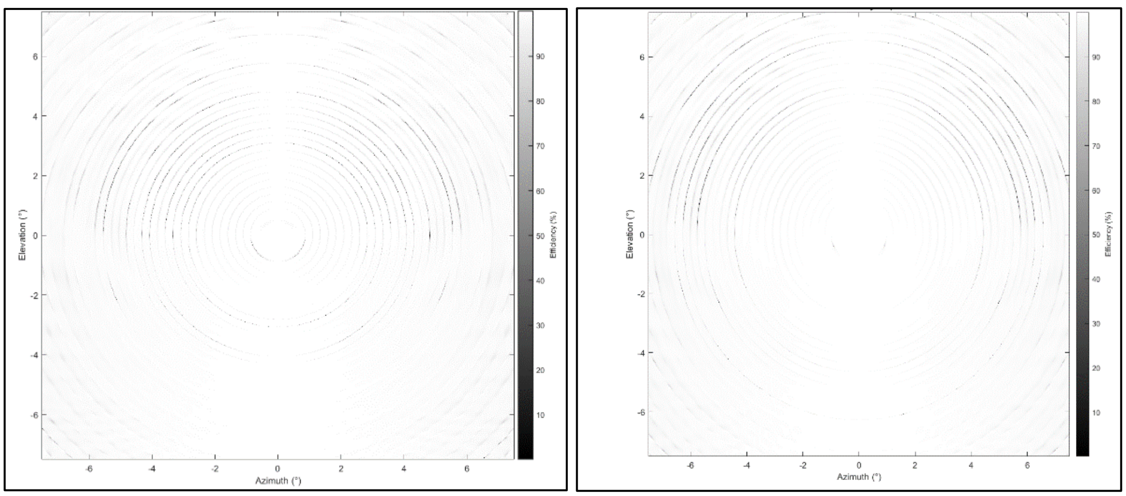

Figure 3-7. Polarization efficiency map for the far field (left) and near field at 25 meters (right). Darker is less efficient.
Despite apparent differences, especially in central and outlying areas corresponding to sidelobe dips, the total polarization efficiency remains constant at the different near field distances.

The overall result of the polarization efficiency map shows a symmetric pattern, shown in Figure 3-7. The near field polarization efficiency map shows a nearly identical result except for the sidelobe-produced dips at a ~0.8° radius being absent. On a deeper inspection of the far field map, we can measure that the polarization efficiency within up to a 0.8° radius varies from 100% to 99.99% at the edge; for larger radii, the polarization efficiency remains at ~99.9% except at the sidelobe dips. This result ensures that despite the positioning accuracy of the drone, the polarization signal can be recovered with near perfect efficiency when flying at 500 meters.

4. TECHNICAL CONSIDERATIONS OF THE POLARIZED RF SOURCE

4.1. The UAV-based calibrator of the Astro-Engineering Center

Given the necessity of better CMB telescope calibration methods and taking advantage of the advancement of UAV technology, the Astro-Engineering Center (AIUC) of Pontificia Universidad Católica de Chile (PUC) has proposed a UAV-based calibrator that can cover the 130 - 160GHz frequency range. This frequency span should allow for the characterization of the 150 GHz camera of the CLASS telescope, among other polarization sensitive CMB experiments with a similar frequency range.

There are several technical constraints involved in the design and implementation of a UAV-based calibrator for CMB experiments. One of the most important challenges is determining the position and angle in the sky of a highly linearly polarized reference signal, while maintaining power and frequency stability.

The goal of the project is to mount a linearly polarized RF source onboard of a professional, commercially available drone and fly it at the far-field of small aperture CMB experiments to serve as a polarization calibrator with polarization angle accuracy equal to or better than $\pm 0.1°$. The calibrator will make use of high-accuracy GPS positioning and photogrammetry to determine the polarization angle of a linearly polarized signal.

The RF source is comprised of a Phase-Locked-Loop (PLL) based polarized RF emitter system and a photogrammetry-based metrology system. During laboratory calibrations, the metrology system will allow us to obtain the polarization angle of the source with respect to the mechanical frame with the use of a laser emitter; during flight, it will be used to record high-definition video of landmarks (targets) placed in the surrounding area of the telescope to perform photogrammetry at a later stage in data processing. This will allow for the determination of the RF source's attitude with respect to the telescope and, thus, obtain the polarization angle as observed by the telescope.

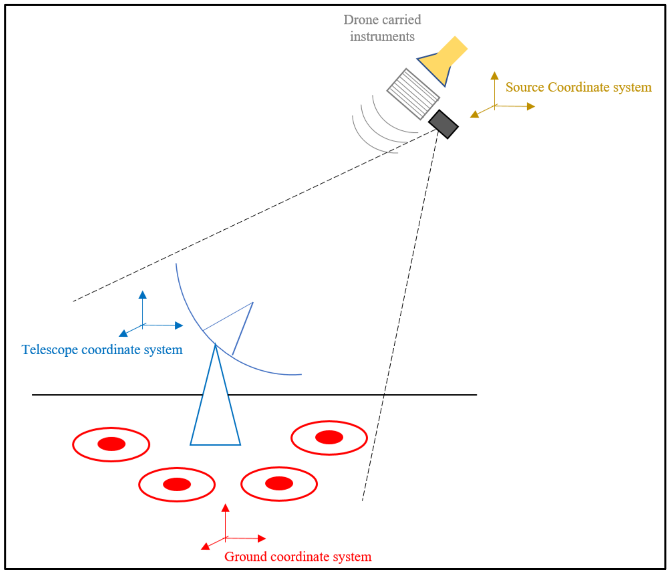

Figure 4-1. Sketch of the proposed method for a UAV-based calibrator.
The setup considers the RF source/drone GPS coordinates (yellow) that will be referenced to the ground coordinate system's landmarks (red) via GPS positioning. Geo-referenced landmarks allow for the transformation of their coordinate system to the telescope's coordinates (blue). The dotted lines represent the metrology camera's FOV from which the attitude of the source —and, thus, the polarization angle relative to the telescope and the sky— can be determined with photogrammetry.

4.2. Description of the UAV-based telescope calibrator

The UAV-based calibrator considers the use of a professional-grade UAV and gimbal, the photogrammetry-based metrology system, and the polarized RF emitter system. The differential GPS receiver system of the UAV ensures that the position of the emitter is known with accuracy of the order of centimeters, while the gimbal absorbs vibrations induced by the propellers, gusts of wind or other effects that can affect the payload. The metrology system, composed of the action camera and the laser emitter, is also carried within the mechanical frame mounted in the gimbal.

A more detailed description of the systems of the UAV-based calibrator as well as the roles of each of their components is listed below.

- <u>DJI Matrice Pro 600 UAV:</u>

A professional grade, heavy lift UAV, equipped with Real Time Kinematic (RTK) GPS assisted navigation, with nominal accuracy of 1 cm + 1 ppm and 2 cm + 1 ppm for vertical and horizontal positioning, respectively. At ground level, its hovering time with a 6 kg payload is listed as 16 minutes. The Matrice Pro 600 is compatible with several third-party cameras and gimbals via a standard dovetail mechanical mount. It can be controlled via a wireless link in the 2.4 GHz or 5.8 GHz frequency bands (DJI, 2021).

- DJI Ronin MX gimbal:

An active stabilization frame that can communicate with DJI hardware. It includes several sensors such as motor encoders, temperature sensors and gyroscopes that ensure the attitude of the payload remains within the user's specification. It can be controlled by a Bluetooth wireless connection, through the 2.4 GHz remote controller wireless link, or from the UAV's wireless link. The gimbal includes two 12 V regulated power outputs (PTAP connector) that can supply up to 3 A in total (DJI, 2021) and serve as the primary energy source of the RF source.

- Photogrammetry-based metrology system:

During flight, the metrology system will obtain the attitude of the RF source with respect to the telescope through georeferenced landmarks and photogrammetry performed on 4K, 30 frames-per-second videos recorded with an ultra-compact Sony RX0-II action camera. During laboratory characterization, the metrology system will be used to obtain the relative angle between the metrology camera and the wire grid polarizer of the RF source by analyzing the images of the projected diffraction pattern obtained with a 5-mW laser permanently mounted in the frame and shun at the polarizer. From those two processes, it will be possible to obtain the absolute polarization angle of the RF source throughout the calibration missions.

- PLL-based polarized RF emitter system:

The RF emitter systems generates a pure, polarized RF tone in the 130 to 160 GHz frequency range. The RF source is expected to be highly stable both in power and frequency, while its power output is expected to be within the linear-regime power limits of the CLASS telescope detectors.

The current implementation of the RF source consists of a Raspberry Pi 3B microcontroller, which communicates with an ADF5355 PLL board to generate a signal between ~10.8 GHz and ~13.3 GHz. The signal is then passed through a handcrafted, resonant cavity RF filter tuned to remove any harmonics outside the frequency range of interest. A fixed 10 dB attenuator followed by a high-flatness 24 dB RF amplifier modify the signal amplitude to be within the typical limits of an Amplifier/Multiplier Chain (AMC) RF Multiplier, which multiplies the input frequency by a factor of 12. The multiplier can be on-off modulated and attenuated precisely with digital and analog signals, respectively, input into the corresponding pins. The output of the amplifier is coupled to the air via an open-ended waveguide, handcrafted from a dual-flange waveguide adapter as part of this work. The output signal then goes through a wire-grid polarizer that ensures and enhances the polarization angle of the signal and allows for the determination of the absolute polarization angle of the RF source through the metrology system.

- Supply board / attenuation controller:

  A circuit board that handles the voltage conversion to supply the RF electronics with power. It contains additional components that generate the voltage reference for the attenuation pin of the multiplier and a current driver for the optional modulation pin in the multiplier. As part of this work, the original power supply electronics were redesigned to allow for the use of the gimbal's 12 V P-TAP output as power supply, with efficient switching regulators that supply the voltage required by each component.

The interaction of the each of the system components is summarized in Figure 4-2, which considers the inclusion of the support structure designed to house the RF source components.

Several tests using UAV-carried equipment have been performed at ~5200 meters above sea level (m.a.s.l.) at the site of the CLASS experiment (see Dünner, Fluxá, Best, & Carrero, 2020). In these test flights it was determined that the DJI Matrice 600 Pro can achieve an altitude up to 500 meters above the ground (legal roof for commercial UAVs) with high-altitude propellers while carrying a payload of up to 4 kilograms during 10-minute missions, which can be extended by using multiple sets of batteries. Additionally, these tests allowed for the determination of the equivalent temperature emission of the aircraft as seen by the CLASS telescope, which was roughly modeled by a 290 Kelvin blackbody with a cross-section diameter of 24 centimeters. With this parameter, in order to maintain the CLASS telescope detectors in the linear regime, the UAV must fly at no less than ~230 meters from the telescope, as shown in Table 2.

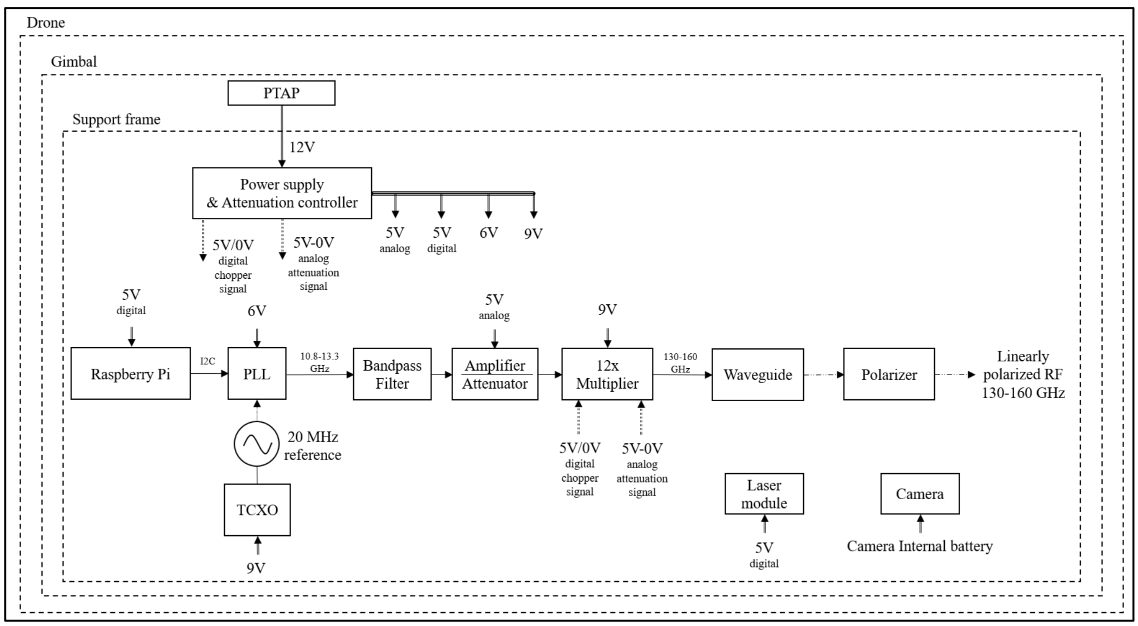

Figure 4-2. Sketch of the components of AIUC's UAV-based calibrator.

The maximum transmitted power limits consider the detectors of the CLASS telescope saturating at 2 pico-Watts of input power. The minimum transmitted power is estimated by taking into consideration a desired signal-to-noise (SNR) ratio of 5 per detector sample, from which the distance versus power curves can be obtained, shown in Figure 4-3.

Other preliminary tests were also carried out using a Gunn oscillator operating at a frequency of 145 GHz coupled to a pyramidal horn and a mechanical chopper wheel. With this setup, it was possible to measure one of the far sidelobes of the ACT telescope at 150 GHz (Dünner, Fluxá, Best, Carrero, & Boettger, 2021). The design of the RF source was then upgraded to the final system described earlier, the programmable, PLL-based signal generator. This final setup constitutes the base framework for the objectives of this thesis.

Table 2. UAV emission at 150 GHz as a percentage of maximum detector power in the linear regime. The distances at which detectors operate in the nonlinear regime are marked in red.

Distance	Detector Power
100	513%
200	128%
226	100%
300	57%
400	32%
500	20%
600	14%

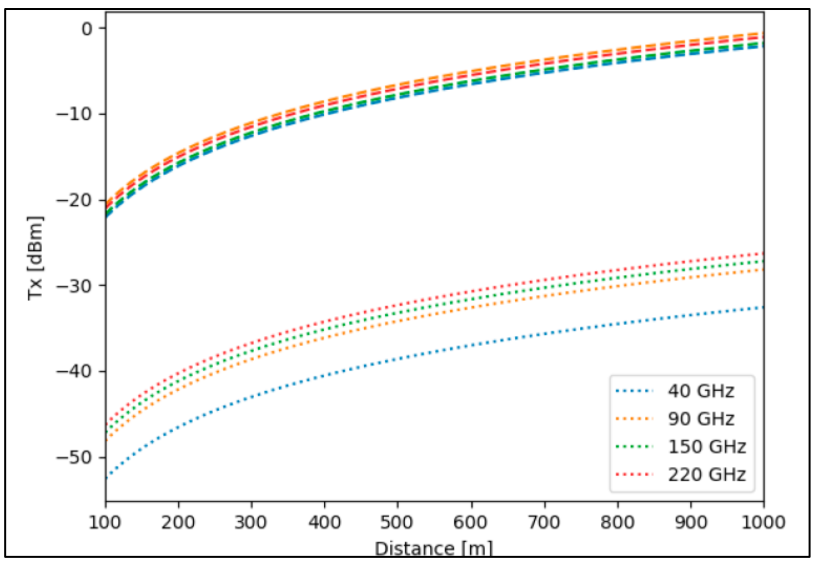

Figure 4-3. Maximum (dashed) transmitted power to avoid detector saturation and minimum (dotted) transmitted power for SNR=5 per sample at different frequencies.
From 'Millimeter-wave polarization angle calibration using UAV-based sources', Dünner, Fluxá, Best and Carrero, 2020

Finally, the UAV-based calibrator's technical requirements, determined from a combination of data from preliminary test flights mentioned earlier and the calibrator's scientific objectives, are listed in Table 3.

Table 3. Technical specifications of the UAV-based calibrator

<table>
<tr><th>Parameter</th><th>Value</th><th>Observations</th></tr>
<tr><td>Maximum altitude of operation:</td><td>> 5700 m.a.s.l.</td><td>Dependent on the altitude of the telescope to be calibrated. The listed specification implies a 5200 m.a.s.l. base altitude and flight at 500 meters.</td></tr>
<tr><td>Positioning accuracy:</td><td>$\sqrt{\Delta X^2 + \Delta Y^2 + \Delta Z^2}$
$< 32\ cm$</td><td>Corresponds to the required accuracy of the drone's RTK-GPS so that the induced angular variation is no higher than 0.1 $\mathrm{FWHM}_{150\mathrm{GHz}}$ of the CLASS telescope while flying at a distance greater or equal to 500 meters. ($FWHM_{150GHz}$=0.36°)</td></tr>
<tr><td>Metrology system absolute angular accuracy:</td><td><table><tr><td>Roll:</td><td>$\pm 0.1°$</td></tr><tr><td>Pitch:</td><td>$\pm 3.0°$</td></tr><tr><td>Yaw:</td><td>$\pm 3.0°$</td></tr></table></td><td>Refers to the measured orientation of the source with respect to the telescope. Metrology X, Y and Z accuracies are not required, as these are determined from the RTK-GPS.

*Roll: rotation around the line-of-sight axis (boresight) of the telescope/calibrator, usually associated with the Z axis (orthogonal to the XY plane) and the absolute polarization angle of the source. The Roll parameter must include photogrammetry, grid alignment uncertainties, mechanical effects, among others.

*Pitch/Yaw: Usually defined as a rotation around the X/Y axis, which we define as parallel/perpendicular to the plane of the drone's propeller arms. Listed values correspond to the approximate angle at which a 1% variation in power is measured in an open-ended waveguide feed radiation pattern.</td></tr>
<tr><td>Power stability:</td><td>10%, within 0.24-second intervals</td><td>Power stability should be assured within the scale of time it takes the telescope to scan an angle equivalent to one FHWM. Time scale was calculated from the CLASS experiment specifications: maximum scan speed of ~1.5°/s and $FHWM_{150GHz} = 0.36°$.</td></tr>
<tr><td>Frequency stability:</td><td>1% of bandwidth at the frequency band</td><td>CMB telescopes typically have large bandwidths, so a small margin for variation in frequency is defined as its upper limit. Frequency-shift-induced power variations should also remain negligible.</td></tr>
<tr><td>Metrology system refresh rate:</td><td>> 8 Hz</td><td>Ensures that at least 2 metrology measurements are carried out in the time it takes the CLASS telescope to scan an angle equivalent to one $FHWM_{150GHz}$.</td></tr>
<tr><td>Payload:</td><td>≥ 4 kg</td><td>Considers 2 kg for the gimbal stabilizer and 2 kg for the RF source.</td></tr>
<tr><td>Flight time:</td><td>≥ 10 minutes</td><td>Based on preliminary test flights, ensures a ~7-minute calibration mission plus ~3 minutes for ascent and descent.</td></tr>
</table>

5. INTEGRATION AND CHARACTERIZATION OF THE POLARIZED RF SOURCE

The UAV-based calibrator of the Astro-Engineering Center was designed considering the two systems that compose the RF source: the RF emitter system and the metrology system. As stated earlier, the main objectives of this thesis work are to integrate and test the RF hardware, design a mechanical structure that can be carried by the aircraft and incorporate the RF hardware, and finally characterize the integrated system. To achieve these objectives, the RF source was characterized and tested through the following experiments:

- Power and frequency stability measurements: attempts to measure and characterize dispersions produced by the intrinsic performance of the electronic components that compose the RF system.

- Band power characterization and absolute output power determination: the objective is to establish the power versus frequency response of the RF source and determine the effective emitted power.

- Polarization angle measurements: intended to measure and assess the quality of the polarization angle of the RF source.

- Relative polarization angle measurements: aims at determining the spatial homogeneity of the polarization angle of the RF source.

- Radiation pattern measurement: the objective is to measure and characterize the power emitted by the source as a function of its orientation.

- Polarizer grid relative angle measurement: the goal is to design a reliable method for obtaining the relative angle between the polarizer and metrology camera and then perform polarizer relative angle measurements with the devised method.

In addition, the mechanical frame design was evaluated for thermal expansion to assess potential variations in the polarizer relative angle during flight at CMB observatories high altitude sites.

Finally, a test flight of the RF source integrated into the gimbal and UAV was carried out to verify is overall performance.

5.1. Mechanical frame implementation

5.1.1. Mechanical frame design

The integration of the RF emitter and other components into the aircraft required the fabrication of a support structure capable of being mounted in the gimbal. As determined by the preliminary tests, a payload of 4 kg allowed 10-minute-long missions at CMB experiment sites. Thus, the first constraint derives from the weight of the Ronin MX gimbal declared as 2.15 kg (DJI, Ronin MX Specifications, 2021), which leaves a margin of roughly 1.85 kg for the mechanical support structure and components of the RF and photogrammetry systems.

The second constraint is the usable volume of the Ronin MX gimbal. Specifications list the maximum height at 130 millimeters, maximum width at 160 millimeters and maximum depth from the center of gravity at 120 millimeters. Figure 5-1 shows the layout of the Ronin MX gimbal the maximum allowable sizes on each axis of a reference coordinate system.

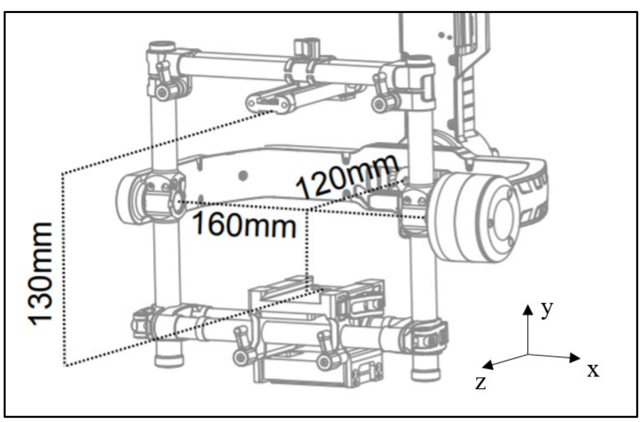

Figure 5-1. Dimensions of the Ronin MX usable volume.
Modified from 'Ronin MX User Manual V1.2', by DJI, retrieved from
https://dl.djicdn.com/downloads/ronin-mx/en/Ronin-MX_User_Manual_V1.2_en_20160711.pdf

Considering most the calibrator's components were already defined prior to this work, the allowable weight for the support frame was subject to the remainder of the 1.85 kg once the rest of components were accounted for. The weight of the components was obtained from technical documentation or by weighting the elements where a reference value was not available, summarized in Table 4.

Table 4. Weight of the UAV-based calibrator's components

Component	Weight
Wire-grid Polarizer	280 g
Camera	117 g
Raspberry Pi	50 g
PLL board	50 g
Power supply board	50 g
Multiplier	45 g
Filter	35 g
Amplifier	25 g
Waveguide	15 g
TCXO	10 g
Laser module	8g
Mounting hardware	75 g
Others	50 g
Total:	810 g

With this information, it was estimated that the weight of the support frame could not exceed ~1 kg in order to maintain the same flight autonomy as in the preliminary tests.

Other important criteria for the design were the requirement of high rigidity and mechanical robustness of the frame. This was a constraint set by the photogrammetry system, which requires that the alignment between the polarizing grid and the camera stays as constant as possible during and after laboratory characterization of their relative angle, but also during flight. This requirement calls for a rigid material and the fabrication should favor a frame machined from a single block of material; the latter condition aims at reducing the chance of structural elements coming loose from on-flight vibrations. Ideal materials would be thermoplastics such as Acrylonitrile Butadiene

Styrene (ABS) or Polylactic Acid (PLA), which can be used in the 3D printer available at AIUC. Among these alternatives, PLA has shown better properties such as low deformation, improved printing bed adherence and widespread availability. Should the need for superior mechanical properties be required later, carbon fiber reinforced filaments have shown improved results (Heidari-Rarani, Rafiee-Afarani, & Zahedi, 2019) and could represent an excellent alternative to PLA without dismissing 3D printing altogether.

Several designs for a single-block aluminum support frame were evaluated in SolidWorks for weight, which yielded results of the order of 1 kg. The high weight, in addition to the complexity and cost of machining aluminum to allow for several support structures, further cemented the decision of fabricating the structure in a 3D printer with PLA plastic. Moreover, the support structure will not be subject to heavy mechanical stress and will act as a platform to accommodate and carry the instruments, the only caveat being that thermal deformations at temperatures expected at CMB sites should not affect the alignment of the camera and polarizer.

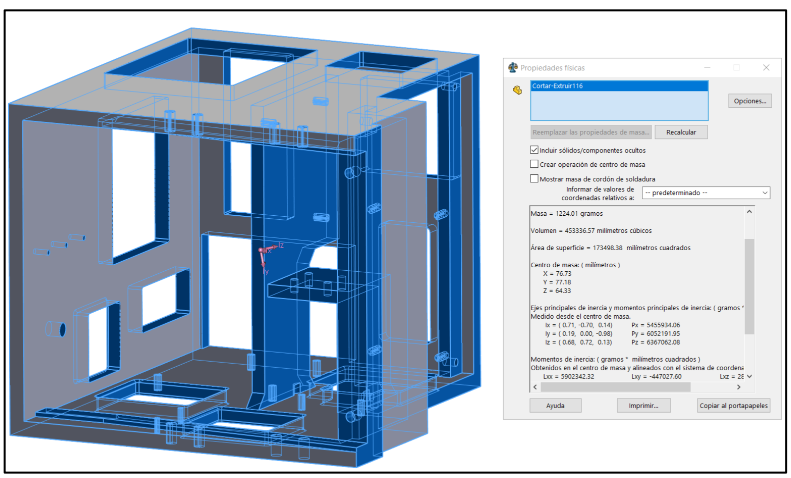

Figure 5-2. Early study of an aluminum single-block support frame with 5-millimeter-thick walls, evaluated for weight in SolidWorks.

To accurately design the support frame taking into consideration ease of assembly and access to component ports and buttons, the 3D models of each element were obtained when available or created in SolidWorks. Using these 3D elements, the design of the support frame was iteratively improved using different configurations.

Figure 5-3. Some of the UAV-based calibrator's elements (left) and their corresponding 3D model in SolidWorks (right).

The design of the support frame considered the interconnection between parts and access to terminals and ports, as well as ease of assembly. The criteria considered for the placement of the elements are listed below:

- The wire-grid polarizer is required to be the final element facing the telescope. The polarizer should be firmly secured to the support structure. The plane of polarizer should be angled at no less than ~5° with respect to the multiplier's output plane to minimize reflections.
- The camera's field of view should be mostly unblocked to be used for photogrammetry during flights, which requires that the camera be also in the front of the frame, but not blocked by the wire grid. The camera should be firmly secured to the frame. The power and record buttons should be accessible by hand and the micro-HDMI port should accessible when the camera is mounted in the frame, should video feed access be required on-site.
- The multiplier and waveguide output must be centered relative to the wire grid, which ensures that the RF signal goes mostly unaltered through the polarizer and

reflections on the polarizer frame are minimized.

- The PLL, TCXO, RF filter, amplifier and multiplier input must form a path that allows for easy interconnection of the elements, following the transmission chain. The number of additional connectors or adapters between cables should be minimized to reduce vibration-induced problems such as loosening of connectors during flight.
- The Raspberry Pi's ports and connectors should be easily accessible, should debugging on-site be required. Connection between the raspberry I/O pins and the PLL I/O pins must be possible.
- The support frame must include a bottom dovetail mount compatible with the gimbals locking mechanism.
- A laser emitter must be placed within view of the polarizing grid and must be aligned to it.
- The center of mass of the frame and components must lie as close as possible to the geometrical center of the structure to minimize the required balance corrections when mounted on the gimbal.
- Access to all mounting hardware, such as bolts and screws, should be possible with relative ease.

The final design of the support frame consists of a single-block structure that can contain all the elements of the UAV-based calibrator and fulfils all the above criteria, shown in Figure 5-4. While the side of the of the frame is open, a side lid was added as protection to the components. The lid does not fulfil any structural function and thus the objective of a single-block structure is accomplished. The final dimensions of the support frame are 130 mm x 148 mm x 160 mm (Height x Width x Depth), with 5 mm thick walls. The lid dimensions are 118 mm x 82.7 mm x 5 mm. The weight of the frame and lid correspond to 250 g and 26 g, respectively. The center of mass of the frame, obtained from SolidWorks corresponds to 56 mm, 74 mm, 61 mm for the X, Y and Z coordinates, respectively. This implies that the frame's weight is shifted slightly towards the front and bottom.

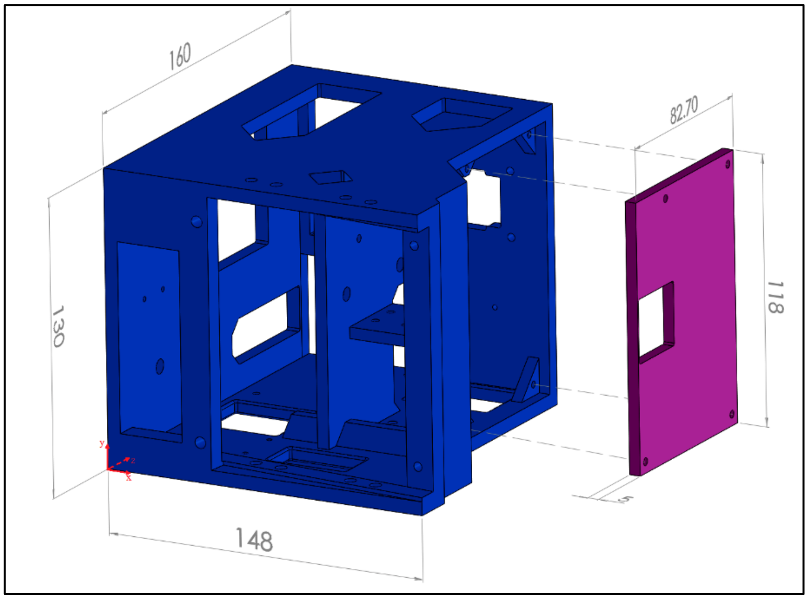

Figure 5-4. Final dimensions of the support frame and side cover.
The back section of the frame is narrower than the front to allow for more leeway during the balancing process when mounted in the gimbal

The distribution of the elements is outlined in the following series of figures. As stated earlier, the camera and polarizer are both located in the front of the frame (see Figure 5-5), with the multiplier centered within the wire grid's open section. The grid itself is angled by 5° with respect to the plane of the multiplier output.

The grid is supported by 5-millimeter bolts that secure it firmly to the top and bottom of the frame. Structural integrity in this section is reinforced by the vertical beam that links the top and bottom walls of the frame and by as the corners of the cubic structure, where the rest of the frame's faces intersect. If additional restraint of the wire grid is required, 4 holes in the frame allow for the use of additional bolts to lock rotation around axial direction of the main bolts.

The camera is supported by the side with a ¼-inch standard tripod-mount bolt that fits in the camera and secures it firmly against the frame's wall; moreover, an additional supporting structure, shown in purple in Figure 5-6, acts as a cage and was added to prevent rotations around the axis of the tripod bolt.

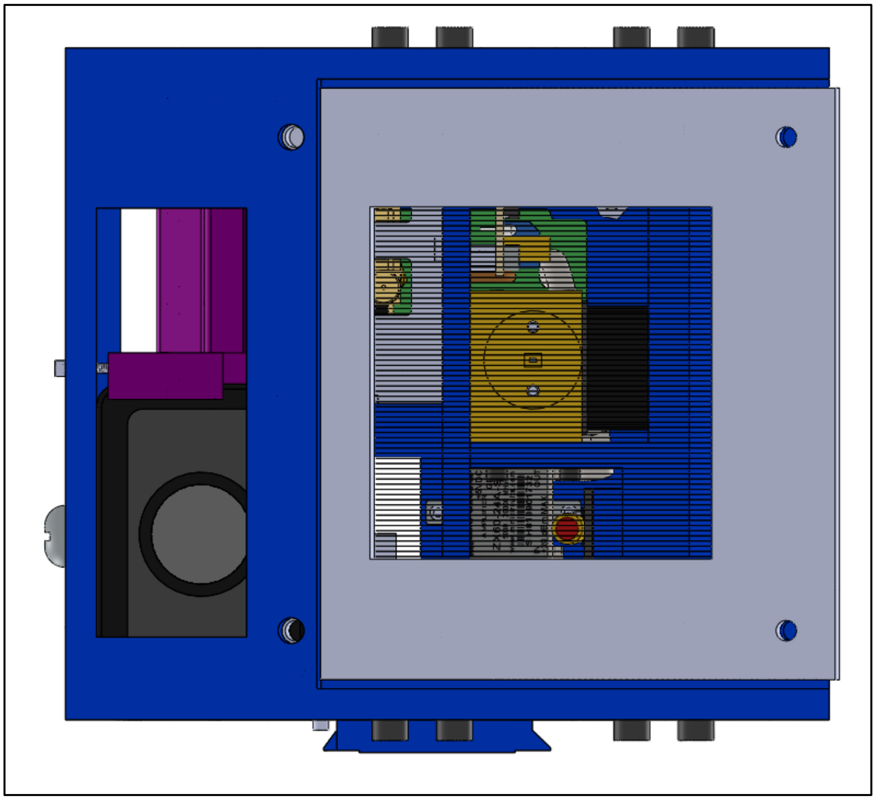

Figure 5-5. Front section of the support frame assembly in SolidWorks shows the camera, polarizer, multiplier and laser module.

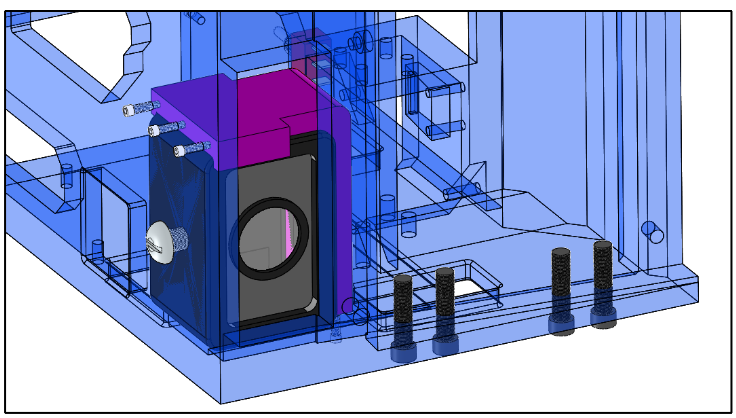

Figure 5-6. Close up view of the camera mount and support structure.
The support structure was designed slightly smaller than the camera itself to ensure the five 2-millemeter bolts (4 visible) constrain movement of the camera. The black bolts correspond to the bottom section mounting hardware of the polarizer.

Next to the camera, an open section in the frame of 20 mm x 37 mm allows for manipulation of the camera buttons, shown in Figure 5-7, and should be accessible from the bottom of the frame to engage video recording prior to or after its placement in the gimbal.

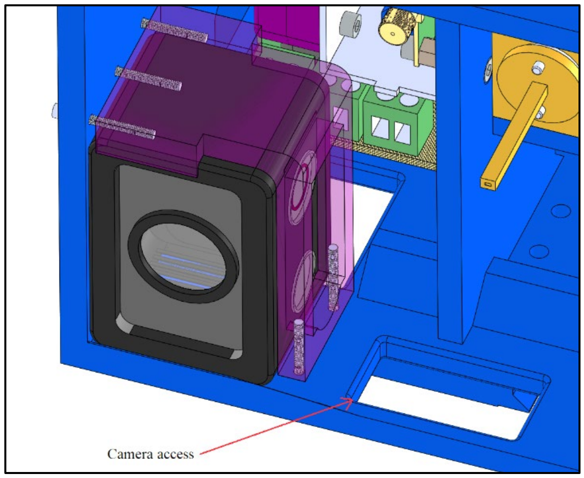

Figure 5-7. Section view of the support frame highlighting the camera access. The camera buttons can be accessed from the bottom. The camera's support structure, shown as a transparent wire frame, also allows access to the camera buttons.

In addition, the camera's 4K, 1.778 aspect ratio video recording FOV of 84° x 47° is mostly unaltered by grid polarizer or by the supporting structures seen on the front of the frame, resulting in an effective symmetrical FOV of 84° x 44°.

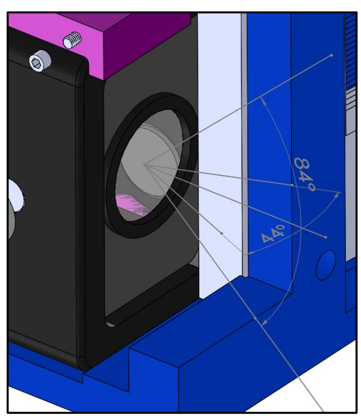

Figure 5-8. Section view of the frame showcasing the camera's field of view.

The multiplier was placed at the vertical center point of the polarizer, held by 4 bolts to a flat surface, structurally supported by a vertical beam that links the top and bottom faces of the frame. The PLL board, encased in a supporting aluminum profile, was placed on the opposite face of the beam, with RF output connectors facing the back of the frame and external reference connectors facing the front of the frame. The TCXO is then placed on the support beam, on top of the multiplier, which allows easy access to the external reference connector of the PLL. The laser module is placed just below the multiplier and aligned to the grid's 5° angle. The Raspberry Pi, encased in a 3D printed enclosure, is mounted with 4 bolts (two on the side and two on the top face) on the PLL's aluminum profile. The power supply and attenuation board is located on the floor of the frame, with its input terminal at the back and its output terminals oriented towards the corresponding components. A horizontal support beam is located on the floor of the frame to reinforce the rail mount for the gimbal and prevent deformations. Figure 5-9 illustrates the distribution of the components from the front of the frame.

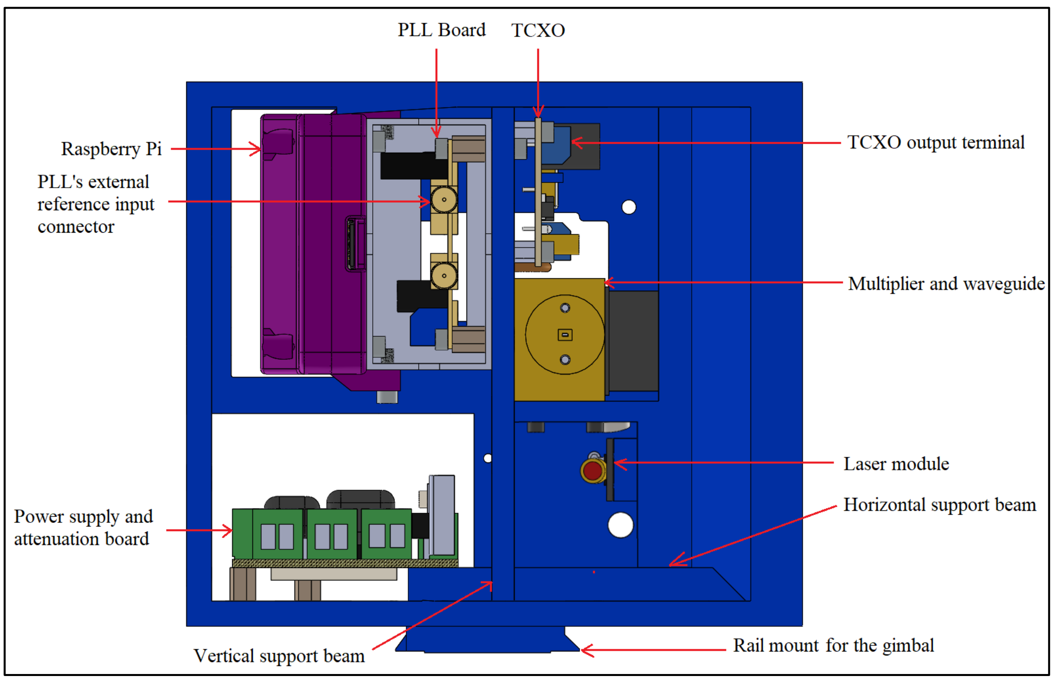

Figure 5-9. Section view of the frame, showing the elements located on the mid-section. Some of the mounting holes for the PLL support bolts are recessed to allow the multiplier to be flush against the vertical beam

On the rear section of the frame, the bandpass filter and RF amplifier are mounted in the internal and external faces of the frame, respectively. The bandpass filter's cables are fixed in length and the PLL cannot be moved forward due to being limited by the position of the camera, so the filter was mounted outside of the frame to accommodate for these conditions without additional adapters. The amplifier was mounted with the input facing down, so that the output is then closer to the multiplier; this prompts the use of only one additional adapter and cable to connect the output of the filter to the input of the amplifier (see Figure 5-10 for details).

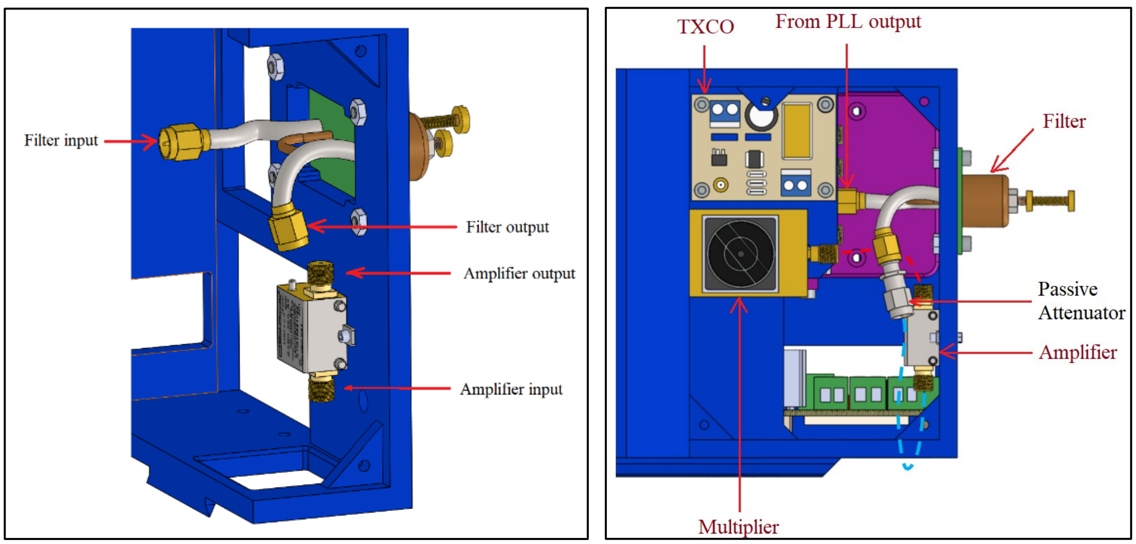

Figure 5-10. Rear section views of the support frame elements.
Left: placement of the filter and amplifier. Right: Connection of the PLL, filter and passive attenuator, amplifier, and multiplier. The dashed light blue line shows the expected path of the cable from the output of the filter to the input of the amplifier; the dashed red line follows the output of the amplifier to the input of the multiplier.

Other relevant features correspond to several open sections aimed at improving handling and assembly. These open sections are located near the top face on the rear of the frame —to improve manipulation of cables and connectors—; bottom face near the front of the frame —to access the camera's connector panel—; top face —an open section to check for alignment of the waveguide with the rotary actuator during characterization procedures—; rear face, upper section of the frame —to access the peripheral and network connectors of the Raspberry Pi—; and rear face, bottom section of the frame —to mount and improve access to the power supply board—. These additions and other miscellaneous information of the frame design are shown in Figure 5-11 , Figure 5-12 and Figure 5-13.

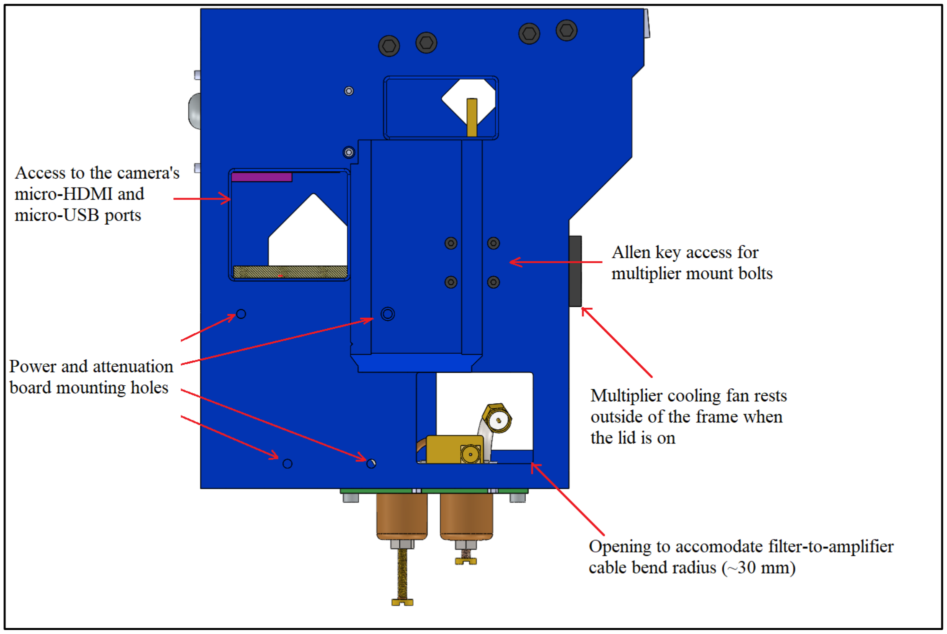

Figure 5-11. Miscellaneous details on the bottom face of the frame.
Some of the mounting holes for the bolts are recessed to accommodate for other elements.

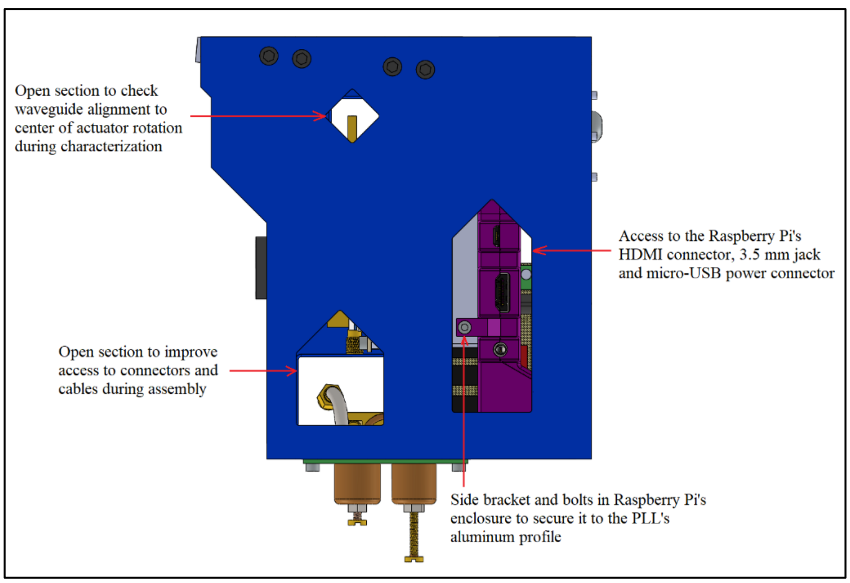

Figure 5-12. Miscellaneous details of the top face of the frame.

With each component's final placement defined, it is possible to make a rough estimation of the center of mass with coordinates from the SolidWorks 3D model. For this estimation, it will be assumed that the weight in each component is evenly distributed and, thus, each element's center of mass can be calculated from the geometric center and mass.

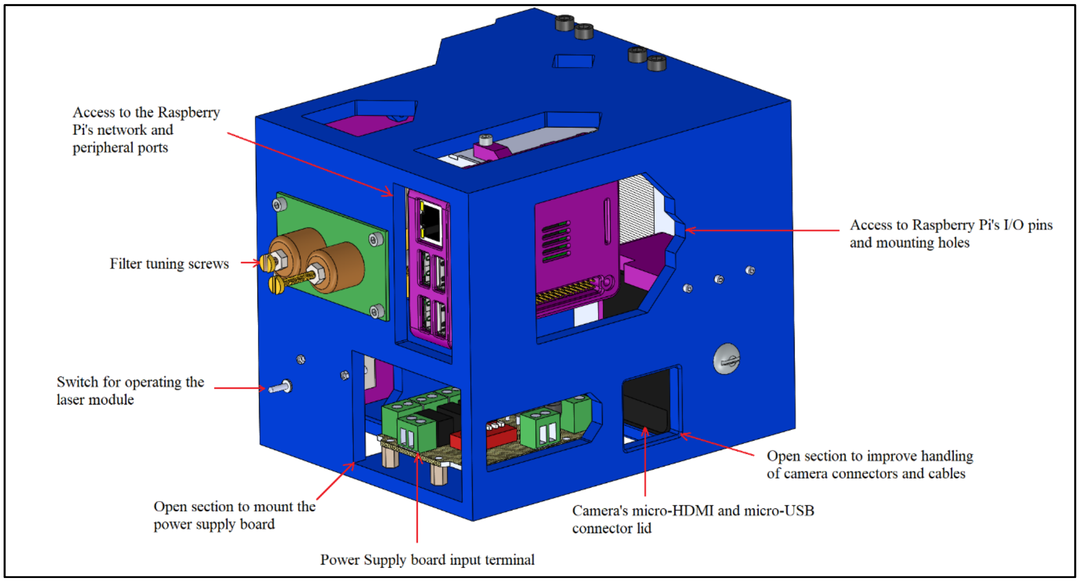

Figure 5-13. Additional information of the frame design.

In addition, the weight of mounting hardware, cables, and connectors will not be considered or, equivalently, it can be assumed that their weight is evenly distributed in the frame. This will allow for a first approximation of the balancing process that must be carried out when mounting the frame into the gimbal.

Table 5. Approximate centroids of each element and resulting center of mass

Element	**X Centroid (mm)**	**Y Centroid (mm)**	**Z Centroid (mm)**	**Mass (g)**
Grid	92	65	17	280
Frame	56	74	61	250
Camera	26	35	38	117
PLL (w/case)	66	92	87	100
R-Pi (w/case)	28	95	110	84
Power board	38	22	118	50
Multiplier	94	70	88	45
Filter	78	86	160	35
Amplifier	84	40	150	25
Lid	120	68	120	26
Wave guide	89	71	56	15
TXCO	88	104	95	10
Camera cage	37	57	37	10
Laser	97	37	81	8
Result:	66 (65)	67 (74)	64 (80)	1055

The estimated center of mass is shown in Table 5, with the geometrical center of the frame shown in parenthesis. From this result we can conclude that the weight will be shifted slightly towards the bottom front section of the frame, which translates into balancing adjustments no higher than 16 millimeters when mounted in the gimbal. Considering the simplifications and assumptions taken for the calculations, the final adjustments might vary slightly.

Finally, we can perform thermal expansion simulations at the expected temperatures that the support frame will be subject to when performing calibrations at high altitude CMB experiment sites. Taking CLASS project's location at mount Toco in San Pedro de Atacama as a reference, we can obtain the minimum temperatures at an altitude of ~5600 meters. This corresponds to flight with the source at ~500 meters from the CLASS telescope (at an angle 45°). From the Chilean Department of Energy's Solar Explorer, an online platform with comprehensive records of weather conditions and weather prediction models in Chilean territory, we can obtain the average monthly temperatures per hour of the day as shown in Figure 5-14

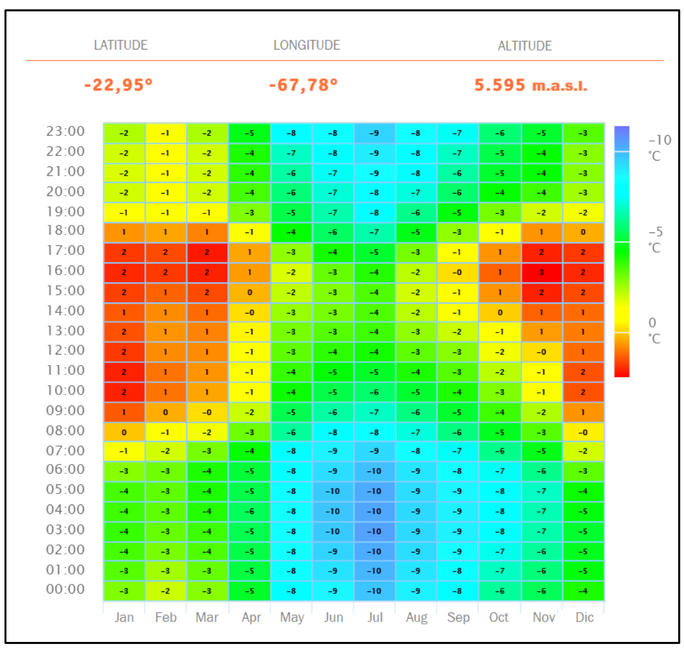

Figure 5-14. Summary of average, per-hour monthly temperatures at Mount Toco. Modified from 'Solar Explorer', by the Chilean Department of Energy, retrieved from http://solar.minenergia.cl/exploracion, 2021

We can then evaluate thermal expansion of the support frame considering thermalization at the minimum average temperature of -10°C, even though most measurements will probably be carried out during daytime within standard working hours. The simulations in SolidWorks consider a uniform base temperature of 25°C at which a temperature delta ΔT=-35°C is applied evenly on all the faces of the frame.

The simulations results, carried out with a thermal expansion coefficient of 68 um/um-°C for PLA and shown in Figure 5-15, result in a maximum displacement of 33 micron and a minimum displacement of 0.01 micron. The wall to which the camera is fixed by the tripod bolt shows displacements in the order of 15 micron, whereas the structures that support the grid show displacements in the order of 20 micron. Neither of these displacements is isotropic and while this is subject to vary due to the metallic frame of the grid acting itself as a structural element, we can attempt to estimate the change in the relative angle between the camera and the grid induced by thermal deformation. Moreover, this assessment assumes that these displacements occur in opposite directions that effectively vary the relative angle as shown in Figure 5-16, which corresponds to the worst-case scenario.

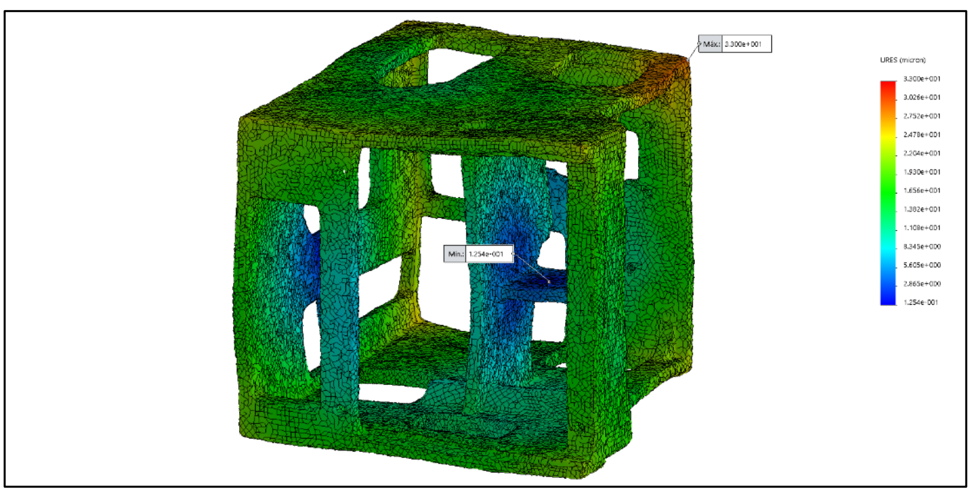

Figure 5-15. Thermal expansion simulation results amplified 500-fold for visualization purposes.

For the estimated displacements of 15 and 20 micron at 60 mm and 130 mm (the farthest ends of the camera and grid, respectively), the relative angle variation corresponds to 0.013° and 0.008°, which adds to ε = 0.021°. This value is well within the desired accuracy of the calibrator of 0.1° and will be taken into consideration when making a more detailed estimation of the total uncertainty in the polarization angle.

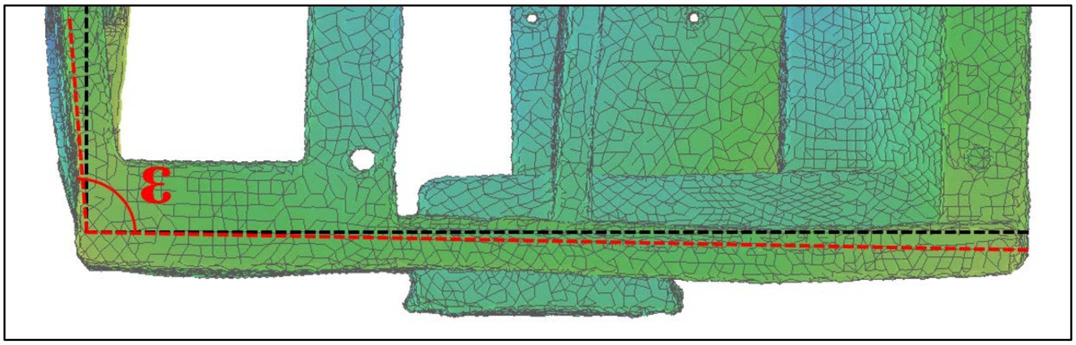

Figure 5-16. Illustration of the angle between the camera and the polarizer before (black lines) and after (red lines) the estimated displacements induced by thermal expansion.

5.1.2. Results of the mechanical frame implementation

The implementation of the mechanical frame was carried out using the FlashForge Guider II S-Series 3D printer available at the AIUC laboratory.

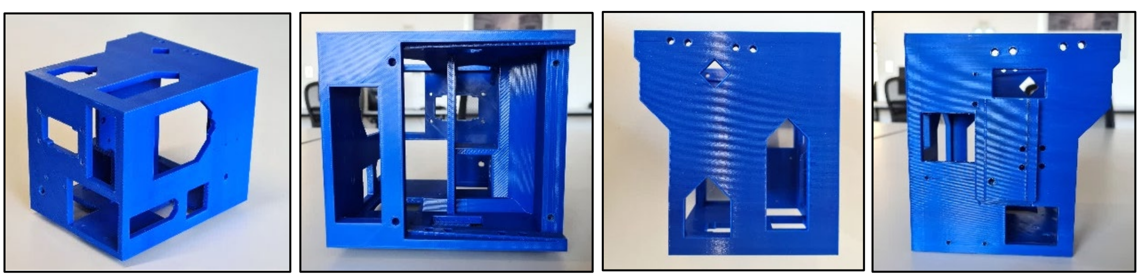

Figure 5-17. 3D printed mechanical frame.

The full system was weighted at 1.096 kg, which shows good agreement between the original estimation and the implemented design. This value is also below the 2 kg limit determined during preliminary test flights and, thus, the actual flight autonomy of the UAV-based calibrator could be able to slightly exceed that of maximum payload, originally estimated at 10 minutes.

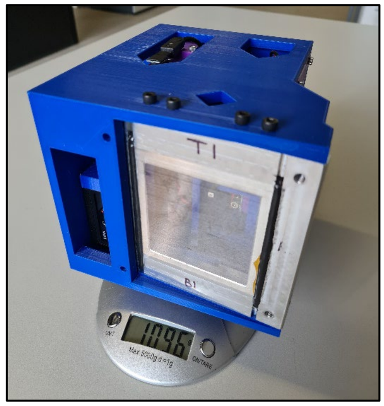

Figure 5-18. Weight of the flight-ready RF source.

The following images showcase different internal and externals views of the RF source and its elements.

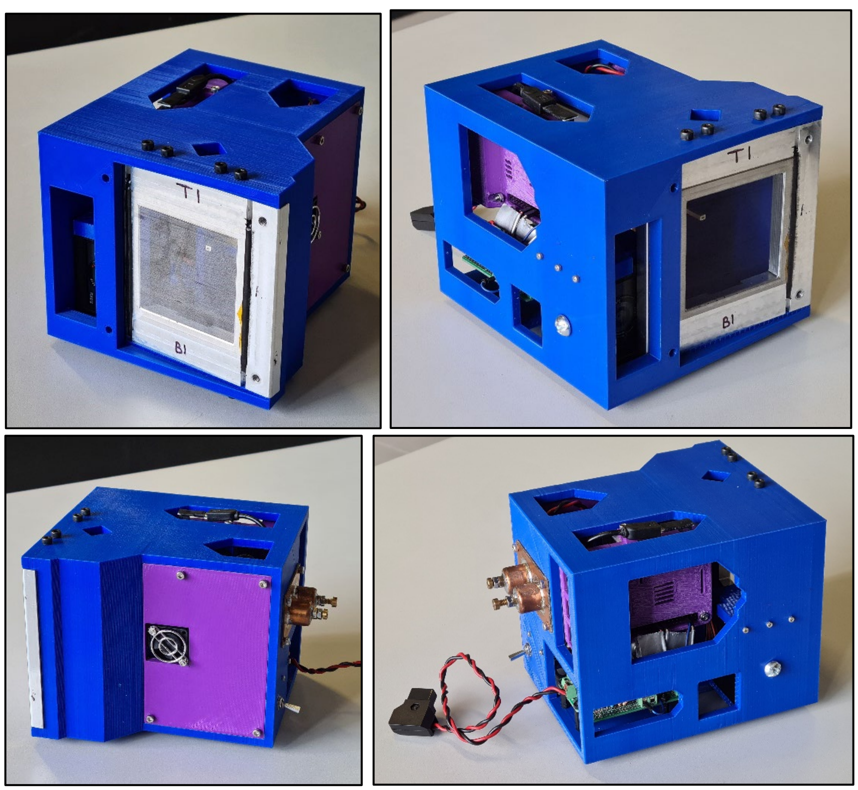

Figure 5-19. Views of the external elements of the integrated RF source.

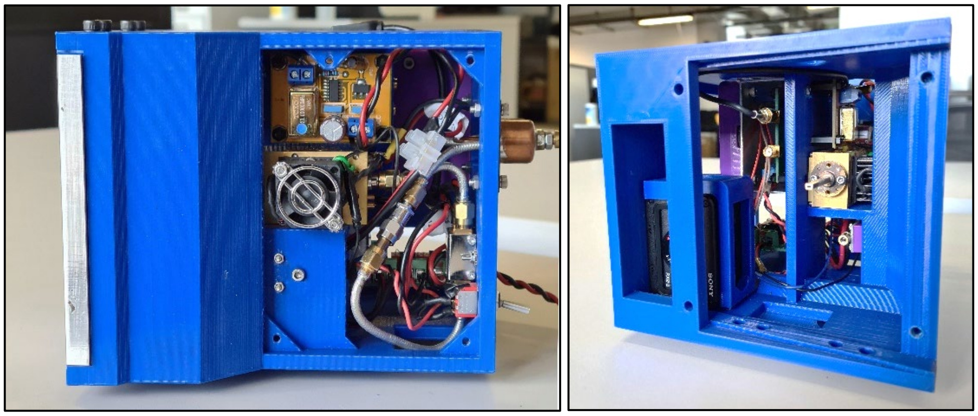

Figure 5-20. Views of the integrated RF source internals.

The integration of the source with the gimbal is shown in Figure 5-21, with the source connected to and powered by the gimbal's front 12 V P-TAP connector.

Figure 5-21. Integration of the source with the gimbal.

Finally, to ensure appropriate behavior of the gimbal's response with the new payload, a procedure of calibration of the gimbal's PID algorithm was carried out. This required connecting the gimbal to the computer with the DJI Ronin Assistant application and selecting the Auto-Calibration option, which ensured that the gimbal's response did not introduce resonance-induced vibrations. Further tuning may be needed depending on the actual conditions when at CMB telescope high sites.

Figure 5-22. RF source integrated with the gimbal and the drone at PUC campus.

From the results, we can conclude that the implementation of the support frame and integration of the RF components was carried out successfully. The thermal expansion simulations of the support frame showed that uncertainties of up to ±0.021° might be introduced into the polarization angle estimation, depending on temperature conditions. In practice, this value might be smaller, but this is difficult to quantify without specialized equipment to required reach the expected below-zero temperatures and to measure displacements of in the order of microns. Nevertheless, the estimation provided in this work should be enough to obtain a good estimate of the overall polarization angle accuracy of the calibrator.

5.2. Setup procedures for the characterization experiments

For the RF characterization experiments, the anechoic chamber of the AIUC laboratory was used. This chamber consists of an optical table in which a CNC robot can be mounted. The table supports a structure of aluminum beams on which grounded aluminum plates are installed, effectively isolating the interior from electromagnetic interference from outside sources, with inner dimensions of 119 x 174 x 83.5 cm (Height x Width x Depth). To minimize reflections and resonances that can be generated by the source within the chamber, the walls are lined with HR-10 Eccosorb[5], a type of high loss millimeter wave absorber that attenuates electromagnetic radiation by converting RF energy to heat.

The CNC robot can be reconfigured depending on the requirements of the experiment and up to 4 actuators can be controlled simultaneously. These actuators are controlled by an Arduino microcontroller, with which a Linux computer can interact via Python scripts to send commands or automate tasks.

To perform power stability, frequency stability and band power estimations, the Keysight N9020B mixed signal spectral analyzer (MXA) was used. The frequency range of this analyzer spans from 10 Hz up to 50 GHz, its amplitude frequency response is listed as ±0.47 dB (2σ) in the frequency range of interest and its current frequency accuracy can be calculated in proportion to $\pm f_{measured}\ x\ 7.4x10^{-6}\ Hz$ (Keysight Technologies, 2021). To reach the frequency band of the source between 130 and 160 GHz, a Virginia Diodes WR6.5 frequency extender was used. The intrinsic mixer loss of the MXA is typically 10 dB (Virginia Diodes, 2021), while its accuracy is listed to be within ±0.25 dB. The MXA can be controlled remotely via local area network by Python commands with a library provided by the manufacturer, which allows the automatization of the data collection.

Figure 5-23. Keysight N9020b Spectrum Analyzer (left) and VDI Frequency Extender WR6.5 without feed horn (right).

Prior to these characterization tests, the robot was reconfigured with of two linear

[5] https://www.eccosorb.eu/Eccosorb.html

actuators and two rotary actuators. Given their motion relative to the coordinate system we defined, these were denoted X actuator, for horizontal motion; Y actuator, for vertical motion; Roll actuator, for rotation around the X-axis; and Pitch actuator, for rotation around the Z-axis. An additional rotary actuator that can perform a rotation about the Y-axis, denoted Yaw actuator, was placed in a pedestal mounted on the optical table facing the CNC robot. The X and Y linear actuators[6] have a resolution of 0.02 mm and an accuracy of 0.01 mm. The rotary actuators[7] have a resolution of 0.02°, 0.01° and 0.01° degrees, and accuracies of 0.01°, 0.01° and 0.02°, for Pitch, Yaw and Roll, respectively.

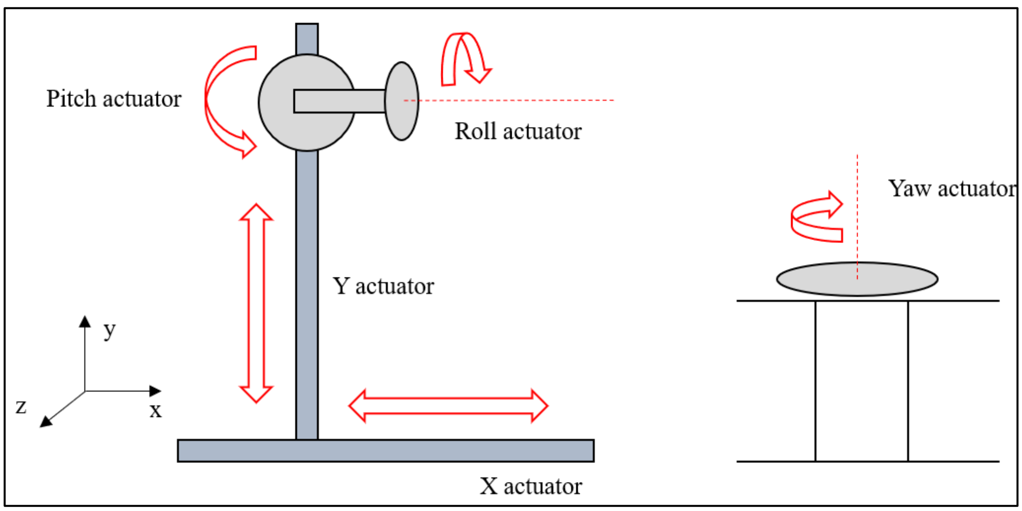

Figure 5-24. Illustration of the CNC robot setup.
Linear actuators are shown in light blue, while rotary actuators are shown in light gray.

The frequency extender was mounted on the CNC robot and connected to the spectral analyzer, which downconverts the signal to the frequency range covered by the spectral analyzer. The RF source's elements were connected and then incorporated into the mechanical support structure. The camera, laser and wire grid polarizer were also incorporated prior to testing to allow for the characterization to be carried out in a configuration as close as possible to the final flight-ready setup.

[6] Jy Instrument J04DP600-XZ
[7] Jy Instrument J01DX60 (Roll) J02DX100 (Yaw and Pitch)

The frame was placed inside the anechoic chamber and aligned in position by first measuring the vertical distance from the center of the waveguide to the base of the optical table and then setting the extender horn to the same height with the CNC robot. 100-sample-averaged (~17-second integration time) power measurements were carried out while varying the Y actuator position in steps of 0.2 millimeters, fine-tuning the alignment until maximum power was registered and then fixing the vertical distance. A similar procedure was carried out with the Pitch and Yaw actuators to ensure the orientation of the frame relative to the extender horn corresponded to 0°. The frame was first roughly aligned to the extender and then power measurements were carried out while adjusting the angle of the actuators in steps of 0.1° until maximum power was measured. Finally, all alignment procedures were repeated successively until no significant variations in maximum power were registered.

The above procedure considers that the waveguide's orientation of maximum power corresponds to ~ (0°, 0°), which was verified in MATLAB with simulations for an open waveguide radiation pattern carried out at 150 GHz, shown in Figure 5-25. In practice, the angle of peak power of the waveguide might differ from zero but this simulation is a good starting point and will be taken as a reference in later comparisons.

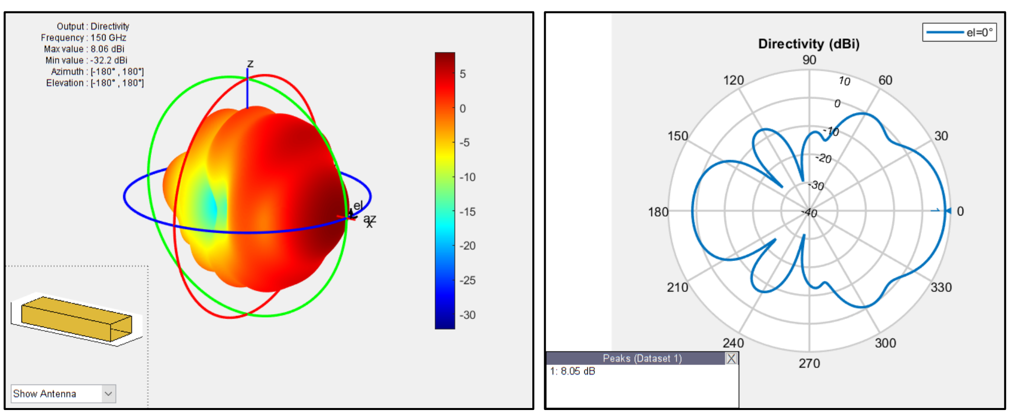

Figure 5-25. MATLAB simulations of an open waveguide at 150 GHz.
The expected waveguide radiation pattern in shown in 3D (left) and 2D at a 0° elevation cut (right). Maximum theoretical gain of ~8 dBi is expected at an azimuth angle of 0°, while the beamwidth was measured at 47.2°.

The extender horn and waveguide final height was measured at 43 cm from the base of the optical table, while horizontal distance from the end of the waveguide to the plane of the aperture of the extender horn was set to 75 cm. The experimental setup is shown in Figure 5-26.

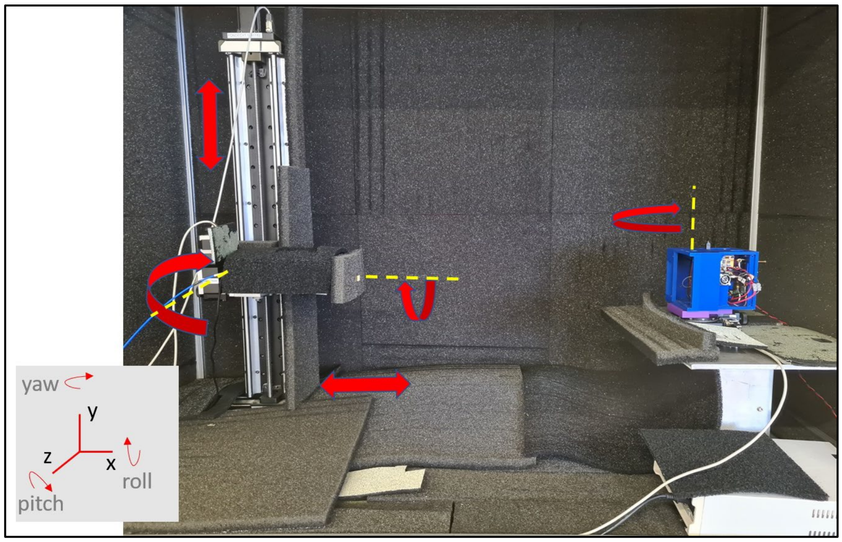

Figure 5-26. Setup of anechoic chamber during RF testing.
The horizontal distance from the source to the receiver is 75 cm, while the vertical distance from the floor of the chamber is 43 cm. The Y actuator is vertical, visible on the left side of the image, with the X actuator perpendicular (not visible), flat on the optical table surface. The Roll actuator supports the frequency extender and is mounted on the Pitch actuator (not visible). The RF source is shown on the right side of the image, mounted on the Yaw-actuator on top of the pedestal. The walls and floor of the anechoic chamber as well as other elements within the chamber were lined with Eccosorb to minimize reflections. The final Eccosorb layout differs from the one seen in this image.

5.2.1. CNC robot calibration

To generate more reliable results while measuring the radiation pattern and obtaining the polarization angle maps, the position and attitude of the robot's actuators was calibrated by using photogrammetry to estimate a model of the robot's movement. This model was used later to generate commands that accurately sweep the expected azimuth and elevation angles of the corresponding radiation pattern.

The robot calibration procedure involved placing coded photogrammetry targets in locations within the anechoic chamber, with the coordinates of at least 3 targets measured with high precision to act as a scale reference during processing. For this process, the Roll actuator was removed from the setup and a photo camera was placed in a 3D printed mount such that its position matches the expected position of the reception hardware (calculated with high precision from its 3D model shown later in Figure 5-47). The camera was used to take photos after each of a series of stepped movements of the X, Y and Pitch actuators, all of which were used together to perform radiation pattern measurements later. The Yaw actuator remained fixed during this experiment and, thus, was not calibrated. By using the photogrammetry software Metashape (Agilent), it was possible to find the center of the coded targets on each picture and obtain the 2D-image coordinates of each target. After performing the camera calibration in OpenCV, which estimates intrinsic parameters of the camera —e.g., aberrations—, the target's 2D coordinates are passed to an OpenCV script that can perform pose estimation from the complete set of pictures. The position and attitude of the camera at each step were then obtained from the OpenCV estimation.

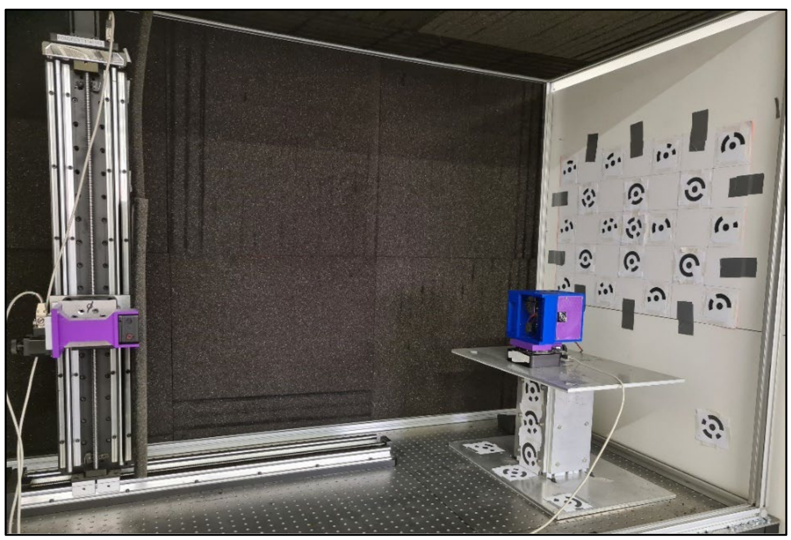

Figure 5-27. Anechoic chamber with coded targets during photogrammetric robot characterization procedures. On the right, a set of targets on the back wall were placed and centered precisely within a 10x10 cm grid, with other targets placed on known locations within the chamber. On the left, the camera is shown placed at the expected location of the ZBD feed horn when mounted on to the robot's actuators. Notice that the Roll actuator has been removed from the setup for these experiments.

In parallel, a Python script used to model the CNC robot was implemented based on a coordinate system and transformation library, originally created by Professor Rolando Dünner (AIUC) for the ACT project. The implemented script generates successive coordinate system transformations for each actuator in a given actuator chain. To define each actuator, its coordinate system must be established in 6-parameter cluster dubbed "Coordinates", which contains the actuator's X, Y, Z position coordinates and the Pitch (p), Yaw (w) and Roll (r) orientation angles referred to its parent actuator, i.e., the previous actuator in the chain. Similarly, its base unit of motion per actuator step must be established in a 6-parameter "Action" cluster. By declaring each actuator in the same order as mounted in the CNC robot, it is possible to determine the position of the last actuator (or last object) in the chain accurately in position and attitude.

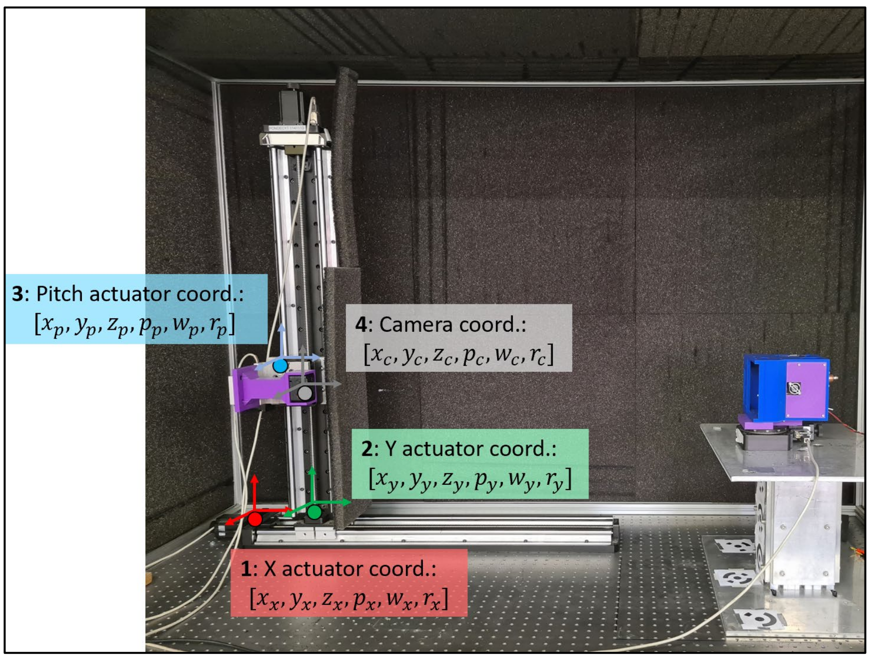

Figure 5-28. Illustration of the robot model's variables and local coordinate systems. In this model, for example, the x_y component indicates the X axis distance between the origin of the Y actuator coordinate system and the origin of the X actuator coordinate system. Should the X axis of the X actuator coordinate system be tilted (if defined through p_x, w_x and r_x), the X_y distance is measured on to this rotated X axis. The rest of parameters are defined with respect to the previous actuator in a similar manner.

To appropriately express the robot's model equation, we will make use of auxiliary operators that are required to define the base coordinate system transformations, listed below.

- The *R* operator: obtains the subsequent, equivalent rotation matrices from the input

Euler angles. It is expressed as

$$R(p,w,r)=\begin{bmatrix}1 & 0 & 0\\ 0 & cos(p) & -sin(p)\\ 0 & sin(p) & cos(p)\end{bmatrix}\begin{bmatrix}cos(w) & 0 & sin(w)\\ 0 & 1 & 0\\ -sin(w) & 0 & cos(w)\end{bmatrix}\begin{bmatrix}cos(r) & -sin(r) & 0\\ sin(r) & cos(r) & 0\\ 0 & 0 & 1\end{bmatrix} \quad \text{(Eq. 5.1)}$$

- The *M2E* operator: obtains the corresponding Euler angles from a 3x3 rotation matrix. It is described as

$$M2E\left(\begin{bmatrix}M_{11} & M_{12} & M_{13}\\ M_{21} & M_{22} & M_{23}\\ M_{31} & M_{32} & M_{33}\end{bmatrix}\right)=\left(\operatorname{atan}(M_{21},M_{11}),\operatorname{atan}\left(-M_{31},\sqrt{M_{32}^2+M_{33}^2}\right),\operatorname{atan}(M_{32},M_{33})\right) \quad \text{(Eq. 5.2)}$$

- The *A* operator: applies a rotation to a given orientation in Euler angles. The rotation to be applied is also declared in Euler angles. It is specified as

$$A(p,w,r)\begin{Bmatrix}p_i\\ w_i\\ r_i\end{Bmatrix}=M2E(\,R(p,w,r)\,*\,R(p_i,w_i,r_i)\,)=\begin{bmatrix}p_o\\ w_o\\ r_o\end{bmatrix} \quad \text{(Eq. 5.3)}$$

Finally, the base coordinate system transformation is defined by transforming the position parameters of the actuator and its orientation angles in two separate operations, shown in Equation 5.4. To express this transformation, we define the parameter cluster $\tilde{t}=[x_t,y_t,z_t,p_t,w_t,r_t]$ of an actuator, which represents the translation and rotation of the transformation to be applied, and a subsequent (child) actuator's parameter cluster $\tilde{q}=[x_0,y_0,z_0,p_0,w_0,r_0]$, which represents the position and orientation of a given coordinate system, that we want to refer to the former's coordinate system. The base coordinate system transformation is expressed as

$$T_{(\tilde{t})}\{\tilde{q}\}=\begin{cases}R(p_t,w_t,r_t)\cdot\begin{bmatrix}x_0\\ y_0\\ z_0\end{bmatrix}+\begin{bmatrix}x_t\\ y_t\\ z_t\end{bmatrix}=\begin{bmatrix}x_1\\ y_1\\ z_1\end{bmatrix}\\ A(p_t,w_t,r_t)\{p_0,w_0,r_0\}=\begin{bmatrix}p_1\\ w_1\\ r_1\end{bmatrix}\end{cases} \quad \text{(Eq. 5.4)}$$

To model the motion produced by each of the robot's actuators, a similarly defined coordinate system transformation is executed, but using an input $\tilde{m}=k\cdot\tilde{t}_a$, where the actuator's Action cluster is defined by $\tilde{t}_a = (ax_t, ay_t, az_t, ap_t, aw_t, ar_t)$. In $\tilde{m}$, k represents the number of steps commanded to move, which can be any real value. This transformation is defined as

$$T_{A(\tilde{m})}\{\tilde{q}\} = \begin{cases} R(p_m, w_m, r_m)\begin{Bmatrix} x_0 \\ y_0 \\ z_0 \end{Bmatrix} + \begin{bmatrix} x_t \\ y_t \\ z_t \end{bmatrix} = \begin{bmatrix} x_1 \\ y_1 \\ z_1 \end{bmatrix} \\ A(p_m, w_m, r_m)\{p_0, w_0, r_0\} = \begin{bmatrix} p_1 \\ w_1 \\ r_1 \end{bmatrix} \end{cases} \quad \text{(Eq. 5.5)}$$

The final robot model equation is given by successive transformations of coordinate systems of each declared actuator, which also includes the possible motion generated by each actuator. The result is the position and orientation of the final actuator (or object) expressed in world coordinates as

$$\tilde{P} = T_0\{T_{A0}\{T_1\{T_{A1}\{\ \dots \{T_{N-1}\{\tilde{P}_N\}\}\}\}\} \quad \text{(Eq. 5.6)}$$

By using the position coordinates and orientation generated at each step by the OpenCV pose estimation algorithm as the ground truth, each of the robot model's parameters can be obtained programmatically by using a multivariate minimization Python script. The script defines values for the Coordinates and Action parameter clusters of each actuator and generates a virtual robot. This robot is tasked to move to each of the points in the photogrammetry data obtained earlier, returning the position of its final actuator as output. The mean squared error between the requested and generated position/orientation is calculated for the full set of data and the algorithm attempts to minimize the error iteratively by adjusting the model's parameters.

The process described above required user supervision to remove degenerations that corresponded to heavily correlated model variables, e.g., the sum of the X coordinate values could be split among several actuators or lumped into just one, both able to produce equivalent results but with different physical implications. This was carried out by freeing or fixing certain components within the Coordinates and Action clusters before inputting them into the minimization algorithm. Freeing the component lets the software optimize its value, while fixing it is equivalent to setting to a given value (e.g., to 0) the corresponding parameter in the operators of Equation 5.6. The process to generate the robot model's parameters is summarized in the flowchart shown in Figure 5-29.

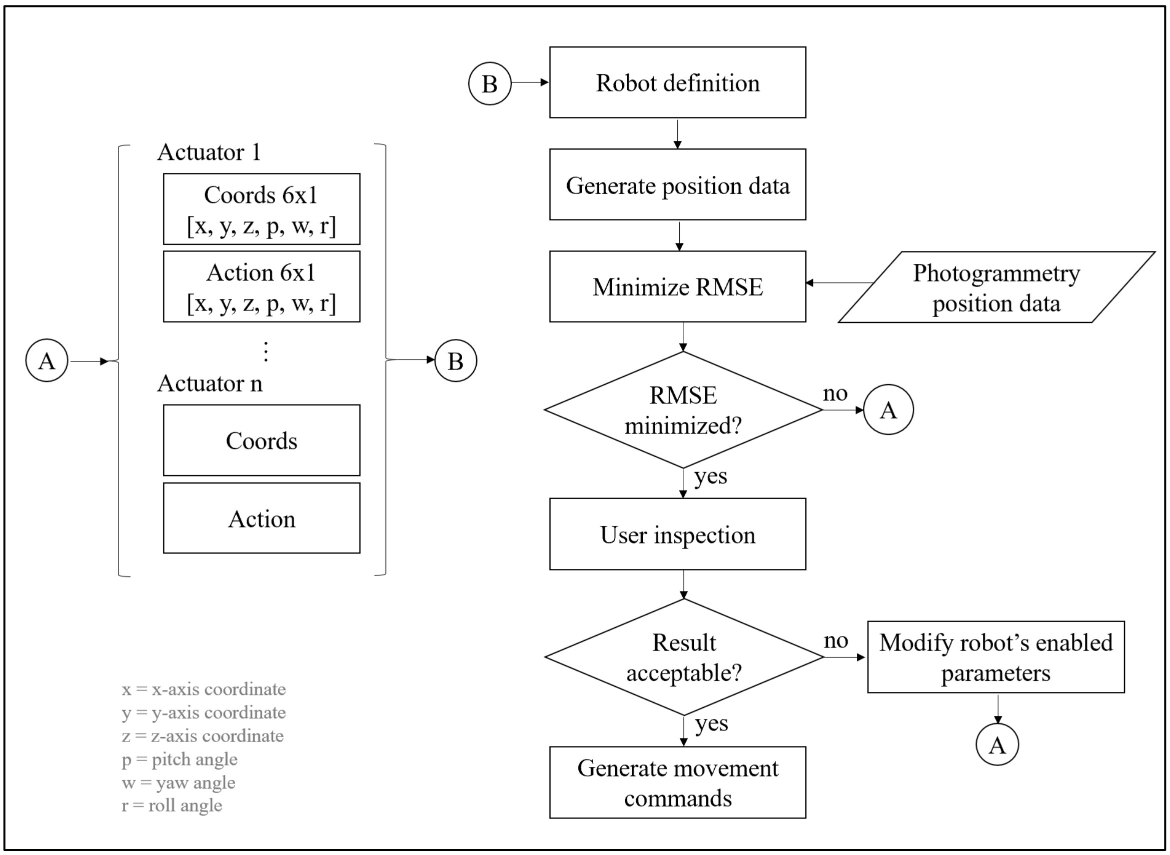

Figure 5-29. Flowchart of the algorithm used to generate the robot's model parameters.

The final model of the robot considered 3 actuators with non-zero Coordinates and Action clusters —X actuator, Y actuator and Pitch actuator—, and a final actuator with Action parameter cluster equal to zero, i.e., it cannot be actuated to produce motion, which corresponds to the object (camera).

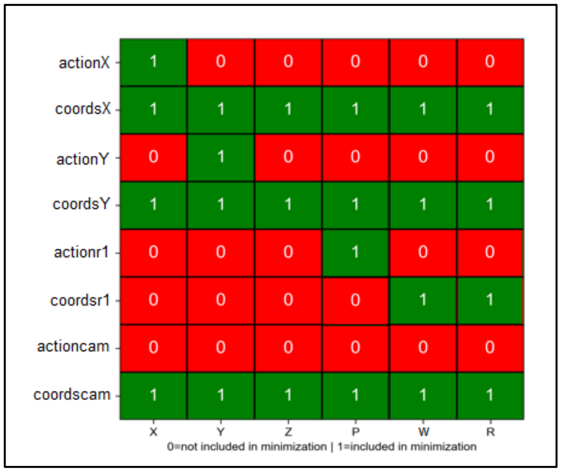

Figure 5-30. Table of the enabled and disabled variables of the robot's final model parameters. The disabled variables are equivalent to setting their value to a fixed number in the robot's equation, which is given by the starting parameter table of the minimization function.

Despite relatively small error values, shown in Table 6, we can deduce that some of these residual errors can be a result of effects not considered in the model, e.g., nonlinear deformations or position dependent actuator warps. A plot of the residuals at each of the 125 data points used to model the robot is shown in Figure 5-31 .

Table 6. Final error values of the data generated from the CNC robot's model parameters

X (mm)	Y (mm)	Z (mm)	Pitch (°)	Yaw (°)	Roll (°)
±1.5	±0.4	±0.2	±0.03	±0.02	±0.04

By using this method, we characterized the motion of the robot independently of the requested location, as well as other effects related to mechanical imperfections and misalignments, which also allows for some insight into the actual physical behavior of the robot. Thus, the resulting error values represent the expected uncertainty on any given position throughout the robot's range of action and not just the characterized section of 20 cm for the linear actuators and 20° for the rotation actuator. The larger error values on the X actuator are a consequence of the location of the coded targets relative to the motion of this linear actuator, which makes it harder for the photogrammetry software to estimate the displacement on each X actuator step. Nevertheless, this error value, as well as the rest, should be sufficient for the radiation pattern characterization process, e.g., the X uncertainty amounts to an error of less than 0.2% at 75 cm.

A final note of this section is that the attitude determination carried out for the radiation pattern characterization experiment is similar to the one that will have to be performed to analyze the camera footage after each flight of the calibrator and determine its attitude with respect to the telescope, which will also be carried out with photogrammetry landmarks and OpenCV. The results shown in Table 6 can then allow us to define an upper bound of the uncertainty on the polarization angle estimation from the analysis of the camera footage, for which the largest uncertainty of ±0.04°, corresponding to the Roll actuator, will be considered.

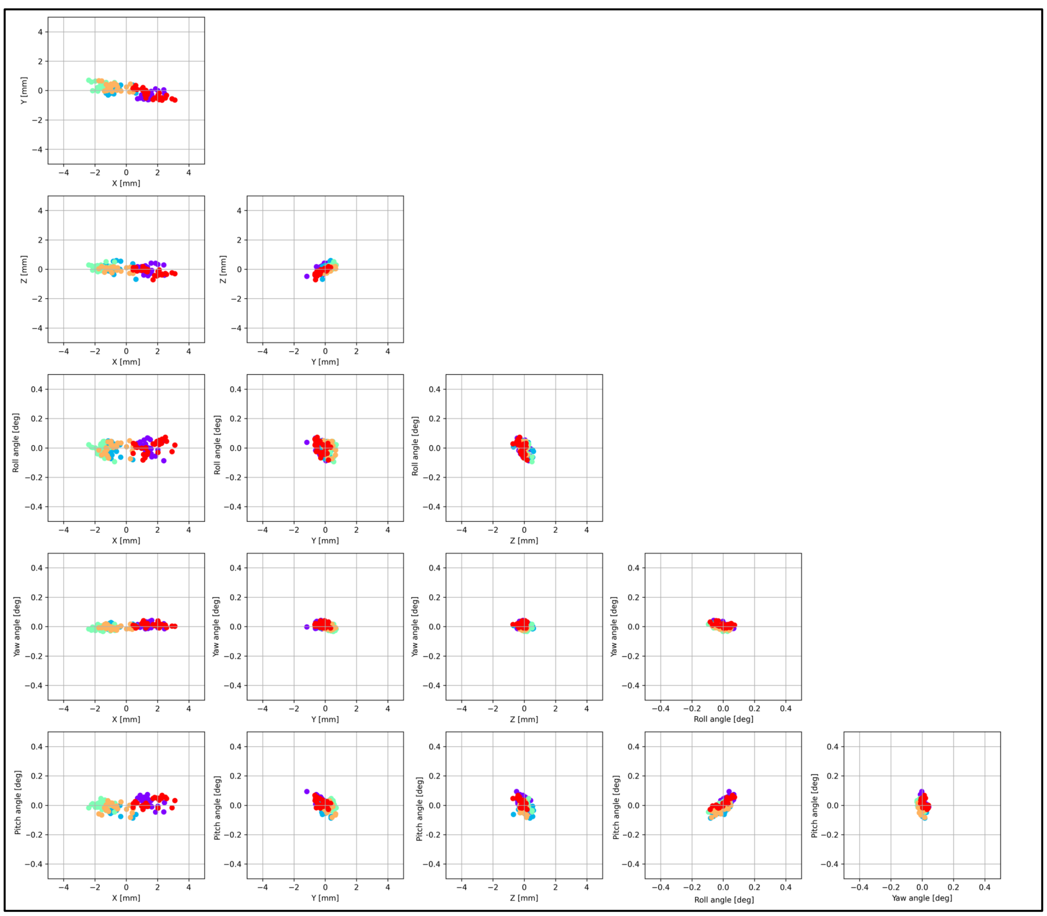

Figure 5-31. Plot of residuals for data generated from the final robot model parameters versus the original data. The original data was generated with 4 steps of 5 cm and 5° for the linear actuators and rotation actuator, respectively. The colors correspond to the distribution of points color-grouped per step of the Pitch actuator, which was used to try to find any correlations of the residuals with the actuator's motion.

5.3. Frequency stability characterization

5.3.1. Design of the frequency stability characterization experiments

The goal of the frequency characterization is to determine the frequency accuracy of the source and capture frequency drifts that may negatively impact calibration procedures.

In order to study the frequency response, the N9020B spectral analyzer was configured to continuously measure the power peak of the source at a given center frequency. The analysis bandwidth was set to 1 MHz with resolution bandwidth of 1 kHz to obtain a more precise estimation of the power peak frequency, while also lowering the Displayed Average Noise Level (DANL). The signal was measured 3000 times over the course of 10 minutes —which corresponds to the maximum expected calibration mission duration— before moving onto the next frequency point. A PC was used to access both the spectral analyzer and the RF source's Raspberry Pi in order to set the center frequency during measurements, simultaneously establishing the frequency of interest for both devices. Data was sampled repeatedly at each frequency, which resulted in the full frequency range measured across a total span of several hours at a relatively constant room temperature of 25° C. Prior to testing, a period of no less than 10 minutes with the source on was considered to allow for thermalization of the RF components.

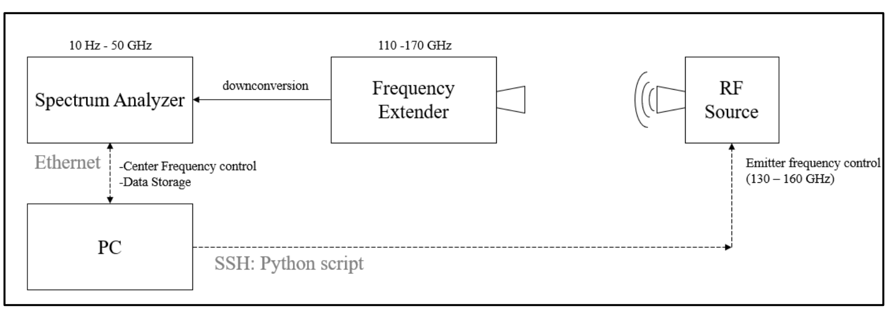

Figure 5-32. Frequency characterization measurement scheme.

The frequency band between 130 and 160 GHz was measured at 0.625 GHz intervals, which corresponds to 48 frequency points. This frequency interval was chosen a-posteriori after several iterations of experiments and based on the results of the band power characterization curve (see Section 5.5). This resolution was also deemed sufficient for characterization purposes, given that CMB telescopes have large bandwidths in the order of tens of GHz. For example, the ACT telescope bandwidth at 148 GHz is listed as 18.4 GHz (Swetz, et al., 2011), while the CLASS 150 GHz bandwidth is listed as 31.4 GHz (Dahal, et al., 2021).

To analyze the data, the mean frequency and the standard deviation of each data set was calculated, which allowed us to appropriately quantify the uncertainty in the measurement. In addition, the correlation matrix of the data set was calculated, measuring the correlation of each series of samples against each other for all frequency points. This allows us to determine if any of the sets show correlated behavior, such as variations in the performance of the spectral analyzer or the RF source during the measurement process, for example, due to temperature fluctuations. This would be evidenced by areas of the graph with similarly colored higher values of correlation.

5.3.2. Results of the frequency stability characterization

The histogram plots, from which a representative set is shown in Figure 5-33, show a good fit to a gaussian, with average skewness of -0.03 and average kurtosis of 5, the latter of which may indicate a larger number of outliers. To analyze these results further, 200-sample subsets at each frequency were taken from the data and analyzed for kurtosis and skewness. While the full set average value of kurtosis was large, the subset results showed that the sample size should not heavily influence this result, as the subset average kurtosis remained of the same order at 4.3. This may indicate that the large number of outliers in the data is a consistent feature, owing to either the measurement instruments or the source itself. Nevertheless, the standard deviations are in the order of kilohertz, which indicates a very stable behavior.

The correlation matrix shows an appropriate behavior, with each point in the array showing very weak correlations. The maximum absolute correlation value was very low at 0.05, while the average correlation (excluding the diagonal) was 0.01. The noise-like pattern of the matrix should serve as a reasonable indication that no noticeable instrumental fluctuations occurred during the measurements.

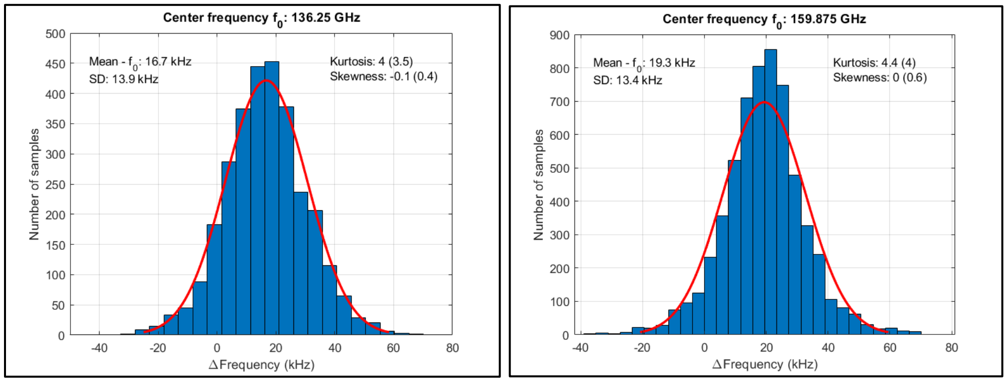

Figure 5-33. Frequency stability test results for 2 representative frequency points in opposing ends of the band. The graphs show frequency shifts obtained by averaging all 3000 samples and subtracting this value from the center frequency. The uncertainty in the measurement was calculated as the standard deviation of the fitted gaussian. In parenthesis, the average kurtosis and skewness of their 200-sample subsets.

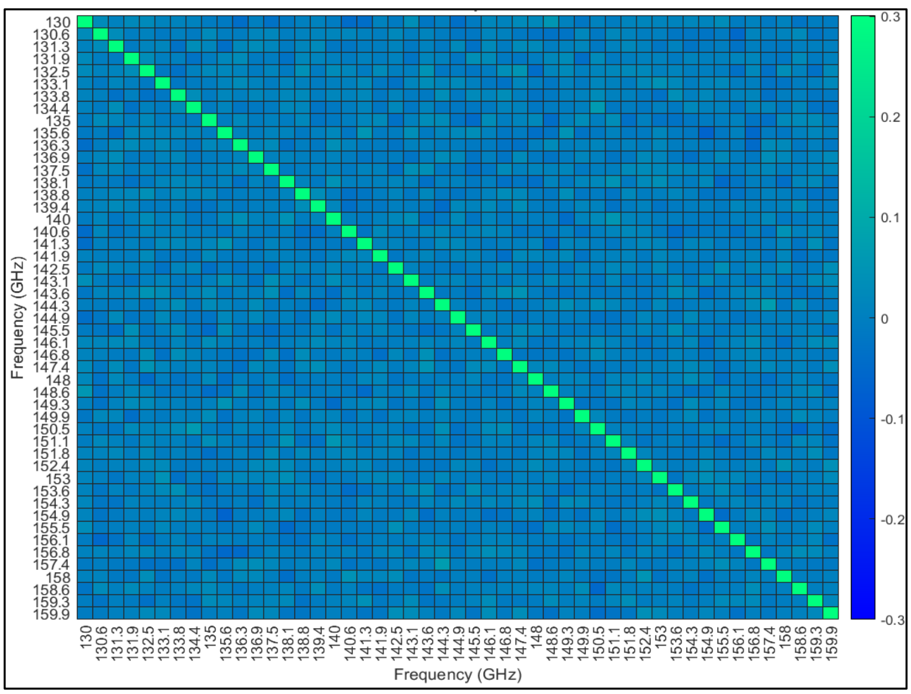

Figure 5-34. Correlation matrix of the frequency stability tests.
The range of the color bar is adjusted to highlight the pattern in the matrix. The diagonal cells, each with a value of 1, are shown saturated towards the maximum due to the displayed scale.

The results at each frequency are summarized in Figure 5-35, where the mean frequency delta for each center frequency and the standard deviation are plotted. The observed linear, upwards trend of the mean frequency delta can be attributed to a difference in the reference frequency between the local oscillator of the PLL and the one in the spectral analyzer. The steep drop of the standard deviation at ~138 GHz is produced by the PLL as it internally changes the circuit path used to produce the output signal; this can be inferred from the PLL's Output Power vs. Frequency graph shown in Figure 5-36, in which an abrupt jump in output power is listed at ~11.55 GHz (~138.6 GHz after the 12x multiplier).

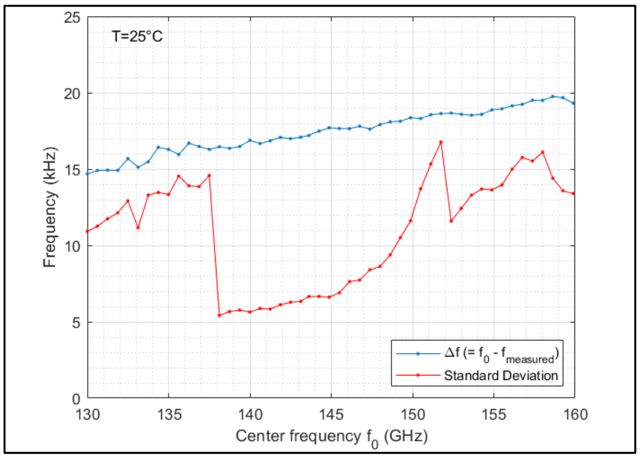

Figure 5-35. Summary of the frequency characterization.
The second major drop in the standard deviation plot at ~152 GHz has also appeared repeatedly in several trials of the frequency stability experiments, which would be explained by a hardware induced feature such as the one at ~138 GHz.

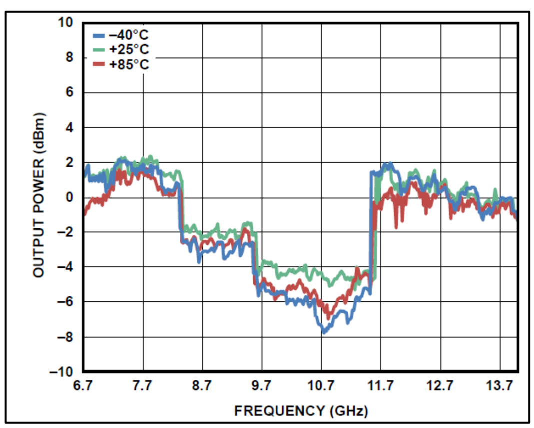

Figure 5-36. PLL output power vs. frequency.
From 'ADF5355 datasheet', Analog Devices, 2017.

The average center frequency shifts in the band remain in the order of kilohertz, as do the values of the standard deviation. These results are consistent with a frequency dispersion no higher 0.1 ppm (up to 17 kHz at 152 GHz), which arises from phase fluctuations in the signal due to the intrinsic behavior of the local oscillator. The declared frequency accuracy of the spectral analyzer is calculated and shown in Figure 5-37, which show systematic effects of up to ~1.43 MHz at 159.9 GHz. The measured data shows uncertainties that are orders of magnitude below this value, which suggests we can treat the measured dispersions as an upper bound that includes instrumental and source uncertainties.

These observed results should pose no issue for CMB experiments, as the bandwidth of these telescopes is in the order of tens of GHz, e.g., the measured dispersions correspond to a variation of ~0.0001% for an arbitrary bandwidth of 10 GHz at the highest measured uncertainty.

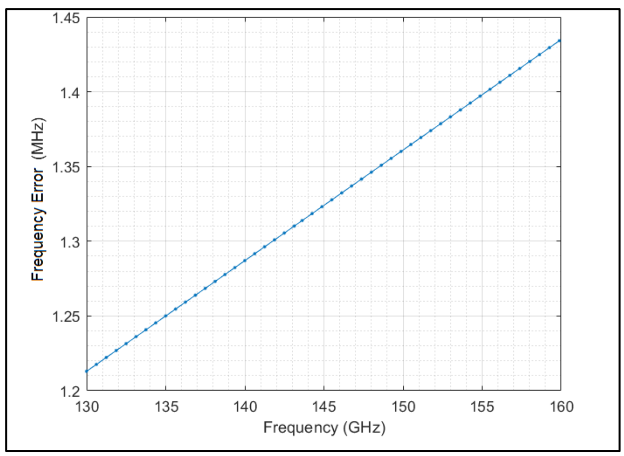

Figure 5-37. Frequency accuracy of the Agilent N9020b spectral analyzer in the frequency band of interest. The values were calculated as $f_0 \; x \; 7.4x10^6 + 251 \; kHz$, which derives from a combination of the initial calibration accuracy of the spectral analyzer, aging factor, time since last calibration, resolution bandwidth and frequency span.

From these results, we can conclude that the frequency behavior of the RF source should not produce any issues during calibration procedures of CMB experiments with the UAV-based calibrator. While the characterization was carried out at ambient temperature of 25°C, we can see from the supplier's information on the TCXO that its frequency stability is listed at ±0.2 ppm in the range of -10 to 60°C, which result in center frequency shifts of the same order as the ones measured in this experiment, even in the extreme temperatures found at CMB sites. Other components that may influence the frequency response of the source, such as the RF multiplier, show little information regarding performance at different ambient temperatures. Nevertheless, because of the wide margin for frequency variations given by the bandwidth of CMB experiments, these should not vary the results and conclusions significantly.

Finally, for polarization angle calibration of CMB experiments, the center frequency of the RF source is not as critical as the power variations that may be induced by the frequency shifts. In this regard, the band characterization experiment results (see Section 5.5) allow us to calculate that the largest frequency uncertainties seen in this experiment can be neglected, as they would produce a power output variation no higher than 0.0001 dB (0.002 %).

5.4. Power stability characterization

5.4.1. Design of the power stability characterization experiments

This experiment attempts to determine the stability of the RF source by continuously sampling the source's emitted power. This should evidence any behavior that may be detrimental to calibration procedures.

For these tests, the CNC robot, chamber, spectral analyzer, and frequency extender retain a setup similar to the one used for frequency calibrations. The spectral analyzer is now configured with a 1 GHz bandwidth (resolution bandwidth of 1 MHz), which allows us to measure the approximate source power from a single frequency bin. The frequency resolution during this experiment is still 0.625 GHz and, as will be shown later, this allows for the measurement and removal of power oscillations seen throughout the frequency band of operation (see Figure 5-41), seemingly produced within the chamber. A total of 3600 samples were taken at each frequency within 10-minute periods, in order to simulate the typical duration of the on-site flight missions. The full data set was obtained during the span of several hours at a relatively constant temperature of 25°C.

In this experiment we calculated the mean power and standard deviation of each set, in order to quantify the uncertainty in the measurement. In addition, the correlation matrix of the data set was calculated, whose results can allow us to infer whether or not component or instrumental effects were present during the measurement's timespan, e.g., noticeable temperature variations. These would otherwise appear as similarly colored extended sections in the correlation plot.

5.4.2. Results of the power stability characterization

The power stability correlation matrix, shown in Figure 5-38, presents maximum and mean correlations of 0.06 and 0.01, respectively, which indicate that the results are independent from one another, without statistically significant correlations.

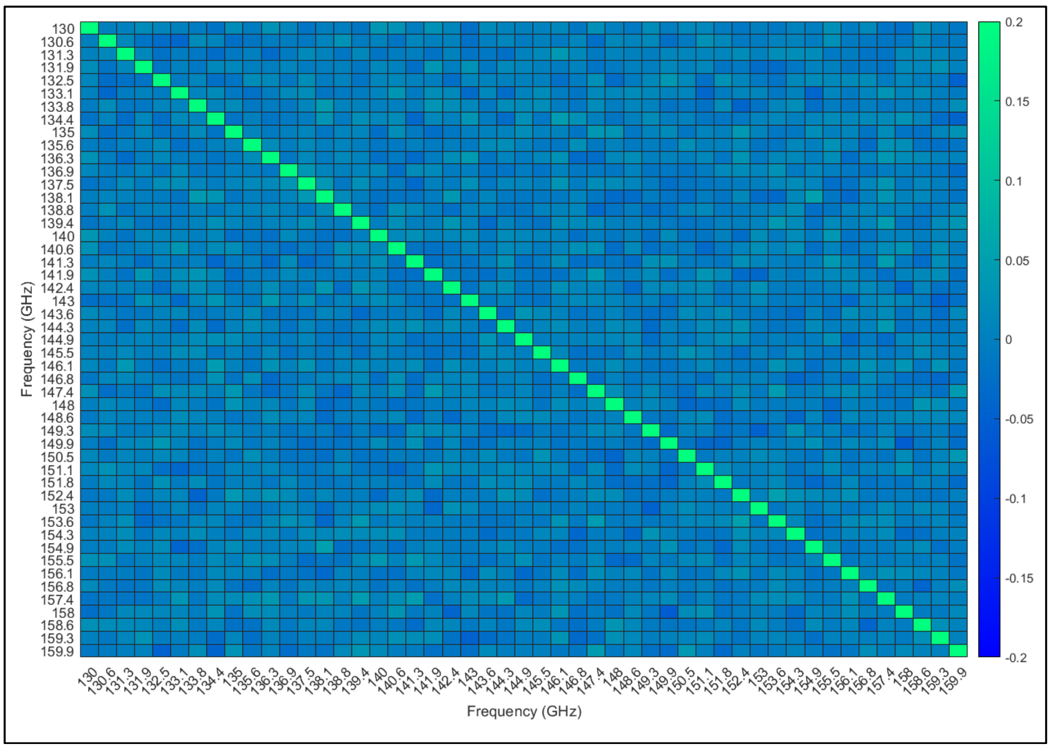

Figure 5-38. Correlation matrix of the power stability measurements.
The scale of the color bar is adjusted to highlight the pattern in the matrix. The diagonal cells, each with a value of 1, are shown saturated towards the maximum due to the scale displayed.

The graphs in Figure 5-39 show representative 3600-sample histogram results for frequency points at opposing ends of the band. The mean power at a given center frequency and the standard deviation are shown, with uncertainty also displayed as a percentage of measured average power at each frequency.

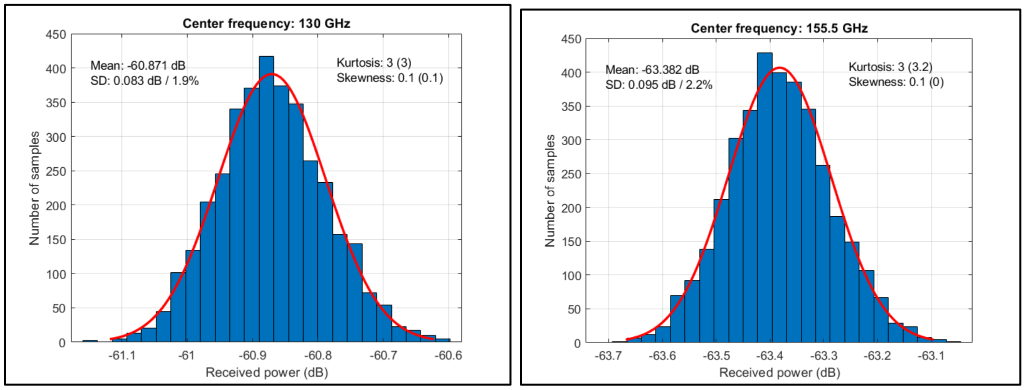

Figure 5-39. Representative results of the power stability characterization.
The average values of kurtosis and skewness for their 200-sample subsets are shown in parenthesis.

The histogram plots show an excellent fit to a gaussian, with average kurtosis of 2.9 and average skewness of 0, which indicates that the oscillations correspond to random noise. Additionally, 200-sample subsets at each frequency were taken from the data and were also analyzed for kurtosis and skewness. The subset analysis showed that the sample size should not heavily influence the results, with subset average kurtosis of 2.8.

The maximum and minimum measured standard deviations correspond to 0.161 dB (3.7%) and 0.071 dB (1.6%) at 146.8 GHz and 131.8 GHz, respectively, while the average standard deviation throughout the band was 0.106 dB. These results indicate that the power stability of the RF source is appropriate, with average fluctuations of 2.5% of the power output. The result seen in Figure 5-40 can also allow us to select a frequency that best fulfils the power stability requirements of the application within the calibrator's performance range.

The standard deviations calculated from the data represent statistical uncertainties that are within the 2σ performance of the spectral analyzer of ±0.47 dB and ±0.25 dB of the frequency extender (±0.53 dB combined accuracy). As in the previous experiment, we can assume that the measured uncertainties include the source-induced and instrument-induced fluctuations and are treated as an upper bound to the power stability of the RF source.

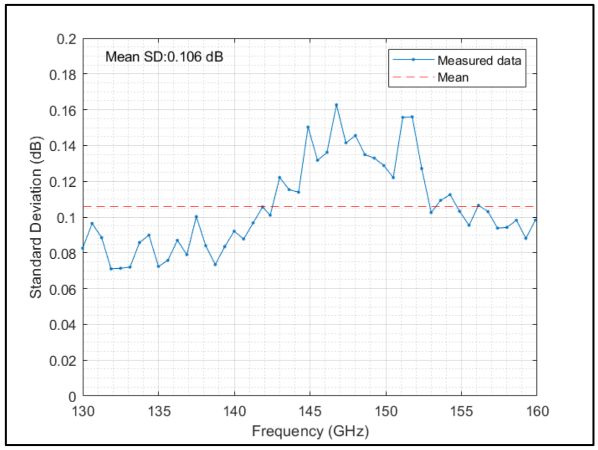

Figure 5-40. Measured power uncertainty as a function of frequency

Finally, we can conclude that uncertainties measured in this experiment should not pose issues during the calibration of the CLASS telescope, which is able to perform differential measurements between each pair of detectors and can thus remove the common-mode power. For other telescopes without this capability, the actual effect of these uncertainties is subject to the telescope detectors' equivalent noise power, sampling frequency, flight path of the aircraft during calibration procedures, among others. In general, a larger uncertainty would require longer integration times to minimize these variations across a larger sample pool; nevertheless, the measured values of dispersion are not large enough to represent a major concern even in this scenario.

5.5. Band power characterization and source power determination

The goal of the band power characterization is to define the expected power output of the source at a given frequency and allow us to make decisions based on the expected application and its power requirements.

The data for the band power characterization was obtained from the full set of power stability measurements. The result of the band power characterization is shown in Figure 5-41, in which we can see a pattern of periodic oscillations overlayed on top of the main power versus frequency curve.

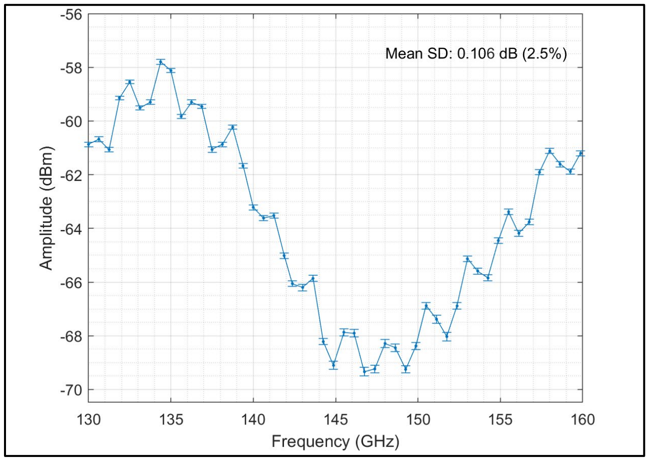

Figure 5-41. Result of the band power characterization.
Each point in the band consists of 3600 averaged samples and is overlayed with the error bar on the amplitude axis.

Given that the PLL and the multiplier are expected to produce a smooth curve with no abrupt variations in signal power, the observed oscillations must be produced either by standing waves formed between the transmitter and receiver, or reflections within the chamber's elements. The required path length to produce such oscillations results in ~0.4 meters for standing waves and ~0.8 meters for reflections. The dimensions of the experimental setup already negate the possibility of standing waves, making reflections the most likely cause of these oscillations. Considering the complex interactions between the chamber's reflecting elements, we will not attempt to determine source of the reflections, but rather remove them from the data to obtain the actual measured power.

To eliminate these oscillations, the Fourier transform of the original data was calculated, shown in Figure 5-42. From the spectral domain plot, we see peaks at ±0.43 spectral units, which match the observed time-domain oscillations.

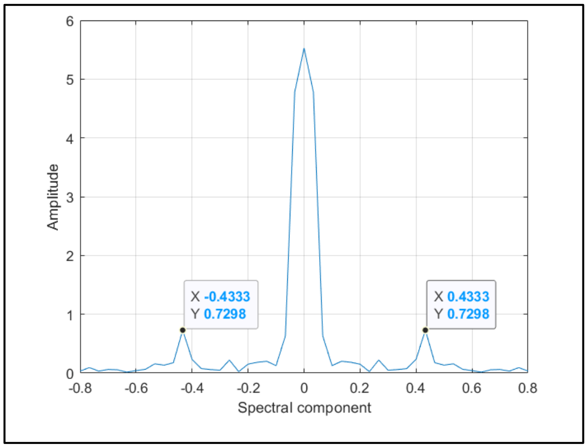

Figure 5-42. Spectral analysis of the band power characterization signal.
If we considered the original signal's x-axis units as time instead of frequency, the approximate period of the waves would result in an equivalent Fourier domain frequency of ~0.4 Hz. The peaks shown in the FFT plot show an appropriate match to this value.

By removing these peaks from the Fourier space, we can obtain the clean signal that corresponds to the actual power versus frequency response of the RF source. A narrow digital filter was tuned to remove the oscillations by optimizing to zero the mean of the residual between the original and corrected signal.

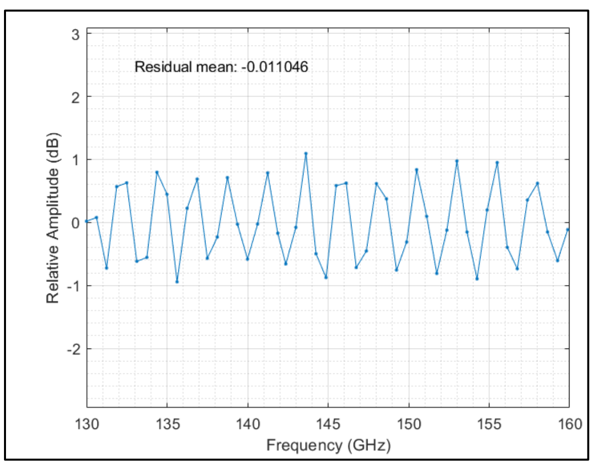

Figure 5-43. Plot of the residual between the original signal and the filtered signal.
The amplitude of the removed standing wave content is measured on average as ~1.5 dB peak-to-peak relative to the main RF source signal.

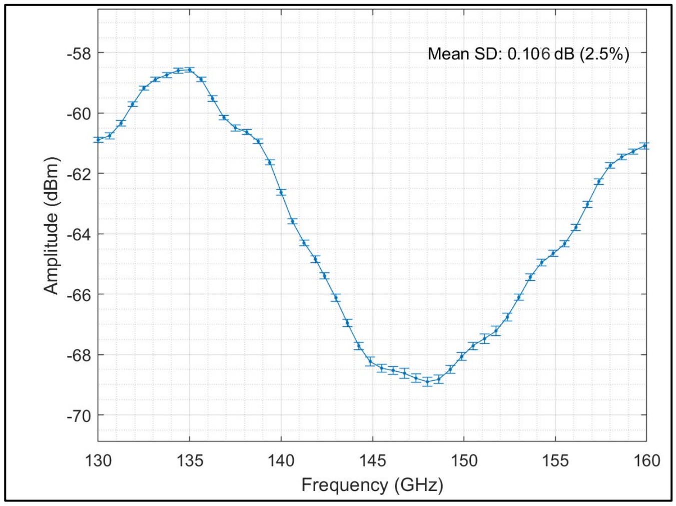

Figure 5-44. Corrected RF source power versus frequency curve overlayed with error bars at each measured frequency.

The final measured power versus frequency curve is shown in Figure 5-44, with the power uncertainties calculated in Section 5.4 shown as error bars overlayed on top of the graph. From this result, we must take into consideration the elements of the reception chain and the RF propagation loss in order to obtain the absolute power emitted at the output of source, given by

$$P_{source} = P_{meas.} + L_{coax} + L_{rx} - G_{horn_{rx}} + FPL \ , \qquad \text{(Eq. 5.7)}$$

where $P_{meas.}$ is the measured power at the spectral analyzer, L_{coax} is the loss in the coaxial cable between the frequency extender and the spectral analyzer, L_{rx} is the mixer loss in the frequency extender, $G_{horn_{rx}}$ is the gain of the frequency extender's pyramidal feed horn and FPL corresponds to the Free Path Loss, a frequency and distance dependent loss due to the transmission of the electromagnetic wave in free space. Free path loss is defined as

$$FPL = 20\log_{10} d + 20\log_{10} f + 20\log_{10}\left(\frac{4\pi}{c}\right), \qquad \text{(Eq. 5.8)}$$

where d corresponds to the propagation distance of the electromagnetic wave, which is equal to 0.75 m for this experiment, and f corresponds to the frequency of the wave.

The gain of the pyramidal horn at the input of the extender is listed at 24 dB, from which a typical loss of 2 dB from the theoretical value is subtracted. The extender's nominal conversion loss is listed at 10 dB[8], while the loss in the 1.2-meter calibrated coaxial cable has been measured at 3 dB at the band of interest. The power output of the source at each point in the frequency range can be then calculated as:

$$P_{source} = P_{meas.} + 3\ dB + {\sim}10\ dB - 22\ dB + FPL\ , \qquad \text{(Eq. 5.9)}$$

The power output of the RF source, shown in Figure 5-45, represents the lowest power that can be emitted at each frequency at the current configuration, while higher values of power can be obtained by setting the multiplier's analog attenuation to lower values. The added jaggedness on certain sections of the curve is due to the frequency extender mixer loss manufacturer's curves, which needed to be interpolated to the frequency values evaluated in this work.

Figure 5-45 shows that the frequency dependance of the RF source's power output can be used to define the center frequency based on the application's power requirements, with a peak-to-peak power span of ~9 dB. For the CLASS project, the plot shows that the RF source's output power is above the transmitted power upper limit of -7.8 dBm at 500 meters (see Figure 4-3). Given that the multiplier's output power is linearly related to the input power, the current 10 dB passive attenuator at the filter output —which ensures power at the multiplier's input no higher than ~3 dBm, as per its specifications— should be replaced with a larger one for the source emitted power to be below the required threshold. Attenuator values up to 20 dB have been tested with reliable results; for larger attenuator values, the multiplier's response becomes nonlinear and less predictable. At the maximum possible attenuation of 20 dB, the source could remain below the 500-meter maximum power threshold for the CLASS project at frequencies between 139.7 GHz and 156.5 GHz.

---

[8] A per-frequency-point loss value was applied from the manufacturer's specifications

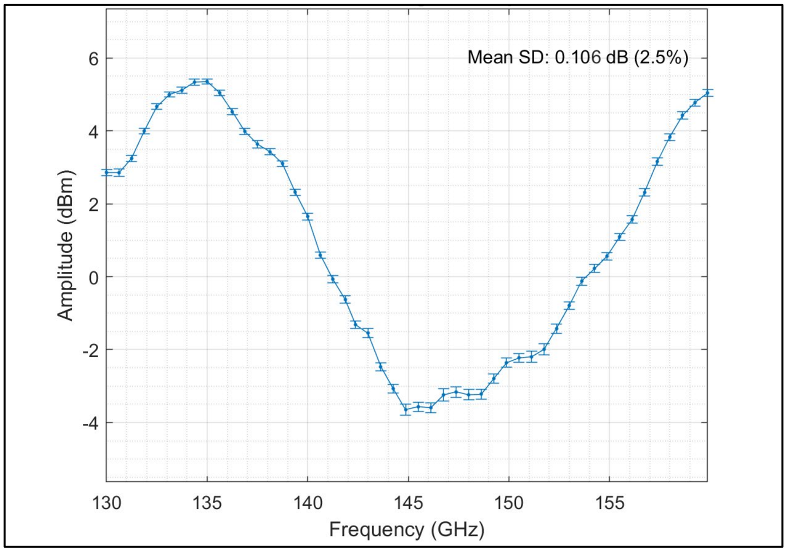

Figure 5-45. Final power output of the RF source as a function of frequency.

Should other telescopes or applications require emitted power to be even lower (i.e., require passive attenuators greater than 20 dB), a better alternative to modifying power at the multiplier's input would be to adapt external attenuators at the multiplier's output, between the multiplier and the waveguide, which ensures that the multiplier performs appropriately even in this scenario.

5.6. Polarization angle characterization

5.6.1. Design of the polarization angle characterization experiments

- **Measurements based on the frequency extender**

The RF multiplier coupled to the open waveguide antenna should produce a highly linearly polarized signal oriented in parallel to the shorter dimension of its cavity (Milton & Schwinger, 2006). Moreover, by using a wire grid in front of the waveguide, the polarization of the signal should be ensured or even enhanced, depending on the manufacturing quality of both the grid and the waveguide. As a crucial element to the UAV-based calibrator, the polarization angle properties of the source should be studied as thoroughly as possible.

By using the Roll actuator, it is possible to rotate the extender around the X axis and thus map the power response of the source depending on the angle of the extender horn with respect to the waveguide (an example of this procedure is shown in Figure 5-46). Forty-sample-averaged power measurements (~7-second integration time) taken every 0.5° with and without the grid were deemed sufficient to obtain a smooth, repeatable curve that can then be fitted and used to obtain the polarization angle from the formula shown in Equation 2.18.

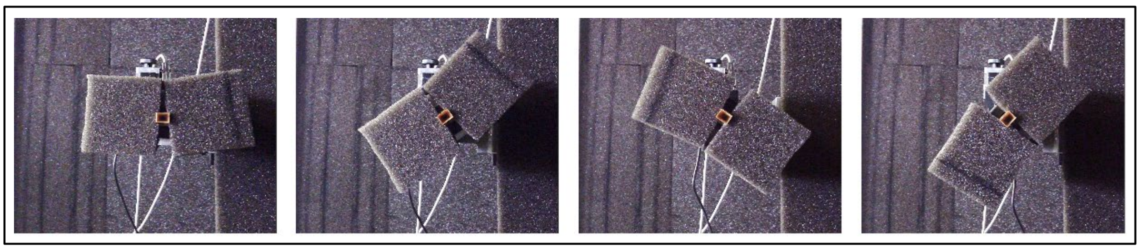

Figure 5-46. Rotation of the extender for polarization angle measurements, as seen from the RF source. Due to limitations imposed by the extender power supply and RF output cables, the effective measurement range spans from -10° to 230°.

However, as will be shown in the results sections of this experiment, the power curve of the RF source showed an irregular response in the vicinity of the 0° and 180° angles, which was attributed to the mechanical structure of the extender sagging as the Roll angle was varied. Thus, the measured response was subject to variations in power that caused the results to be unreliable, despite polarization angle measurements with and without the grid showing appropriate behavior. For this reason, an additional polarization measurement experiment was implemented in the form of a continuously rotating polarimeter.

- **Measurements based on the rotary polarimeter: relative polarization angle measurements**

A high-speed rotary stage was mounted on the CNC robot instead of the Roll actuator, on which a Virginia Diodes WR-6.5 Zero-Bias Detector (ZBD) diode was mounted via a 3D printed structure. The ZBD is a bolometer, which integrates power from all sources within its band of sensitivity and generates a voltage output proportional to the received power. The small footprint and weight of the ZBD should eliminate mechanical issues like the ones observed in the previous experiment.

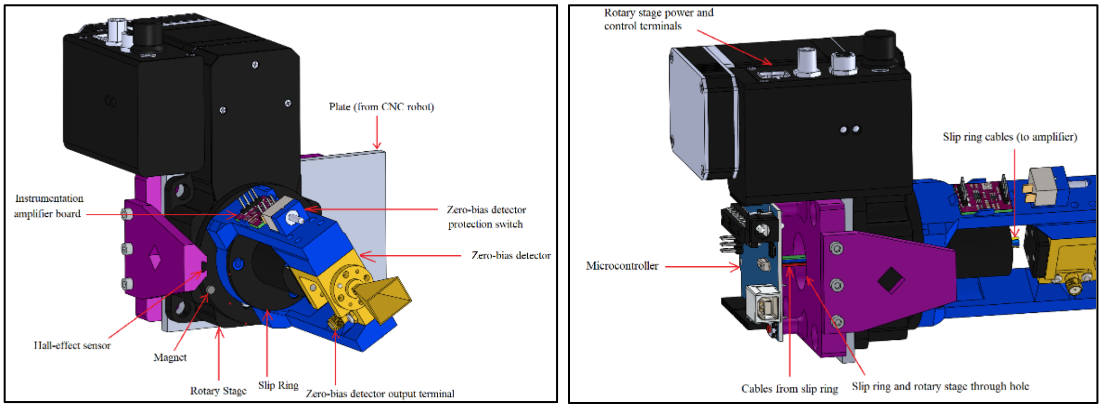

Figure 5-47. Illustration of the 3D design of the rotating polarimeter (cable layout not shown).

The DC output of the ZBD is connected to an AD620 instrumentation amplifier module and then fed to the Arduino's 10-bit ADC port through a slip ring mounted into the rotary stage. In parallel, the Arduino will also read the signal of a Hall-effect sensor that is activated by a magnet placed at the 0° reference of the rotary stage. Data is then logged into a high-speed MicroSD card by the Arduino, while the control of the Zaber RSB-E high-speed rotary stage is handled through a PC via a python script. By using this configuration, the phase can be demodulated from the measurements and allows for more precise, albeit relative, polarization angle measurement.

For this experiment, the frequency of the source was fixed at 144 GHz, as the source's polarization angle should not be frequency dependent. Knowing the source's output power from previous experiments and the sensitivity of the ZBD from the manufacturer's datasheet, the multiplier's attenuation was removed, and the gain of the instrumentation amplifier was set to 1000. To ensure maximum resolution in the digitized waveforms, the reference voltage of the ADC was set to 3.645 V (3.5 mV per ADC step), roughly 5% higher than the maximum measured voltage of the hall-effect sensor during 5 RPM operation at the 70-cm distance from the source defined for these experiments. The ADC ports of the Arduino were configured to sample at 9000 Hz, sampling the detector and sensor every 0.2°. This resolution that should be sufficient for this experiment, as we are mostly interested in the shape sinusoidal wave.

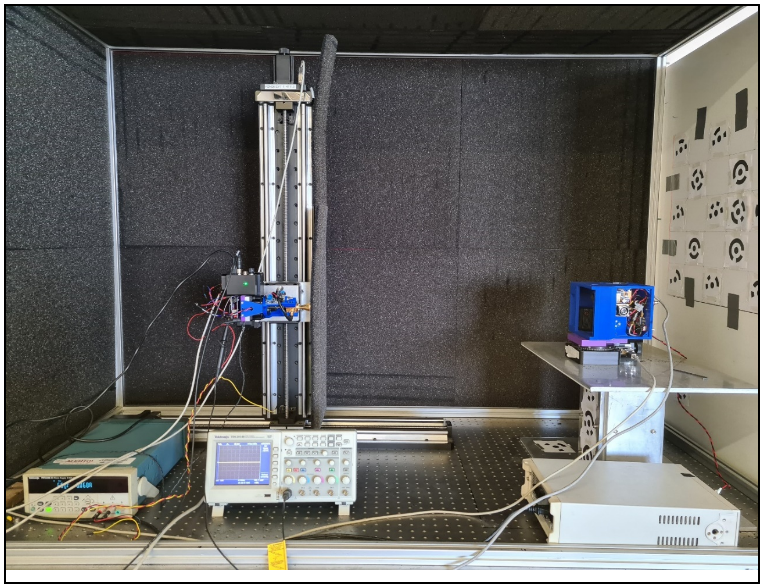

Figure 5-48. Early tests during the design of the rotary polarimeter.

The relative polarization angle that can be obtained from these measurements corresponds to the relative angular distance between the zero reference, i.e., the position of the magnet, and the location of maximum power measured by the ZBD. This can be determined from the phase of each signal by calculating the complex Fourier Transform and obtaining the fundamental frequency component, which should be produced at the rotation frequency of actuator for the hall-effect sensor signal and at twice of this value for the detector signal due to the intrinsic polarization sensitivity of the feed horn.

The relative angle between the hall effect sensor and the ZBD can be described in terms of two periodic waves with different frequencies:

$$a(t) = A_a.\cos\left(2\pi f_a(t - \Delta t_a)\right), \quad \text{(Eq. 5.10)}$$

$$s(t) = A_s.\cos\left(2\pi f_s(t - \Delta t_s)\right), \quad \text{(Eq. 5.11)}$$

where $a(t)$ corresponds to the actuator sensor signal with amplitude A_a, frequency f_a, period T_a, time offset Δt_a and phase shift $\sigma = \Delta t_a/T_a$. In turn, $s(t)$ corresponds to the ZBD signal, with amplitude A_s, frequency f_s, period T_s, time offset Δt_s and phase shift

$\phi = \Delta t_s / T_s$. From the conditions set earlier, we know that $f_s = 2f_a$, so Equation 5.11 is rewritten as

$$s(t) = A_s . \cos\big(2\pi . 2f_a(t - \Delta t_s)\big) \qquad \text{(Eq. 5.12)}$$

We are interested in the phase difference between the two signals, related to the time domain offsets of the signals by

$$\tau = \Delta t_a - \Delta t_s \, , \qquad \text{(Eq. 5.13)}$$

which can then be rewritten as

$$\tau = \frac{f_a}{2\pi}\left(\sigma - \frac{\phi}{2}\right), \qquad \text{(Eq. 5.14)}$$

and, thus, taking as a reference the phase and frequency of the hall-effect sensor signal, the relative phase ξ between the ZBD signal and the hall-effect sensor to be calculated from each measurement finally corresponds to

$$\xi = \sigma - \frac{\phi}{2} \qquad \text{(Eq. 5.15)}$$

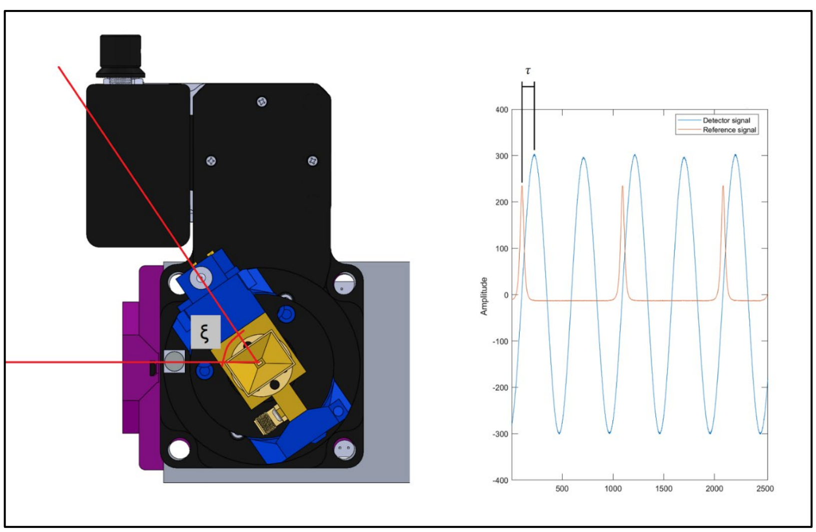

Figure 5-49. The measured angle with the rotary polarimeter (left) and expected signals (right).

Tests of the rotary polarimeter show that the measured relative angle is highly repeatable: for example, 20 separate measurements with the RF source fixed in place while taking data for as little as 3 seconds on each instance resulted in a standard deviation no higher than 0.05°. This method does show a slight dependence on standing wave amplitude and reflections, shown in Figure 5-50, as the ZBD is a bolometer and is only sensitive to the $\hat{E}$ component of the EM wave. Reflections and standing waves can alter the angle in which the highest or lowest power is measured and thus the relative angle measured by this device may change.

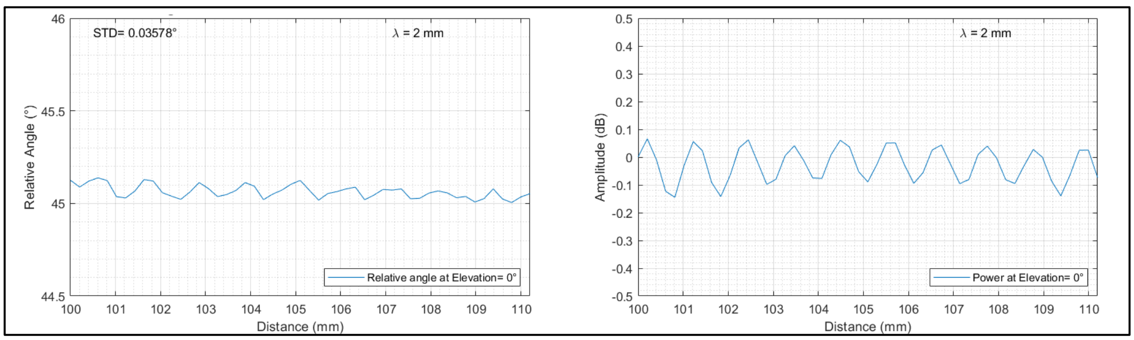

Figure 5-50. Measurements of the relative angle (left) and power (right) with the rotary polarimeter. Standing waves are produced by interference of the emitted and reflected wave when linearly moving the detector in 0.2 mm steps ($\lambda/5$) at 0° azimuth and 0° elevation. For standing waves of this characteristics, the dispersion of the relative angle remains small.

- **Measurements based on the rotary polarimeter: relative polarization angle maps**

Aside from allowing us to compare the relative angle with and without the polarizing grid, the rotary polarimeter can also allow us to study any significant variations of the polarization angle throughout the measured pattern of the source.

Several factors, such as the dimensions of the anechoic chamber and the expected number of points to measure, allowed us to define that the angular span of the map, from -10° to 10° each for elevation and azimuth, with angular resolution of 1°. This will be sufficient to identify any trends in the data that require further study.

To perform the required range of motion in this experiment, the CNC robot was combined with the Yaw actuator, located on the pedestal, on the other end of the chamber (see Figure 5-51). For an elevation equivalent motion, the linear actuators define the position of the reception hardware during tests and its attitude is determined by the Pitch actuator. For the azimuth equivalent motion, the Yaw actuator performs rotations that are equivalent to the rotary polarimeter rotating around the RF source.

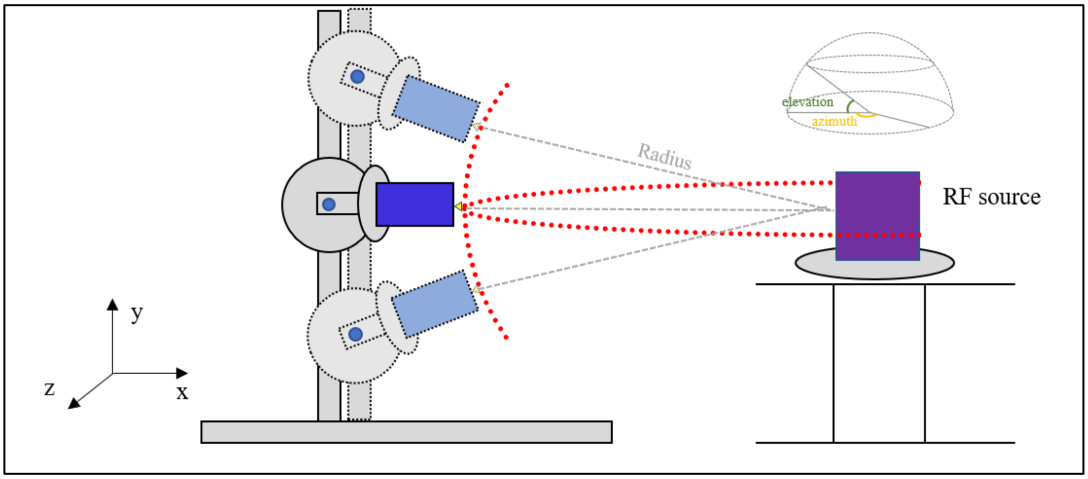

Figure 5-51. Illustration of actuator motion during the relative polarization angle map measurements.

To generate the set of coordinates required to sweep the spherical surface around the RF source, the robot was placed at measured distance of 70 cm from the source using a laser telemeter with 2 mm accuracy. Then, the vertical position of maximum power is defined in a similar fashion as in Section 5.2. This point is established as the 0° elevation position, whose world coordinates are used as a starting point to determine the ones for each elevation. Afterwards, a script is tasked to generate the actuator steps (i.e., their positions, represented as blue dots in Figure 5-51) needed to minimize the error between the camera position as generated by the CNC robot model and the requested coordinates (represented as red dots in Figure 5-51). This allows the reception hardware to both be in the expected position within the section of the sphere and to be pointed correctly towards the RF source. After each sweep along elevation, the Yaw actuator is then moved a step to the next position until the -10° to 10° azimuth range is swept. For this procedure, the Yaw actuator rotation axis was aligned to the mouth of the open-ended waveguide, which ensured that rotation was performed as precisely as possible, shown in Figure 5-52.

The final uncertainty in the elevation positioning was calculated to be better than ±0.04° within the angular span of the measurements, which arises from a combination of the angular uncertainty generated by the linear actuators (including the laser telemeter) and the uncertainty in the Pitch actuator. The azimuth positioning uncertainty depends on the Yaw actuator's accuracy and the robot model's error values, calculated to be better than ±0.03°. Both parameters are appropriate to perform the estimation of the RF source's beam pattern.

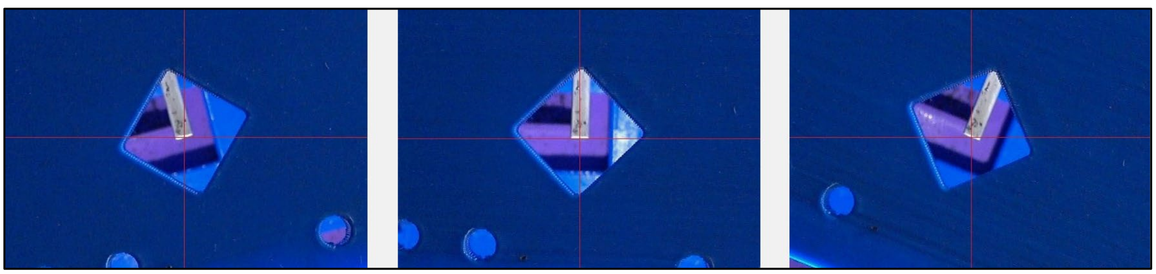

Figure 5-52. Verification of the rotation of the RF source at arbitrary angles after aligning the waveguide to the Yaw actuator's rotation axis.
The mouth of the waveguide stays in the same point throughout the rotations, marked with red lines.

5.6.2. Results of the polarization angle characterization using the frequency extender

From a deeper examination of the extender rotation, we found that there are small displacements of the horn's center with respect to its expected position, most likely due to the sagging of the structure of the extender as the extender rotates. These can produce variations in the signal calculated to be up to 0.1 dB or ~2%. Thus, the displacements of the frequency extender should be responsible for only a fraction of the observed power variations seen in several results (see Figure 5-53). However, other center frequencies show variations of up to 10% in signal power, e.g., at 139 GHz, which could not be attributed to the mechanical setup.

While the curve fit was appropriate in most cases, the variations in the measured polarization angle and in their error values make these results unreliable. The most important conclusion of this section is that the effects that alter the polarization angle in this experiment must have a different cause than the mechanical setup, such as standing waves or reflections. This is especially true considering that this experiment relies on per-point measured power, which can be altered by unanticipated sources.

In this experiment, the polarization angle is referred to the setup of the chamber and measurement equipment; however, the actual polarization angle as determined from in-flight data will be referred to the sky through georeferenced landmarks, which are themselves referred to the camera/laser system through photogrammetry. Thus, the relative angle between the wire grid and the metrology camera should be a better indicator of the quality of the polarization angle for the UAV-based calibrator.

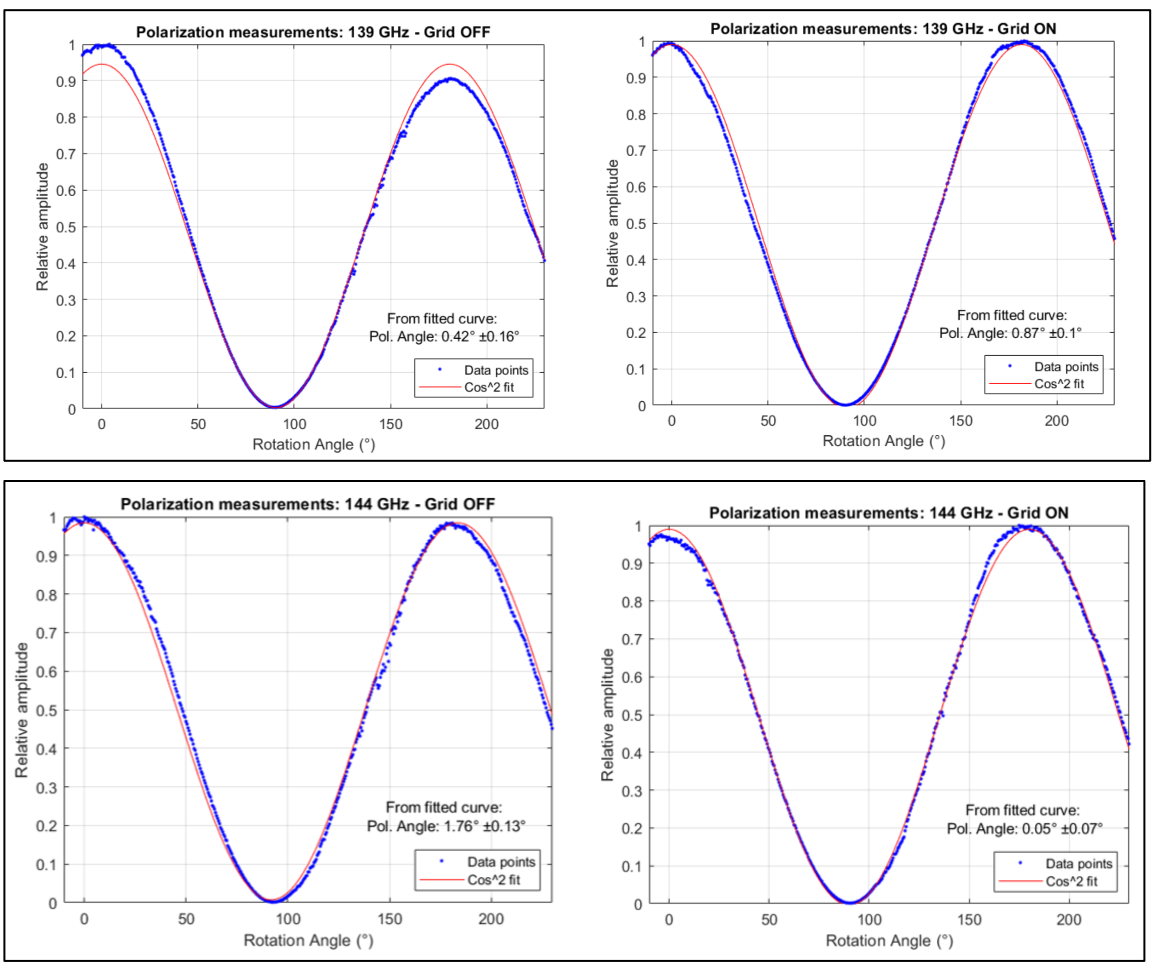

Figure 5-53. Various results of the polarization angle measurements.
Notice deviations from the expected curve at certain sections of the curves, which are a combination of mechanical displacement of the reception hardware and standing waves within the chamber.

5.6.3. Results using the rotary polarimeter

- **Relative polarization angle**

The timestream obtained from the measurement system shows very well-defined waveforms with large signal-to-noise ratio for both the ZBD and the hall-effect sensor. The Fourier transform plot of both signals, shown in Figure 5-54, presents peaks in excellent agreement to the fundamental frequency of the ZBD signal, while the reference signal shows additional harmonic peaks, expected as per its time domain waveform.

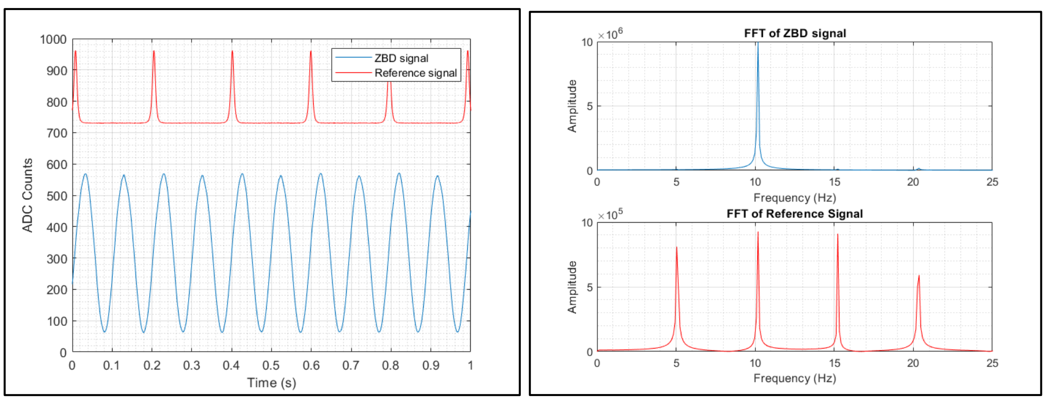

Figure 5-54. Extract of the ZBD and hall effect sensor timestreams as digitized by the Arduino (left) and their Fourier Transform (right).

The relative angle was measured 10 times with and without the grid to confirm the repeatability of the relative angle estimation. The average relative angle without the grid was 42.89° ± 0.05°, while the average relative angle with the grid was 43.23° ± 0.03°. The difference between the relative angle with the grid on and off then corresponds to 0.34° ±0.06°. This can be attributed to the mechanical alignment of the waveguide with respect to the grid, the latter which defines the actual polarization of the source and, thus, the relative angle.

This result allows us to conclude that the polarization angle of the RF source does not rely heavily on the polarizer as the waveguide already emits a highly linearly polarized signal. Given the small difference between the two relative angles, we could also presume that this may rather be an effect of imperfections in the mechanical frame and that the polarization of the waveguide is nearly identical to the one produced by the polarizer. Should this effect be produced by the misalignment between the polarizing grid and the waveguide, the transmitted versus reflected portion of the signal would correspond to loss of power of 0.59%; however, this effect is already accounted for in the results of experiments, as the power characterization was carried out with the polarizer grid. At the lowest emitted power of ~ (-4) dBm, for example, and considering the 2 cm FPL from the waveguide to the polarizer, this would imply a reflected wave with power no higher than -68 dBm.

- **Relative polarization angle maps**

The measurements show that the relative angle stays reasonably constant throughout the mapped region, as seen in Figure 5-55. The results are shown in 2D maps with and without the wire grid polarizer, as well as azimuth and elevation cuts, all normalized to the (0°, 0°) point (see Figures 5-56 and 5-57).

The grid-on results show maximum and minimum values of relative polarization angle of 1.09° and -0.84°, respectively. The map also shows a noticeable trend that is persistent both with and without the grid and that occurs mostly at negative angles of azimuth and elevation, shown in Figure 5-58.

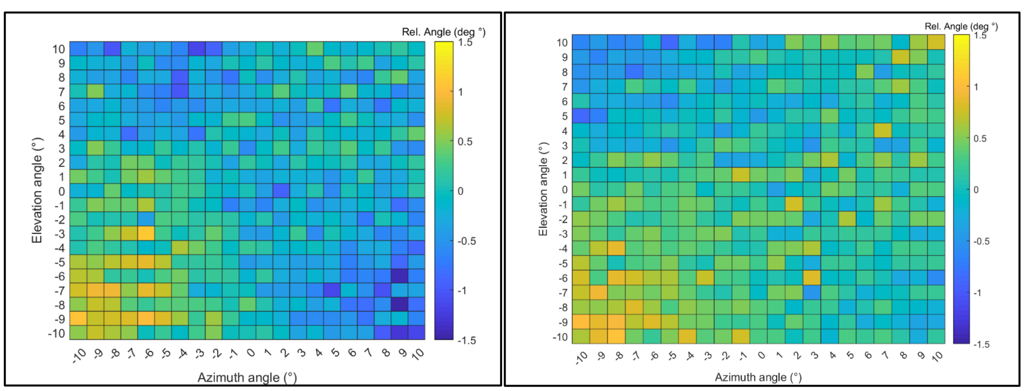

Figure 5-55. Mapped relative angle without the grid (left) and with the grid (right).

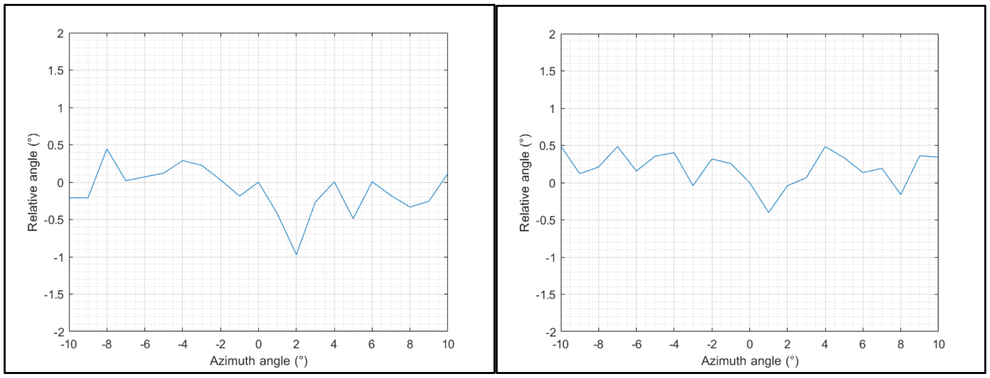

Figure 5-56. Relative angle azimuth cut without the grid (left) and with the grid (right).

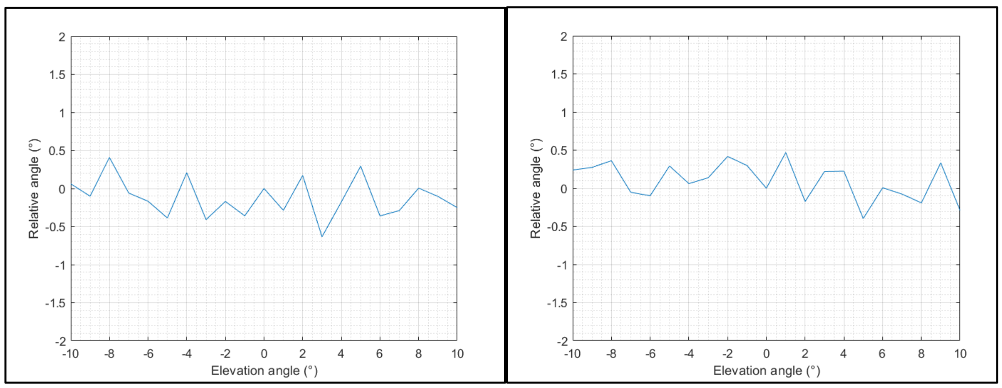

Figure 5-57. Relative angle elevation cut without the grid (left) and with the grid (right).

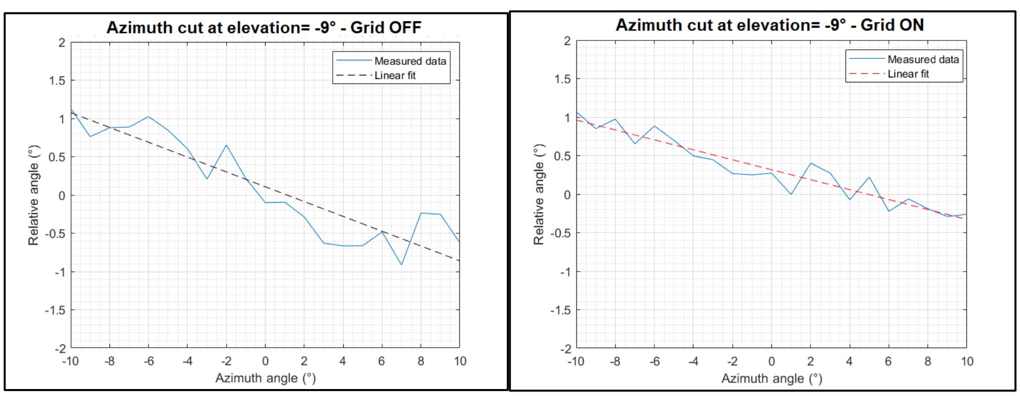

Figure 5-58. Relative angle trend at lower elevations without the grid (left) and with the grid (right).

Considering that the presence of standing waves was concluded by previous experiments and that the relative angle measured by the rotary polarimeter showed dependence on standing waves and reflections, further tests were carried out to determine whether the observed drifts were an actual characteristic of the source or were caused by the measurement setup. The description and results of some of the tests carried out are outlined below.

- Various configurations of RF absorbers: attempted to ensure most reflecting surfaces within the anechoic chamber were covered in Eccosorb, especially the exposed sections of the CNC robot. These changes resulted in a mapped pattern with a different distribution of peaks and dips overlayed on the trend seen earlier slightly diminished in amplitude.

- Eccosorb baffle: by adding an Eccosorb baffle around the rotary polarimeter, as seen in Figure 5-59, we attempted to minimize any large angle reflections coming from the chamber's floor and walls, induced by the large beam of the open waveguide. Detector line-of-sight standing waves produced by same-path reflections (such as the one observed when moving the ZBD linearly back and forth as in previous experiments) showed slight improvement under this configuration. The finer structures in the relative angle map varied slightly, but the overall trend stayed relatively constant.

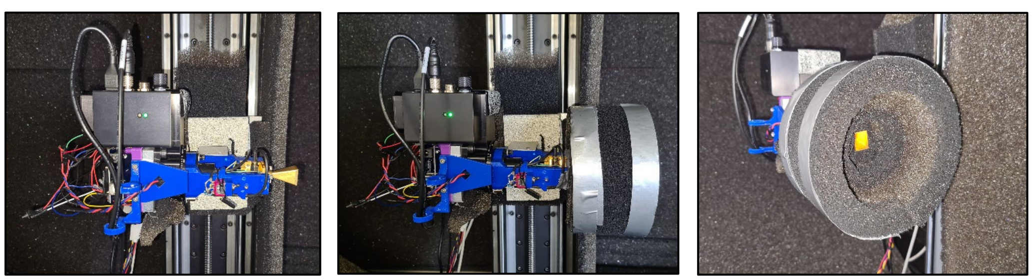

(a) (b) (c)

Figure 5-59. Rotary polarimeter (a) and Eccosorb covered setup (b & c).

- Rotation of the source: a special mount was 3D printed to rotate the RF source 90° counterclockwise around the X axis (see Figure 5-60), while ensuring the location of the waveguide remained constant. Under this condition, should the source produce the trend, it should not be observed in the same axis. Despite this change, the trend persisted in the same orientation as before, although with a different structure and amplitude, shown in Figure 5-61.

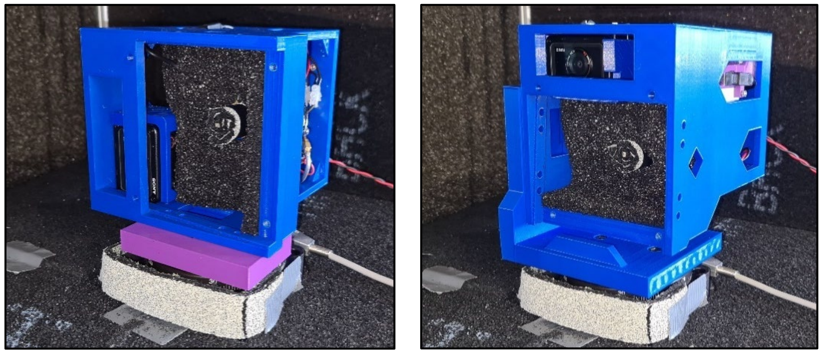

Figure 5-60. Illustration of the original configuration of the RF source (left) and 90° rotated RF source (right).

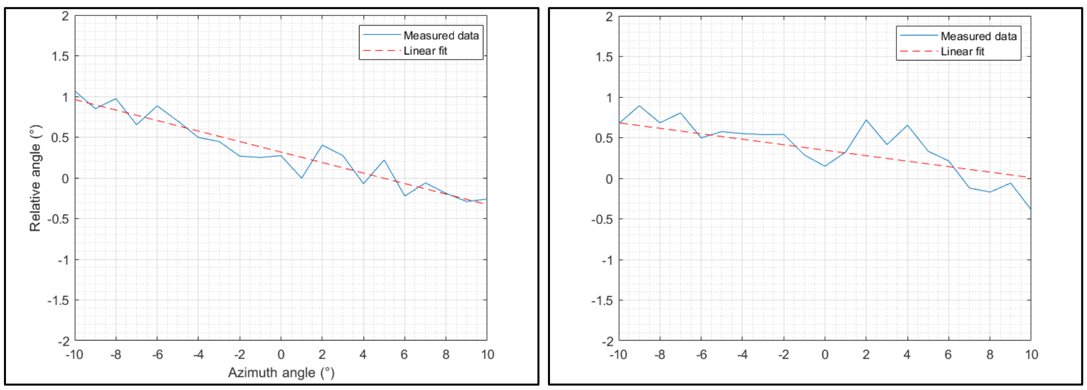

Figure 5-61. Azimuth cuts at elevation = -9°. Original (left) and with the rotated RF source (right).

- <u>Use of a different waveguide</u>: if the trend was an inherent effect of the open-ended waveguide, a different waveguide would not exhibit the exact same behavior. Despite this change, the trend remained unaltered.

- <u>Simulations of tilts of the Yaw actuator</u>: attempted to determine if a tilt of the Yaw actuator could produce the effects seen in the relative angle map. The simulations showed that a tilt of 15° should be capable of producing the observed trend, which would have been evident by simple observation. Moreover, if this had been the case, the trend should have been noticeable through most elevations, which is not the case. The setup for these simulations is shown in Figure 5-62.

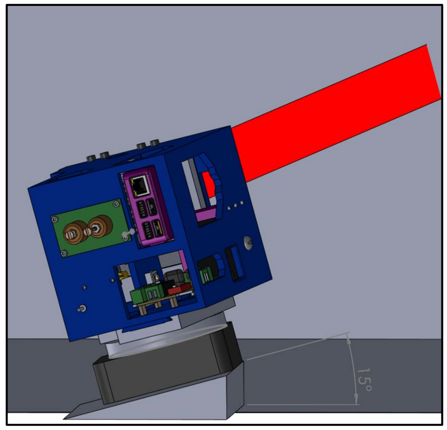

Figure 5-62. SolidWorks simulation of the frame's critical tilt angle.
The black structure is the yaw actuator, the red beam is the projection of the polarization angle of the waveguide on a surface at the same distance as the detector.

- Use of an alternate section of the rotation actuator: suspecting that precession of the rotation axis of the yaw actuator could induce the observed effects, the actuator was rotated 90° to ensure that a different section of the actuator was used. If a precessing rotation axis was the cause of the trend, using a different section of the actuator should produce a different behavior. Despite this change, the trend persisted unaltered.

- Different detector distances: by moving the ZBD away from the source in 0.2 mm steps, it was possible to observe the effects of standing waves in the pattern. The results showed that the measured relative angle changes as the standing waves amplitudes change.

- Different center frequencies: measurements with different center frequencies allowed us to effectively vary the standing waves without altering the geometric setup of the system. The results showed that the measured relative angles change in relation to the standing wave content, with a nonlinear correlation on the edges of the mapped pattern (see Figure 5-63).

From these tests, we can conclude that the trend observed in the data is an effect of the measurement system setup, most likely the effect of standing waves produced within the chamber or reflections rather than an actual effect of the source. Several results back this assumption, such as the fact that the trend seemed unaffected by rotation of the RF source, or tests at different frequencies, which show that the measured angle is heavily affected by standing waves if the source is pointed away from the center. While the latter effect is evident in the plots, this effect was found to be nonlinear and hard to model or filter.

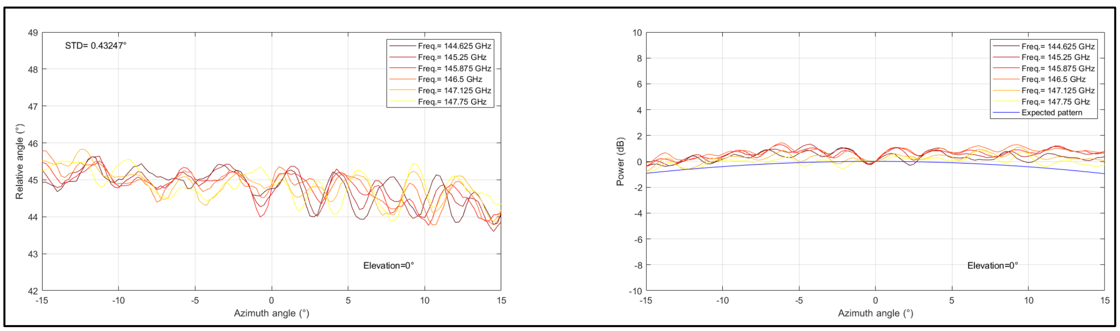

Figure 5-63. Overlayed azimuth cuts at different center frequencies for relative angle (left) and normalized power (right).

The asymmetry of the trend is seemingly related to the setup of the anechoic chamber, in which the Y actuator of the CNC robot is a cause of asymmetry in the horizontal direction, while the floor of the chamber is asymmetric in the vertical direction. A similar observation was made by Professor Edward Wollack (NASA Goddard Space Flight Center), experienced in RF characterization of antennas and receivers, after observing the measurement setup and reviewing the data.

While the span of measured relative angles is beyond the 0.1° target accuracy of the calibrator, the relative angle throughout the map was generally well behaved, without large variations across the characterized region. We can conclude that the standing-wave-produced effects should not be present on a calibrator flight due to the lack of elements capable of inducing standing waves or significant reflections, especially at distances such as the ones evaluated in this work.

The polarization angle of a source is not expected to change throughout its radiation pattern. Thus, we can conclude that the polarization angle of the source and calibrator should only be dependent on its rotation around the axis along the line of sight (boresight) of the telescope during calibration missions. The combination of the relative angle between the grid and the camera, as characterized in the laboratory before calibration missions, in combination with the photogrammetry assessment of the attitude of the source with respect to the telescope, should always be considered the main polarization angle reference and will be assumed isotropic by all accounts.

5.7. Radiation pattern characterization

5.7.1. Design of the radiation pattern characterization experiments

The goal of this experiment is to map the angular power response of the RF source. This information can serve to identify potential issues with the RF source and allow us to quantify the variation in received power during calibration procedures should the UAV-carried source vary its attitude with respect to the telescope in a significant manner.

The radiation pattern power was obtained from the Fourier domain fundamental frequency component power measured with the rotary polarimeter, which allows for a precise power estimation, rejecting effects such as noise in the amplifier and electronics or quantization noise in the DAC.

For these tests, the CNC robot remains in the same configuration seen in Figure 5-51, used for the relative polarization angle map. The radiation pattern will be mapped for elevation and azimuth angles between -10° and 10°, with 1° resolution.

5.7.2. Results of the radiation pattern characterization

The grid-off results, shown in Figure 5-64a, indicate that standing waves heavily affect the measured pattern, despite the use of several configurations of Eccosorb that were used try to mitigate this effect. The induced variation’s peak-to-peak span was measured at up to ∼1.5 dB. These waves can be seen more clearly in a tridimensional representation of the radiation pattern, shown in Figure 5-65, and in azimuth and elevation cuts, shown in Figure 5-66.

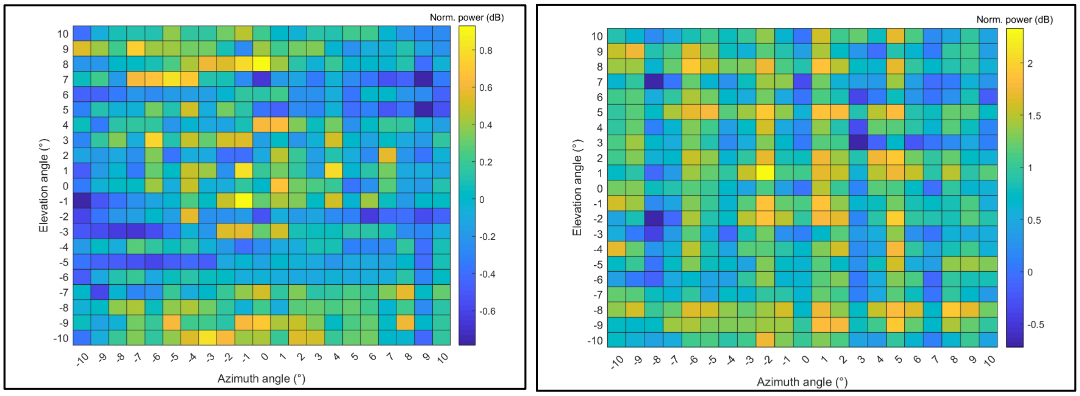

(a) (b)

Figure 5-64. Radiation pattern of the RF source without the polarizer (a) and with the polarizer (b), projected into a 10° x 10° flat grid.
The pattern is shown normalized to the (0°, 0°) point.

On closer inspection, the mapped pattern does appear to follow the expected behavior seen in the simulation. From these results, we shall consider that the waveguide's behavior follows closely its theoretical counterpart and that its beamwidth without the grid is approximately 47.2°, as is the case with the simulated waveguide.

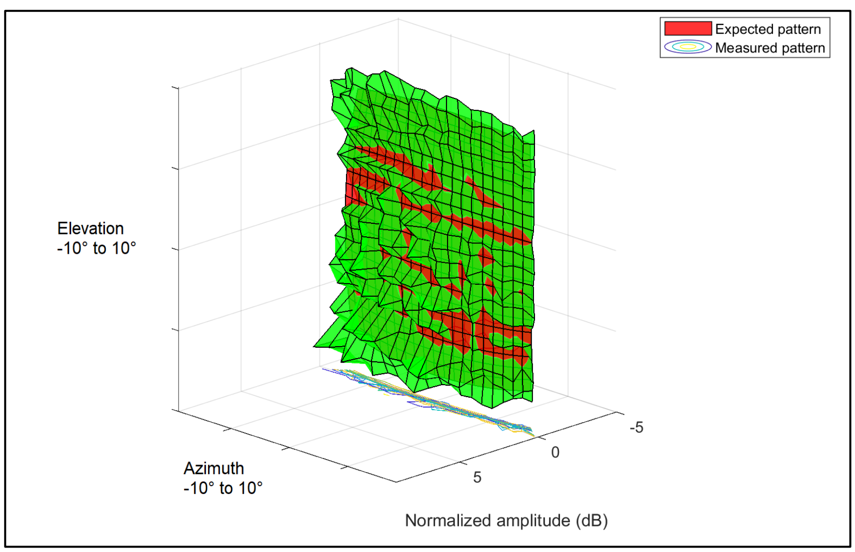

Figure 5-65. Tridimensional representation of the RF source power pattern without the polarizer.
Notice that several points seem to lie on the surface of the expected pattern.

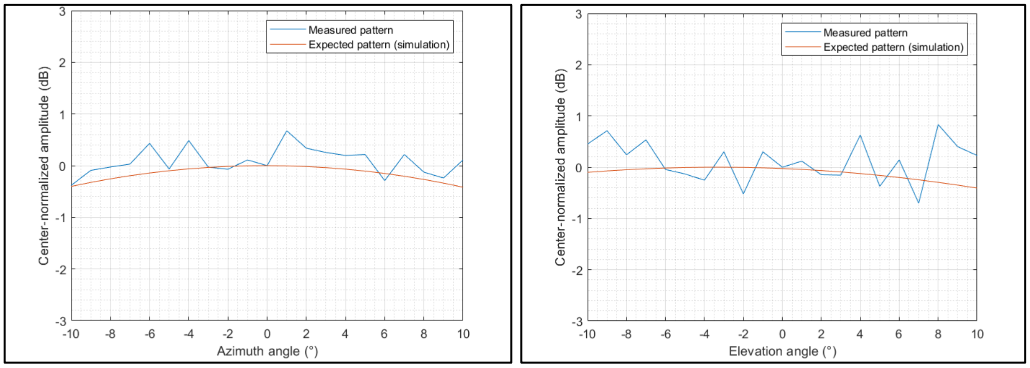

Figure 5-66. **A**zimuth cut at elevation=0° (left) and elevation cut at azimuth=0° (right) without the polarizer.

The results with the wire grid polarizer also show that standing waves dominate the pattern, seen in Figure 5-64b. The large metal frame of the wire grid, covered in Eccosorb for this test, apparently amplifies the effects seen in the grid off measurements, especially on the central section of the pattern, which shows much larger standing waves than before. The amplitude of the standing waves at the edges remains mostly consistent with the previous experiment.

As in the previous case, the grid-on azimuth and elevation cuts mostly align to the expected pattern, with an array of waves overlayed on top of it, most noticeable in the 3D pattern and residual plots of Figure 5-67 and Figure 5-69, respectively.

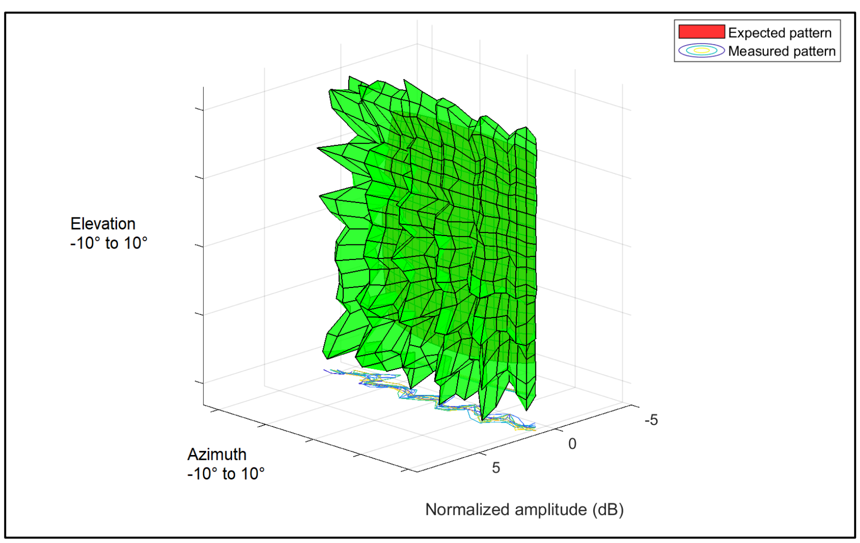

Figure 5-67. Tridimensional representation of the RF source power pattern with the polarizer. The standing waves content becomes more prominent than without the polarizer, but still seem to be overlayed on top of the expected pattern.

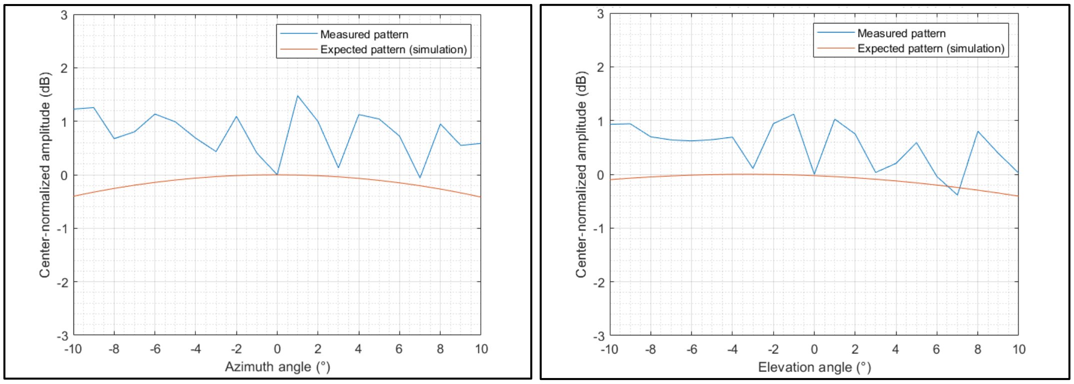

Figure 5-68. Azimuth cut at elevation=0° (left) and elevation cut at azimuth=0° (right) with the polarizer. Notice that the pattern of waves changes as we point the source towards the Y actuator (negative azimuth) or when the reception hardware is closer to the anechoic chamber floor (negative elevations), which resembles the effects seen in the relative polarization angle maps.

The most evident difference from the grid-off result lies in the central section, and between -10° and -5° of each cut, both showing larger oscillations. The sustained larger amplitudes on these sections can be explained by the inclusion of the polarizer, which may generate larger reflections on asymmetric elements: the robot's y-axis actuator, for the effects seen at negative azimuth angles; and the metallic surface of the optical table, which is closer to the source than the anechoic chamber ceiling, for those seen at negative elevation angles.

The main takeaway from these results is that the measured pattern seems to be largely consistent with the simulated one, with other effects seemingly overlayed on the base response of the source. While characterizing the exact sources of the standing waves within a given anechoic chamber setup has been carried out successfully, as seen in the literature (Togawa, Hatakeyama, & Yamauchi, 2005; Eimer J. , Bennett, Chuss, & Wollack, 2011), it would require far more complex measuring setups and specialized equipment —e.g. a Vector Analyzer— to obtain reliable results. Due to the nature of the expected telescope calibration setup, with large distances between the telescope and the RF source, as well as structures specifically designed to minimize reflections incorporated the telescope's structure, it can be assumed that the systematic effects seen in these measurements should not affect the final performance of the RF source during calibrations.

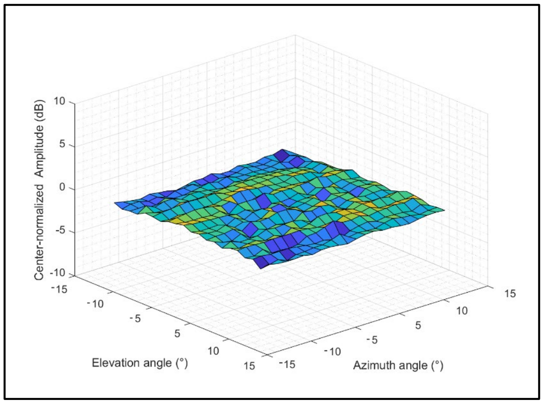

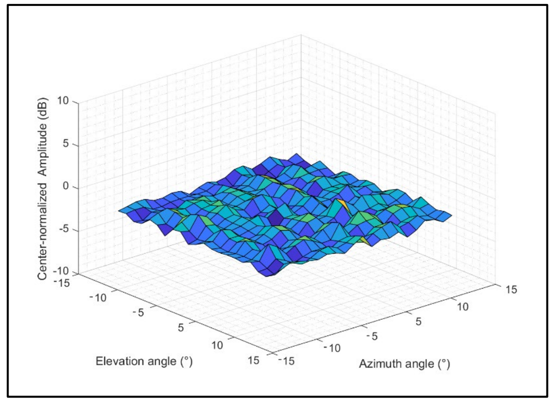

Figure 5-69. 3D residuals between the expected and measured pattern without the grid (left) and with the grid (right). The grid-on result shows very clear oscillations that must correspond to standing waves.

5.8. Relative angle of the wire grid polarizer

5.8.1. Design of the polarizer relative angle determination method

The goal of this experiment is to obtain a reliable method for obtaining the wire grid relative angle with respect to the metrology camera, which sets an absolute coordinate system for the calibrator. This calibration needs to be performed every time the camera and grid are assembled into their final positions in the frame.

The devised method relies in shinning a laser placed orthogonal to the wire grid and then analyze the diffraction pattern, which forms a plane perpendicular to the direction of the wires, or parallel to the polarization angle of the grid. As we rely on the mechanical setup of both elements, the pattern is affected by the manufacturing quality of the laser module, the accuracy and deformations of the 3D printed frame and final assembly of the components, all of which are assumed to produce a far greater effect than that produced by the wire grid's manufacturing quality. The observed diffraction pattern is predominantly linear, with subtle higher order effects that appear to be produced mainly by the vertical and horizontal misalignments between the laser and the grid, shown in Figure 5-70.

To obtain the relative angle, the diffraction pattern was projected onto a flat surface placed parallel to the source and 12-megapixel images are captured with the digital camera mounted inside the frame in its final position. The image is processed to smooth out noise in the edges of the laser trace and then binarized to obtain pixels corresponding to the diffraction pattern.

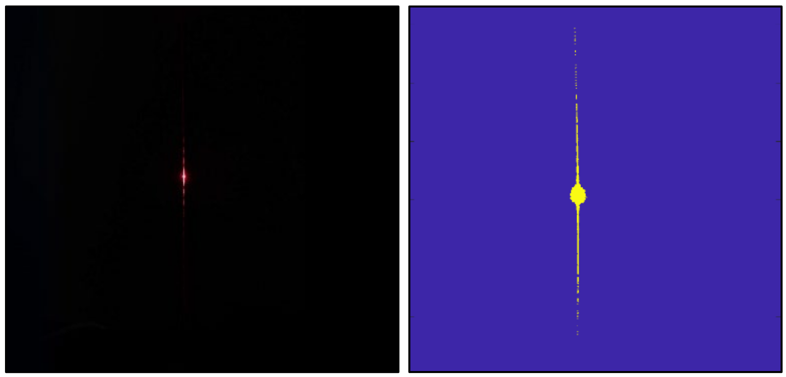

Figure 5-70. Original image of the diffraction pattern (left) and processed image (right).

With the binarized image, the centroids of each row in the image are calculated. The central section surrounding the zero-order mode location is then removed from the set to minimize the error induced by glow. A minimization script then fits a quadratic curve to all remaining points and sets the location of the zero-order mode within this curve. The relative angle between the zero-order location and each point in the curve is calculated and then a differential relative angle is recalculated by subtracting the angles of each pair of points at an equal radial distance from the zero-order location. By using differential measurements, it is possible to effectively neglect the higher-order effects seen in the pattern and obtain a more reliable estimation of the relative angle of the grid. Finally, the minimization script obtains the differential angle dispersion with the standard deviation and iteratively adjusts the zero-order mode location until the dispersion has been minimized. This procedure is summarized in the flowchart shown in Figure 5-71.

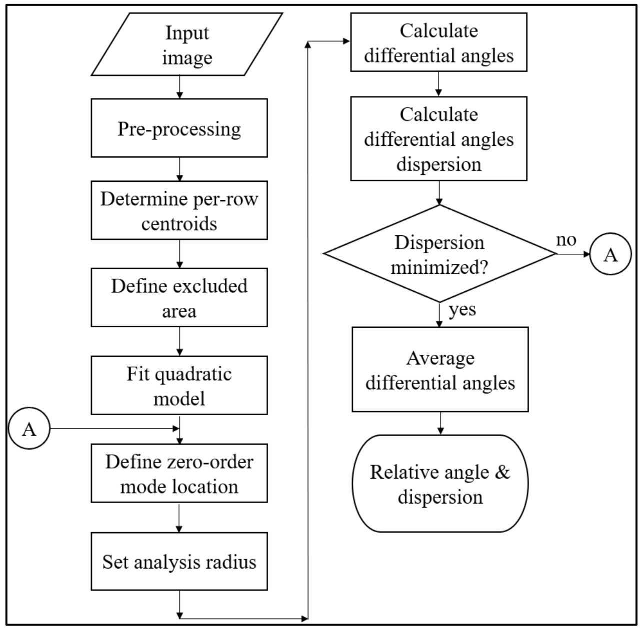

Figure 5-71. Flowchart of the algorithm to determine the relative angle of the polarizer.

5.8.2. Results of the polarizer relative angle determination

To test the grid-to-camera relative angle determination algorithm, two 5-picture sets were analyzed. The first set was taken with the camera and polarizer setup already assembled and fixed in place, while the second one was taken after disassembling the setup and then reassembling it. The results are shown in Table 7, where the developed method is compared to a linear fit of the binarized laser trace.

Table 7. Relative angle of the wire grid with respect to the metrology camera

	Set 1		**Set 2**	
Image	**Pixel-pair differential relative angle (°)**	**Linear Fit (°)**	**Pixel-pair differential relative angle (°)**	**Linear Fit (°)**
1	0.458	0.392	0.473	0.414
2	0.438	0.482	0.468	0.472
3	0.438	0.471	0.471	0.427
4	0.441	0.445	0.484	0.472
5	0.46	0.46	0.476	0.463
Mean:	0.447	0.450	0.474	0.450
SD:	0.011	0.035	0.006	0.027

The results of the relative angle determination are consistent with the mean and dispersion shown in previous work, based on a similar method, performed on an earlier version of the support frame, and carried out with a laser manually aligned to the grid (Dünner, Fluxá, Best, Carrero, & Boettger, 2021).

The method developed for this work does show better performance compared to a linear fit, obtaining a lower dispersion and, thus, a more reliable estimate of the wire grid relative angle. Nevertheless, the mean of both methods shows a reasonable agreement, which indicates that the higher order effects do not heavily influence the results.

On Set 2, the linear fit seems to mostly replicate its results from Set 1, however, it is unlikely that the relative angle stayed perfectly constant despite reassembling the setup. The current method shows a slight variation in the relative angle, which may indicate that it captured the finer differences produced by reassembling the setup. This, in combination to the linear fit result's much wider dispersion, should serve as an indication that the method developed in this work is a more reliable alternative to determine the relative angle. Moreover, the Set 2 mean result from our method is within uncertainty of the linear fit's measurements, which serves as an additional validation.

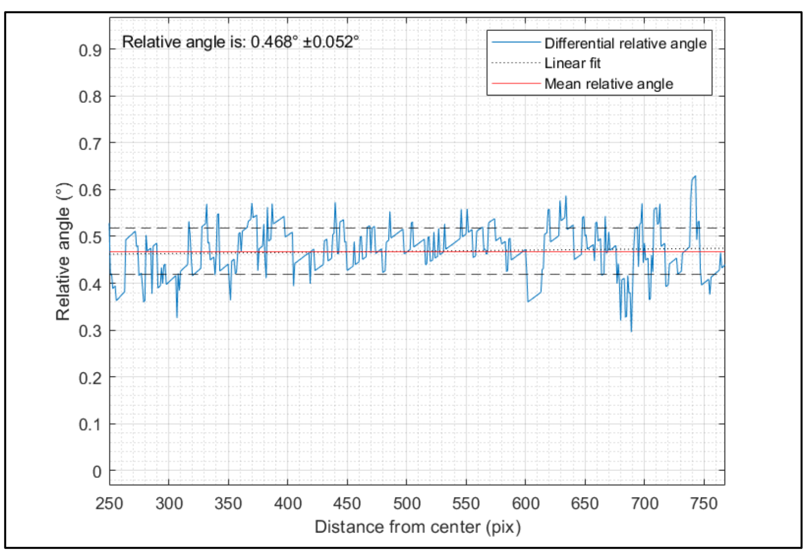

Figure 5-72. Plot of the pixel pair differential relative angle as a function of distance.

Figure 5-72 shows the plot of differential angles versus radial distance for one of the images, which suggests that the dependance of the relative angle with distance is low, as well as the per pixel-pair angle dispersion, even at larger radial distances.

The results of the relative angle characterization show that it is possible to determine the relative orientation of the grid with respect to the metrology camera with great precision. Moreover, the uncertainties shown in the results, obtained either from the per-image pixel-pair relative angle plot or from the photo sets, satisfy the accuracy requirement set as a goal for the UAV-based calibrator. The ideal scenario for this measurement would be to align the grid, camera, and laser perfectly, which would minimize all higher-order effects and ensure that the relative angle is determined with maximum certainty. In future work, more effort could be placed into fine-tuning the alignment of the elements, with the alignment between the grid and the laser being the most likely source of nonlinear effects that translates into larger inaccuracies.

5.9. Test flight of the integrated RF source

A test flight of the source was conducted at PUC campus while measuring power with the spectral analyzer connected to the frequency extender, the latter angled at elevation of ~45°. Coded targets were placed in the vicinity of the frequency extender to simulate the expected setup when performing telescope calibrations and the gimbal was aligned to the extender pointing angle. The unattenuated RF source was mounted on the gimbal and the camera was set to record while connected to the aircraft's HDMI port to simultaneously transmit the video feed to its remote control. The source's RF multiplier was set to modulate the output signal with a square wave at 1 Hz, generated by the Raspberry Pi microcontroller to test the digital chopping system. This will be used in actual telescope calibration procedures to improve signal recovery in presence of noise by chopping the signal at frequencies in the order of kilohertz.

Figure 5-73. UAV-carried RF source pointed at the frequency extender during test flight.

The aircraft was able to take off successfully while carrying the source, the latter powered from the gimbal. The source was flown at different altitudes while pointed at the reception setup and data was recorded. During this test, the drone showed very stable hovering and no signs of strain or abnormal behavior. The gimbal also performed appropriately, absorbing any abrupt movements when the aircraft was relocated.

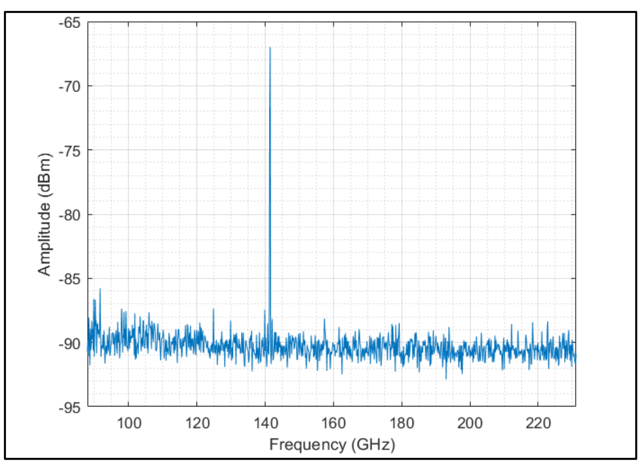

Figure 5-74. Trace of the spectrum retrieved from the spectral analyzer during the test flight.

The retrieved data from the spectral analyzer shows a narrow line at 141.3 GHz, the programmed frequency of the source for this experiment, with signal to noise greater than 20 dB at shorter distances. The signal was observed flickering on and off at a rate of 1 Hz, consistent with the digital signal chopper's frequency.

Afterwards, the aircraft was moved iteratively to higher altitudes while pointed at the source. The experiment was stopped when a signal-to-noise ratio of ~8 dB was observed, with displayed average noise floor of -90.3 dBm. From the full trace of the drone's sensors, the maximum measured altitude was 35.14 meters, which, at a 45° angle, translates to 49.7 meters from the reception hardware.

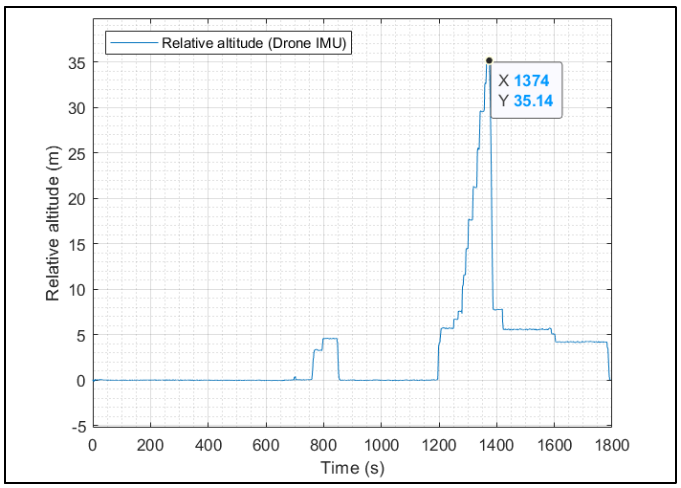

Figure 5-75. Relative altitude trace from the drone's Inertial Measurement Unit (IMU).

For 141.3 GHz and 49.7 meters, the free space propagation loss amounts to 109.4 dB. The emitted power of the source can be calculated and compared to the characterized power curve by incorporating into Equation 5.7 the factor that corresponds to removing the multiplier's attenuation A_{tx}, measured at 23 dB, which results in

$$P_{source} = P_{meas.} + 3\ dB + L_{rx}{}^{9} - 22\ dB - A_{tx} + FPL\ , \qquad \text{(Eq. 5.16)}$$

$$P_{source} = P_{meas.} + 3\ dB + 10.3\ dB - 22\ dB - 23\ dB + 109.4\ dB\ , \quad \text{(Eq. 5.17)}$$

which results in an estimated emitted power of -4.6 dBm. From the band power

[9] Frequency extender intrinsic mixer loss at 141.3 GHz

characterization curve, the emitted power at 141.3 GHz corresponds to 0.5 dBm, which shows a difference of 5.1 dBm. The most likely cause of the observed difference is inaccurate alignment between the emitter and receiver antennas, which was performed manually and becomes harder as distance increases. Nevertheless, this is still a satisfactory result, considering the test conditions and underlying assumptions.

Finally, a photogrammetry reconstruction of the test site was conducted to ensure the metrology system performed appropriately during flight, shown in Figure 5-76. An estimate of altitude versus time was also calculated with sequential frames extracted from a 30-second video clip of the metrology camera, shown in Figure 5-78. The reconstruction results show an appropriate correspondence to the aircraft's sensors, with percentual errors between -2% to 2%, except for the section in which the drone's altitude is changed rapidly, where the plots diverge more noticeably.

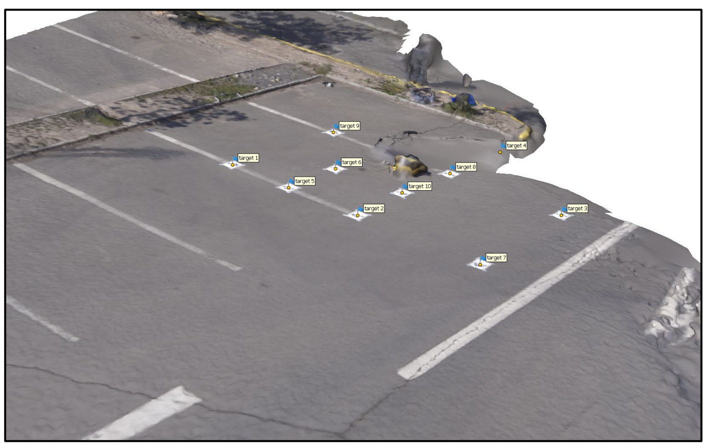

Figure 5-76. 3D Photogrammetry reconstruction of the test site obtained with Metashape.

The test flight allowed us to confirm that the integration of the source with the gimbal and drone was carried out successfully. The photogrammetry reconstruction of the test site as well as the estimated position of the drone from the photogrammetry data showed satisfactory results, which confirms that all the calibrator's systems are operating as expected during flight. The maximum transmission distance for this setup while maintaining a good signal-to-noise ratio was approximately 49.7 meters and the emitted power is in reasonable agreement with the values measured during characterization, which validates both the test flight and the characterization processes.

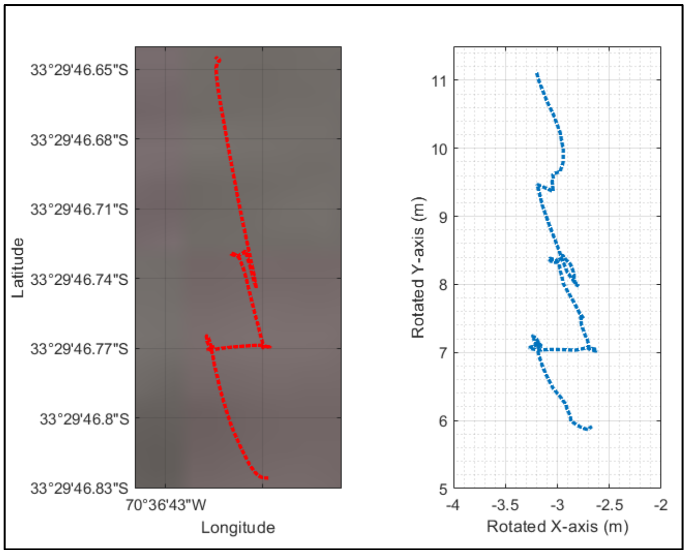

Figure 5-77. Trace of the drone's path from the RTK-GPS overlayed on a map (left) and matched reconstruction with photogrammetry from the 30-second video clip (right).
The RTK-GPS map plot has been scaled so that each major tick on the axes represents ~1 meter.

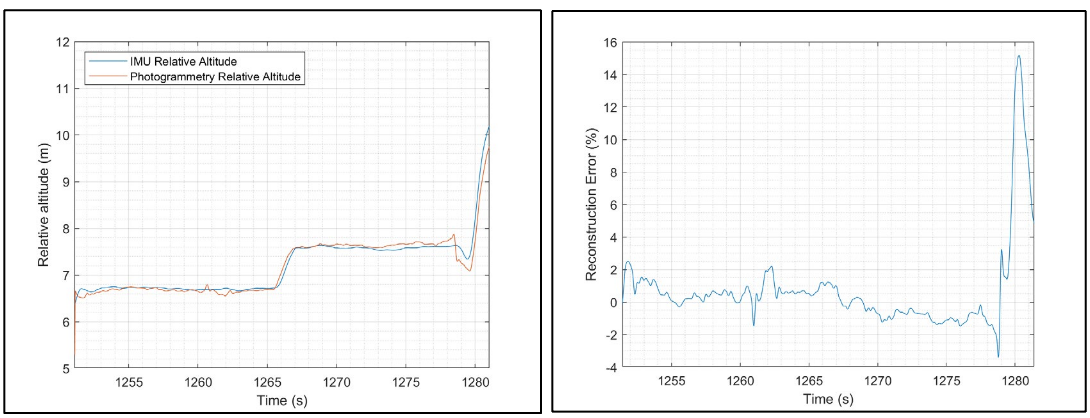

Figure 5-78. IMU vs. photogrammetry measured altitude (left) and percentual reconstruction error (right).

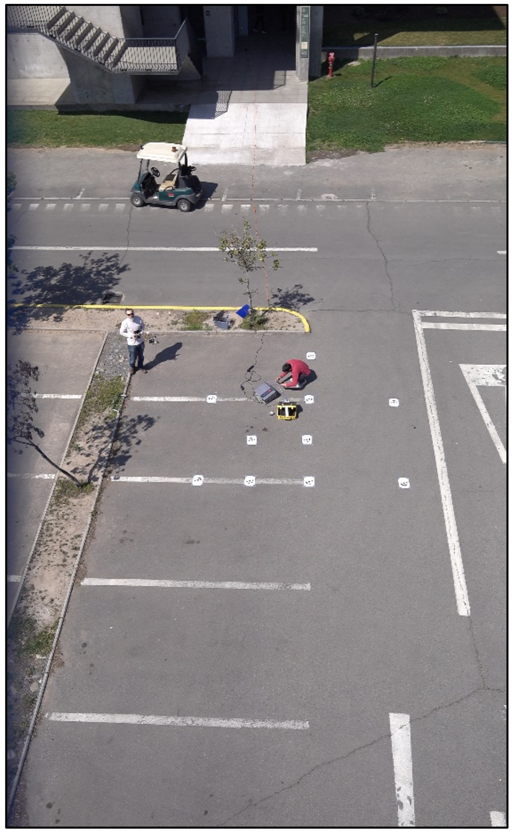

Figure 5-79. View from the source's metrology camera during the test flight.

6. CONCLUSIONS

A first order estimation of the uncertainty in the most important parameter of the UAV-based calibrator, the polarization angle α, can be obtained as the combination of uncertainties from the following sources: the mechanical frame's thermal deformations, the photogrammetry determination of the drone's attitude with respect to the telescope from the metrology camera's flight footage, and the calibration of the relative angle between the camera and the grid. For the photogrammetry analysis uncertainty, we will consider that its upper bound is of the same order as the largest angular uncertainty obtained when characterizing the CNC robot with photogrammetry and OpenCV. For the relative angle between the polarizer and the grid, we will use the largest uncertainty, which was found in the per pixel-pair relative angle dispersions of each image, with an image set average of 0.06°.

By assuming that the phenomena listed earlier are not correlated, we can obtain an approximation of the polarization angle accuracy as the quadrature sum of the individual uncertainties calculated on each experiment

$$\sigma_\alpha = \sqrt{\sigma_{thermal}^2 + \sigma_{photogram.}^2 + \sigma_{calib.}^2} \quad , \qquad \text{(Eq. 6.1)}$$

and by replacing the values obtained from the experiments into Equation 6.1, we obtain the following:

$$\sigma_\alpha = \sqrt{0.02^2 + 0.04^2 + 0.06^2} = \pm 0.07° \qquad \text{(Eq. 6.2)}$$

The result of Equation 6.2 is within the calibrator's target accuracy of ±0.1°, from which we can conclude that the UAV-based calibrator for CMB telescopes should perform optimally with the current design.

The most important results obtained from the characterization experiments of the RF source are summarized in Table 8.

Table 8. Summarized results of the RF source characterization

Parameter	**Result**	**Observations**
Emitted power:	5.36 to -3.65 dBm	Corresponds to the multiplier's lowest attenuation, with a 10 dB passive attenuator at the multiplier's input.
Power stability:	0.106 dB / 2.5%	Corresponds to the average power dispersion throughout the frequency band of operation.
Avg. freq. stability:	0.1 ppm (< 1% CLASS BW_{150GHz})	Corresponds to the largest measured uncertainty within the band of operation of the UAV-based calibrator.
Expected -3dB beamwidth:	47.2°	Experiments allowed us to conclude that the source should closely resemble the simulated pattern. Thus, the listed beamwidth corresponds to the one obtained from the simulation.
Relative polarization angle vs. direction:	1.09° to -0.84°	Measured maximum and minimum values throughout σ and ϕ between -10° and 10°, and referred to the polarization angle at (0°, 0°). In the open, the polarization angle should be highly isotropic.
Source polarization angle uncertainty:	0.07°	First-order estimation based on the results of this work.
Total weight:	1096 g	

The characterization experiments allowed us to conclude that the current design of the UAV-based calibrator can achieve the required polarization angle accuracy and is a viable alternative to polarization angle calibration of CMB experiments. The RF source has achieved suitable levels of performance:

- The mechanical support structure was designed and implemented within the rigidity, volume and weight constrains. The integrated RF source has been shown to be below the initial 2 kg technical requirement.
- The photogrammetry-based metrology system's upper bound of accuracy has been shown to be better than 0.1°.
- The emitted power of the RF source has been demonstrated to be within power limit specifications of the CLASS telescope, albeit at the limits of the RF source's hardware.
- The RF source power has been shown to be stable within 4%.
- The RF source frequency stability has been shown to be well below 1% of the bandwidth of typical CMB telescopes and the frequency-shift-induced power variations have been determined to be negligible.
- The overall expected accuracy of the UAV-based calibrator has been shown to be within 0.1°.
- The UAV-based calibrator's systems have shown excellent results during a test flight.

Finally, we can conclude that the objectives set at the beginning of this thesis have been achieved successfully and the result is a UAV-based calibrator that has been characterized in the laboratory.

With the work carried out in this thesis, a solid framework has been laid for future work in this project, such as performing test flights with the source at CMB high sites, developing the actual methods for analyzing photogrammetry data during calibration tests, and designing flight plans and data reduction schemes for each calibration mission.

REFERENCES

Abitbol, M. H., Alonso, D., Simon, S. M., Lashner, J., Crowley, K. T., Ali, A. M., . . . Coppi, G. (2020, November). *The Simons Observatory: Bandpass and polarization-angle calibration requirements for B-mode searches*. Retrieved from arXiv.org (Journal of Cosmology and Astroparticle Physics [JCAP] Preprint).

Aghanim, N., Akrami, Y., Arroja, F., Ashdown, M., Aumont, J., Baccigalupi, C., . . . Zonca, A. (2020). Planck 2018 results. *Astronomy and Astrophysics, Volume 641*.

Analog Devices. (2021). *Analog Devices Technical Documentation - Datasheet - ADF5355.* Retrieved from Analog.com: https://www.analog.com/media/en/technical-documentation/data-sheets/ADF5355.pdf

Appel, J. W., Xu, Z., Padilla, I. L., Harrington, K., Pradenas Marquez, B., Ali, A., . . . Zeng, L. (2019). On-sky performance of the CLASS Q-Band Telescope. *The Astrophysical Journal, Vol. 876, Issue 2*.

Aumont, J., Ritacco, A., Macías-Pérez, J. F., Ponthieu, N., & Mangilli, A. (2020). Absolute calibration of the polarisation angle for future CMB B-mode experiments from current and future measurements of the Crab Nebula. *mm Universe @ NIKA2.* Grenoble.

Balbi, A. (2000). Cosmological Parameter Estimation from CMB Experiments. *Cosmology and Particple Physics, Proc. of the CAPP 2000 Conference.* Verbier.

Burke, B. F., Graham-Smith, F., & Wilkinson, P. N. (2019). *An Introduction to Radio Astronomy (Fourth Edition).* Cambridge University Press.

Carmeli, M., Harnett, J. G., & Oliveira, F. J. (2005). The Cosmic Time in Terms of the Redshift. *Foundations of Physics Letters, vol. 19, issue 3*, pp. 277-283.

Condon, J. J., & Ransom, S. M. (2016). *Essential Radio Astronomy.* Princeton University Press.

Condon, J. J., & Ransom, S. M. (2018). Retrieved from National Radio Astronomy Observatory - Essential Radio Astronomy: https://www.cv.nrao.edu/~sransom/web/xxx.html

Dahal, S., Appel, J., Datta, R., Brewer, M., Ali, A., Bennet, C., . . . Xu, Z. (2021). *Four-year Cosmology Large Angular Scale Surveyor (CLASS) Observations: On-sky Receiver Performance at 40, 90, 150, and 220 GHz Frequency Bands*. Retrieved from www.arxiv.org: https://arxiv.org/abs/2107.08022

Dhawan, S., Jha, S. W., & Leibundgut, B. (2018). Measuring the Hubble constant with Type Ia supernovae as near-infrared standard candles. *Astronomy and Astrophysics, Volume 609*.

DJI. (2021). *Matrice 600 Pro Specifications.* Retrieved from dji.com: https://www.dji.com/matrice600-pro/info#specs

DJI. (2021). *Ronin MX Specifications.* Retrieved from dji.com: https://www.dji.com/ronin-mx

Dodelson, S., & Schmidt, F. (2020). *Modern Cosmology.* Elsevier Academic Press.

Dünner, R., Fluxá, J., Best, S., & Carrero, F. (2020). Millimeter-wave polarization angle calibration using UAV-based sources. *SPIE Proceedings Volume 11453, Millimeter, Submillimeter, and Far-Infrared Detectors and Instrumentation for astronomy X.* [Online].

Dünner, R., Fluxá, J., Best, S., Carrero, F., & Boettger, D. (2021). Drone-based polarization calibration source for mm-wave telescopes. *2021 15th European Conference on Antennas and Propagation (EuCAP).* Dusseldorf.

Durrer, R. (2008). *The Cosmic Microwave Background.* Cambridge University Press.

Eimer, J., Bennett, C. L., Chuss, D. T., Marriage, T., Wollack, E. J., & Zeng, L. (2012). The Cosmology Large Angular Scale Surveyor (CLASS): 40 GHz optical design. *Proc. SPIE 8452, Millimeter, Submillimeter, and Far-Infrared Detectors and Instrumentation for Astronomy VI, 845220.* San Diego.

Eimer, J., Bennett, C., Chuss, D., & Wollack, E. (2011). Vector Reflectometry in a Beam Waveguide. *Review of Scientific Instruments, vol. 82,*, p. 086101.

Encyclopaedia Britannica. (2021). *Cosmology.*

Fixsen, D. (2009). The Temperature of the Cosmic Microwave Background. *The Astrophysical Journal, Volume 707, Issue 2*, pp. 916-902.

Gallardo, P. A., Cothard, N. F., Puddu, R., Dünner, R., Koopman, B. J., Niemack, M. D., . . . Wollack, E. J. (2018). Far Sidelobes from Baffles and Telescope Support Structures in the Atacama Cosmology Telescope. *SPIE Astronomical Telescopes & Instrumentation 2018.* Berlin.

García-Fernández, M., Álvarez López, Y., Arboleya, A., González-Valdés, B., Rodríguez-Vaqueiro, Y., De Cos Gómez, M. E., & Las-Heras Andrés, F. (2017). Antenna Diagnostics and Characterization Using Unmanned Aerial Vehicles. *IEEE Access, Vol. 5*, pp 23563-23575.

Gary, D. (2019). *Radio Astronomy: Lecture #5, New Jersey Institute of Technology.* Retrieved from https://web.njit.edu/~gary/728/Lecture5.html

Grain, J., Tristram, M., & Stompor, R. (2012). CMB EB and TB cross-spectrum estimation via pseudospectrum techniques. *Physical Review D, vol. 86, Issue 7.*

Gullberg, S. R. (2020). *Astronomy of the Inca Empire.*

Heidari-Rarani, M., Rafiee-Afarani, M., & Zahedi, A. M. (2019). Mechanical characterization of FDM 3D printing of continuous carbon fiber reinforced PLA composites. *Composites Part B: Engineering, Vol. 175*.

Hinshaw, G., Larson, D., Komatsu, E., Spergel, D. N., Bennett, C. L., Dunkley, J., & al, e. (2013). Nine-year Wilkinson Microwave Anisotropy Probe (WMAP) Observations: Cosmological Parameter Results. *The Astrophysical Journal Supplement Series, Volume 208, Number 2*.

Huffenberger, K. M., Araujo, D., Bischoff, C., Buder, I., Chinone, Y. C., Kusaka, A., . . . Newburgh, L. B. (2015). The Q/U Imaging Experiment: Polarization Measurements of Radio Sources at 43 and 95 GHz. *The Astrophysical Journal, Vol. 768, N°2*.

Issaoun, S., Folkers, T. W., Blackburn, L., Marrone, D. P., Kirchbaum, T., Janssen, M., . . . Falcke, H. (2017, September). *A conceptual overview of single-dish absolute amplitude calibration.* Retrieved from Event Horizon Telescope Memo Series: https://eventhorizontelescope.org/files/eht/files/EHT_memo_Issaoun_2017-CE-02.pdf

ITU. (2013). *Handbook on Radio Astronomy (Third Edition).* Radiocommunication Bureau.

Johnson, B. R., Vourch, C. J., Drysdale, T. D., Kalman, A., Fujikawa, S., Keating, B., & Kauf, J. (2015). A CubeSat for Calibrating Ground-Based and Sub-Orbital Millimeter-Wavel Polarimeters. *Journal of Astronomical Instrumentation, Vol. 4, Nos. 3 & 4*.

Kamionkowski, M., & Kovetz, E. D. (2016). The Quest for B Modes from Inflationary Gravitational Waves. *Annual Reviews, Volume 54*, pp 227-269.

Keating, B. G., Shimon, M., & Yadav, A. P. (2012). Self-calibration of Cosmic Microwave Background Polarization Experiments. *The Astrophysical Journal Letters, Vol. 762, N°2*.

Keysight Technologies. (2021). *N9020B MXA X-Series Signal Analyzer, Multi-touch.* Retrieved from www.keysight.com: https://www.keysight.com/zz/en/assets/7018-05048/data-sheets/5992-1255.pdf

Liddle, J. D., Holt, A. P., Jason, S. J., O'Donnell, K. A., & Stevens, E. J. (2020). Space science with CubeSats and nanosatellites. *Nature Astronomy 4*, 1026-1030.

Marcelino, N. (2016). *Observational methods in radio astronomy I: Single-Dish.* Retrieved from Instituto Nacional de astrofísica, óptica y electrónica (INAOE) - México: https://www.inaoep.mx/~progharo/gh2016/presentaciones/NM_metodosObsI.pdf

Martínez Picar, A., Marqué, C., Anciaux, M., Lamy, H., & Ranvier, S. (2015). Antenna pattern calibration of radio telescopes using UAV-based device. *2015 International Conference on Electromagnetics in Advanced Applications (ICEAA)*. Torino.

Milton, K. A., & Schwinger, J. (2006). *Electromagnetic Radiation: Variational Methods, Waveguides and Accelerators.* Springer.

Minami, Y., & Komatsu, E. (2020). New Extraction of the Cosmic Birefringencefrom the Planck 2018 Polarization Data. *Physical Review Letters, 125, 221301*.

Mini-Circuits. (2021). *ZX60-24A-S Amplifier Specifications.* Retrieved from minicircuits.com: https://www.minicircuits.com/pdfs/ZX60-24A-S+.pdf

Morison, I. (2008). *Introduction to Astronomy and Cosmology.* Wiley.

Nati, F., Devlin, M. J., Gerbino, M., Johnson, B. R., Keating, B. P., & Teply, G. (2018). Airborne, Far-Field Calibrators for Comic Microwave Background Telescopes: POLOCALC. *2018 IEEE Conference on Antenna Measurements and Applications (CAMA).* Stockholm.

Navaroli, M. F., Teply, G. P., Crowley, K. D., Kaufman, J. P., Galitzki, N. B., Arnold, K. S., & Keating, B. G. (2018). Design and characterization of a ground-based absolute polarization calibrator for use with polarization sensitive CMB experiments. *SPIE Proceedings Volume 10708, Millimeter, Submillimeter, and Far-Infrared Detectors and Instrumentation for Astronomy IX.* Austin.

O'Neil, K. (2001). Single Dish Calibration Techniques at Radio Wavelengths. *The NAIC/NRAO School on Single Dish Radio Astronomy.* Arecibo.

Paonessa, F., Virone, G., Bolli, P., & Addamo, G. (2018). Improvement of the Test Source Frequency Behavior. *2018 IEEE Conference on Antenna Measurements and Applications (CAMA).* Stockholm.

Pogosian, L., & Zucca, A. (2018). Searching for Primordial Magnetic Fields with CMB B-modes. *Classical and Quantum Gravity, Volume 35, Number 12*.

Raspberry Pi Foundation. (2021). *Raspberry Pi 3 B Specifications.* Retrieved from raspberrypi.org: https://raspberrypi.cl/producto/raspberry-pi-3-modelo-b/

Robishaw, T., & Heiles, C. (2019). *The WSPC Handbook of Astronomical Instrumentation, Volume 1, Radio Astronomical Instrumentation: Radio Telescopes.* World Scientific.

Smoot, G. F. (1999). COBE observations and results. *AIP Conference Proceedings, Volume 476*, (pp. 1-10).

Sony. (2021). *RX0-II Camera Specifications.* Retrieved from sony.com: https://store.sony.cl/dsc-rx0m2/p

Stevens, J. R., Goechner-Wald, N., Keskitalo, R., McCallum, N., Ali, A., Borril, J., . . . al., e. (2018). Designs for Next Generation CMB Survey Strategies from Chile. *Millimeter, Submillimeter, and Far-Infrared Detectors and Instrumentations for Astronomy IX, SPIE Astronomical Telescopes + Instrumentation, Proceedings Volume 10708.* California.

Swetz, D. S., Ade, P. A., Amiri, M., Appel, J. W., Battistelli, E. S., Burger, B., . . . Zhao, Y. (2011). Overview of the Atacama Cosmology Telescope: Receiver, Instrumentation, and Telescope Systems. *The Astrophysical Journal Supplement Series, 194:41*, 17.

Togawa, H., Hatakeyama, K., & Yamauchi, K. (2005). Reflectivity measurements in anechoic chambers in the microwave to millimeter range. *IEEE Transactions on Electromagnetic Compatibility, vol. 47, no. 2*, pp. 312-319.

Virginia Diodes. (2021). *Vector Network Analyzer Extenders.* Retrieved from https://www.vadiodes.com/: https://www.vadiodes.com/en/spectrum-analyzer-extension-modules-sax

Virginia Diodes Inc. (2021). *Integrated AMC - VDI Model: WR6.5AMC-I/WR6.5AMC-I-M6.* Retrieved from Vadiodes.com: https://www.vadiodes.com/images/Products/Int-AMC_MixAMC/VDI-740_AMC-I_Product_Manual.pdf

Wijinhols, S. J., Pupillo, G., Bolli, P., & Virone, G. (2016). UAV-aided calibration for commissioning of phased array radio telescopes. *2016 URSI Asia-Pacific Radio Science Conference (URSI AP-RASC).* Seoul.
Wilson, T., Rohlfs, T., & Huettemeister, S. (2012). *Tools of Radio Astronomy (5th ed.).* Springer.

Xu, Z., Brewer, M. K., Fluxá, P. R., Li, Y., Osumi, K., Pradenas, B., . . . Wollack, E. J. (2020). Two-year Cosmology Large Angular Scale Surveyor (CLASS) Observations: 40 GHz Telescope Pointing, Beam Profile, Window Function and Polarization Performance. *The Astrophysical Journal, 891:134*, 25pp.

Zemcov, M., Ade, P., Bock, J., Bowden, M., Brown, M. L., Cahill, G., . . . Wu, E. Y. (2009). Characterization of the Millimeter-Wave Polarization of Centaurus A with QUaD. *The Astrophysical Journal 710*, 1541-1550.

Zhang, J.-C., Jiao, K., & Zhang, T.-J. (2019). Model-independent measurement of the Hubble Constant and the absolute magnitude of Type Ia Supernovae. *Journal of Cosmology and Astroparticle Physics, Volume 2019*.